

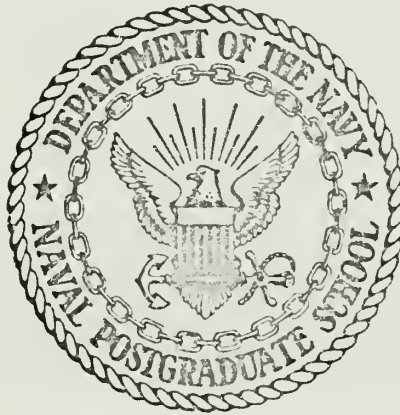
AN INVESTIGATION OF SECONDARY-FLOW  
PHENOMENA AND ASSOCIATED LOSSES  
IN A HIGH-DEFLECTION TURBINE CASCADE

James Raney Woods



# NAVAL POSTGRADUATE SCHOOL

## Monterey, California



# THESIS

AN INVESTIGATION OF SECONDARY-FLOW  
PHENOMENA AND ASSOCIATED LOSSES  
IN A HIGH-DEFLECTION TURBINE CASCADE

by

James Raney Woods, Jr.

Thesis Advisor:

M. H. Vavra

September 1972

T148508

*Approved for public release; distribution unlimited.*



An Investigation of Secondary-Flow Phenomena  
and Associated Losses  
in a High-Deflection Turbine Cascade

by

James Raney Woods, Jr.  
Lieutenant Commander, United States Navy  
B.S., United States Naval Academy, 1962

Submitted in partial fulfillment of the  
requirements for the degree of

DOCTOR OF PHILOSOPHY

from the  
NAVAL POSTGRADUATE SCHOOL  
September 1972



## ABSTRACT

In this study precise quantitative data were established for the overall flow losses in a high-deflection turbine rotor cascade for a range of aspect ratios  $h/c$  from 1.480 to 0.592. The magnitude of the losses due to secondary-flow effects was also determined. From these measurements it was possible to obtain an improved physical description of the complex secondary-flow phenomena.





## TABLE OF CONTENTS

I.	INTRODUCTION -----	9
II.	NATURE OF THE PROBLEM -----	11
	A. DEFINITION OF SECONDARY FLOW -----	11
	B. DESCRIPTION OF SECONDARY FLOW -----	11
	1. Cascade Secondary Flow -----	13
	2. Corner Vortices -----	16
	3. Trailing Vortices -----	16
	4. Tip-Clearance Flow -----	17
	5. Scraping Effect -----	17
	6. Radial Flow -----	18
	C. THREE-DIMENSIONAL FLOW IN CASCADES -----	18
III.	EXPERIMENTAL APPARATUS AND PROCEDURES -----	29
	A. RECTILINEAR CASCADE TEST FACILITY -----	29
	B. CHANNEL-FLOW MODEL -----	47
IV.	RESULTS AND DISCUSSION -----	52
	A. CASCADE TESTS -----	52
	B. CHANNEL-FLOW-MODEL TESTS -----	80
	C. CORRELATIONS FOR PREDICTION OF SECONDARY LOSSES -----	83
V.	CONCLUSIONS -----	88
	A. SECONDARY-FLOW LOSSES -----	88
	B. SECONDARY-FLOW DESCRIPTION -----	89
	C. GENERAL -----	91
	APPENDIX A: REDUCTION OF CASCADE TEST DATA -----	93
	APPENDIX B: REDUCTION OF CHANNEL-FLOW-MODEL TEST DATA -----	103



APPENDIX C: MEASUREMENT OF OUTLET THROUGH-FLOW ANGLE -----	107
COMPUTER PROGRAM CASCADE II -----	110
BIBLIOGRAPHY -----	117
INITIAL DISTRIBUTION LIST -----	121
FORM DD 1473 -----	122



## LIST OF FIGURES

### Figure

1.	Secondary Flows and Vortices in an Axial-Flow Compressor Rotor (adapted from Ref. 1) -----	12
2.	Secondary Flow in a Bend Showing the Cascade Secondary Vortices (adapted from Ref. 12) -----	14
3.	Secondary Flow in a Cascade Showing the Corner Vortices (adapted from Ref. 11) -----	14
4.	Profile Geometry of the High-Deflection, Impulse-Type Turbine Rotor Blade -----	30
5.	Cascade Installation -----	32
6.	Exit Probe Carriage and Adjustable Support -----	32
7.	Spanwise Distributions of Loss Coefficients $Y_2$ and $\zeta_2$ for $h = 10.0$ inches ( $h/c = 1.480$ ) ----	34
8.	Flow Probes for Cascade Tests (Top, Two-Dimensional - Bottom, Three-Dimensional) -----	39
9.	Calibration Curves for Two-Dimensional Probe ----	40
10.	Calibration Curves for Three-Dimensional Probe --	40
11.	Installation for End-Wall Boundary-Layer Surveys -----	46
12.	Tubing for Surface Static-Pressure Measurements -----	46
13.	Channel-Flow-Model Installation for 90-Degree Curved Section -----	51
14.	Spanwise Distributions of Loss Coefficients $Y_2$ and $\zeta_2$ for $h = 7.0$ inches ( $h/c = 1.036$ ) ----	53
15.	Spanwise Distributions of Loss Coefficients $Y_2$ and $\zeta_2$ for $h = 6.0$ inches ( $h/c = 0.888$ ) ----	54
16.	Spanwise Distributions of Loss Coefficients $Y_2$ and $\zeta_2$ for $h = 5.0$ inches ( $h/c = 0.740$ ) ----	55
17.	Spanwise Distributions of Loss Coefficients $Y_2$ and $\zeta_2$ for $h = 4.0$ inches ( $h/c = 0.592$ ) ----	56



18.	Mid-Span Total-Pressure Loss Coefficient -----	60
19.	Variation of Secondary Loss in Total Pressure with Blade Height -----	60
20.	Separation of Overall Loss into Two- Dimensional Loss and Secondary Loss for Each Blade Height -----	61
21.	Contours of Constant Relative Total Pressure at Cascade Exit for $h = 7.0$ inches ( $h/c = 1.036$ ) -----	63
22.	Contours of Constant Relative Total Pressure at Cascade Exit for $h = 6.0$ inches ( $h/c = 0.888$ ) -----	64
23.	Contours of Constant Relative Total Pressure at Cascade Exit for $h = 5.0$ inches ( $h/c = 0.740$ ) -----	65
24.	Contours of Constant Relative Total Pressure at Cascade Exit for $h = 4.0$ inches ( $h/c = 0.592$ ) -----	66
25.	Boundary-Layer Flow Pattern on End Wall -----	68
26.	Boundary-Layer Flow Pattern on Pressure Surface --	68
27.	Boundary-Layer Flow Pattern on Suction Surface in Leading-Edge Region -----	70
28.	Boundary-Layer Flow Pattern on Suction Surface in Mid-Chord Region -----	71
29.	Boundary-Layer Flow Pattern on Suction Surface in Trailing-Edge Region -----	72
30.	Percent-Surface Coordinates for Cascade Blade ---	73
31.	Static-Pressure Distributions on Blade Surface for $h = 7.0$ inches ( $h/c = 1.036$ ) -----	75
32.	Static-Pressure Distributions on Blade Surface for $h = 6.0$ inches ( $h/c = 0.888$ ) -----	76
33.	Static-Pressure Distributions on Blade Surface for $h = 5.0$ inches ( $h/c = 0.740$ ) -----	77
34.	Static-Pressure Distributions on Blade Surface for $h = 4.0$ inches ( $h/c = 0.592$ ) -----	78
35.	Tufts Attached to Blade Suction Surface -----	79





36.	Kinetic-Energy Loss Coefficient $\bar{\zeta}$ of Channel- Flow Model for Various Deflection Angles -----	82
37.	Comparison of Griepentrog's Secondary-Loss Correlation with Cascade Test Results -----	86
A1.	Entropy Diagram of Accelerated Flow through Cascade -----	95
A2.	Nomenclature for Cascade Flow -----	95
B1.	Schematic Side View of Channel-Flow Model -----	103
C1.	Error in Measurement of Outlet Through-Flow Angle in Blade Wake Region -----	108



## ACKNOWLEDGEMENT

The author gratefully acknowledges the guidance and advice given by Professor M. H. Vavra of the Department of Aeronautics and the willing cooperation and competent assistance provided by Mr. J. E. Hammer and Mr. R. W. Savage of the Turbo-Propulsion Laboratory.



## I. INTRODUCTION

Advanced, small gas-turbine power plants are being developed for many present and future applications. Low specific fuel consumptions are obtained if compressors and turbines can be built that have good efficiencies at high pressure ratios. However, economical reasons and practical design considerations require turbomachines that can handle the high pressure ratios with a minimum number of stages. Axial turbines, in particular, must therefore operate with transonic or supersonic nozzle velocities, and the rotor bladings must have large flow deflections to produce the necessary high specific work output. Three-dimensional or secondary flow effects are responsible for a major portion of the flow losses that occur in cascades of rotor bladings with large deflections and small ratios of blade height to rotor diameter.

Although a considerable amount of research work has been carried out in the past to obtain a better understanding of the physical nature of the secondary-flow phenomena, only limited data are presently available for the prediction of the losses associated with secondary flows in bladings with high turning angles and small blade heights. The objectives of the present study were to establish precise quantitative data for the overall flow losses in a high-deflection rotor cascade, varying blade height, and to determine the magnitude



of the losses due to secondary-flow effects. From these measurements it was also possible to obtain an improved physical description of the complex secondary-flow phenomena, which are not well understood at present.

Due to the difficulties associated with measuring fluid properties in the rotating bladings of small turbines, the investigation was carried out in the Rectilinear Cascade Test Rig. This facility is an open-cycle wind tunnel specifically designed for flow-testing cascades of axial compressor or turbine blades. In this test rig, model blades of large size that have the same profiles along the span are arranged along a straight axis, and the flow through these blades is investigated by means of traversing probes that measure the fluid properties ahead of and after the cascade. The subsonic Cascade Test Facility of the Turbo-Propulsion Laboratory is well-suited for this type of investigation since its large size minimizes the disturbing effects of introducing probes into the flow. Moreover, because of its peculiar design, the Cascade Test Rig can be operated without having to remove the boundary layers on the channel side walls that guide the flow to the test cascade, since these side walls are of equal length [Ref. 27].





## II. NATURE OF THE PROBLEM

### A. DEFINITION OF SECONDARY FLOW

Secondary flow in an axial-flow turbomachine is defined as the difference between the actual three-dimensional flow and the flow which occurs on assumed axisymmetric stream surfaces, and it is principally caused by the interaction of the hub and casing boundary layers with the primary through-flow. Similarly, secondary flow in a rectilinear cascade is considered to be the difference between the real flow in a finite-span cascade and the two-dimensional flow in a cascade with infinite blade height, and it is due to the interaction of the end-wall boundary layers with the main through-flow. In practice two-dimensional flow in a cascade is frequently achieved by removing the wall boundary layers.

### B. DESCRIPTION OF SECONDARY FLOW

As shown in Fig. 1, a reasonably clear physical description of the nature of secondary flows in turbomachines has resulted from extensive qualitative investigations using various flow-visualization techniques, namely injecting smoke into the flow or obtaining boundary-layer traces from a nondrying substance applied to the flow boundaries [Refs. 2-11]. The secondary flows and vortices in Fig. 1 are closely interrelated and are part of the total flow field; but in order to successfully treat their effects



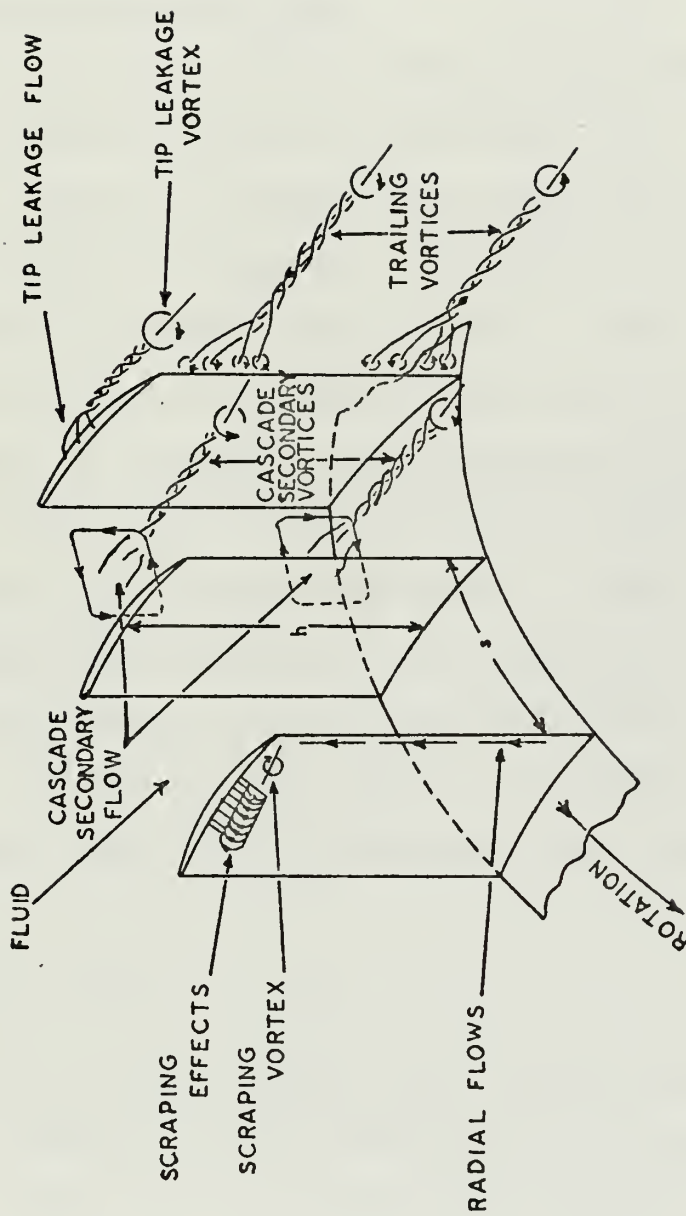


Figure 1. Secondary Flows and Vortices in an Axial-Flow Compressor Rotor (adapted from Ref. 1).



both experimentally and theoretically, they are separated for convenience into the following: cascade secondary flow, corner vortices (not shown in Fig. 1), trailing vortices, tip-clearance flow, scraping effect, and radial flow.

### 1. Cascade Secondary Flow

The explanation of the origin of the cascade secondary flow is based on that of Vavra [Ref. 12]. In Fig. 2 the passage between two neighboring blades of a cascade without diffusion or expansion is represented by a rectangular bend with a constant cross section. A flow with uniform static pressure enters the channel from the left as indicated in the figure. A nonuniform total-pressure distribution results from the boundary layers that are formed on the upper and lower walls ahead of the bend. Hence, the inlet velocity profile has a uniform part, where  $V_1 = V_{1m}$  is constant, and reduces to zero at both end walls.

The flow through the channel is assumed to be steady, incompressible, and inviscid; therefore, the equation of motion is

$$\nabla(P_t/\rho) = \vec{V} \times (\nabla \times \vec{V}) \quad (1)$$

where  $P_t$  is the total pressure,  $\rho$  is the density, and  $\vec{V}$  is the velocity vector. Since inviscid flow is assumed,  $V_1 = V_{1m}$  is taken as constant along the entire mean flow path (Fig. 11 (29b) of Ref. 12). With the cylindrical coordinate system of Fig. 2,  $\vec{V} = \hat{i}_1 V_{1m}$  and  $V_2 = V_3 = 0$ ; thus, neglecting changes in the  $z$ -direction and the gravitational forces, Eq. 1 becomes



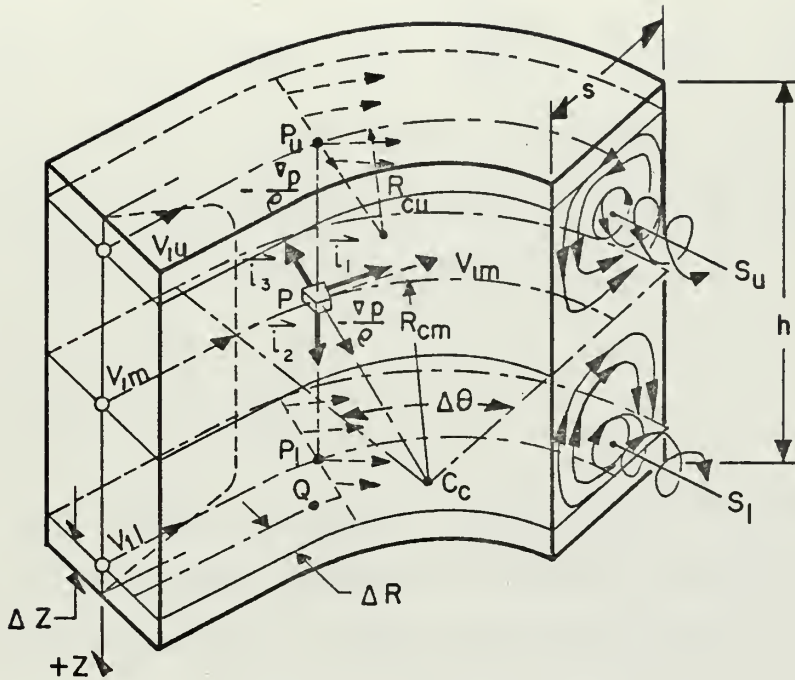


Figure 2. Secondary Flow in a Bend Showing the Cascade Secondary Vortices (adapted from Ref. 12).

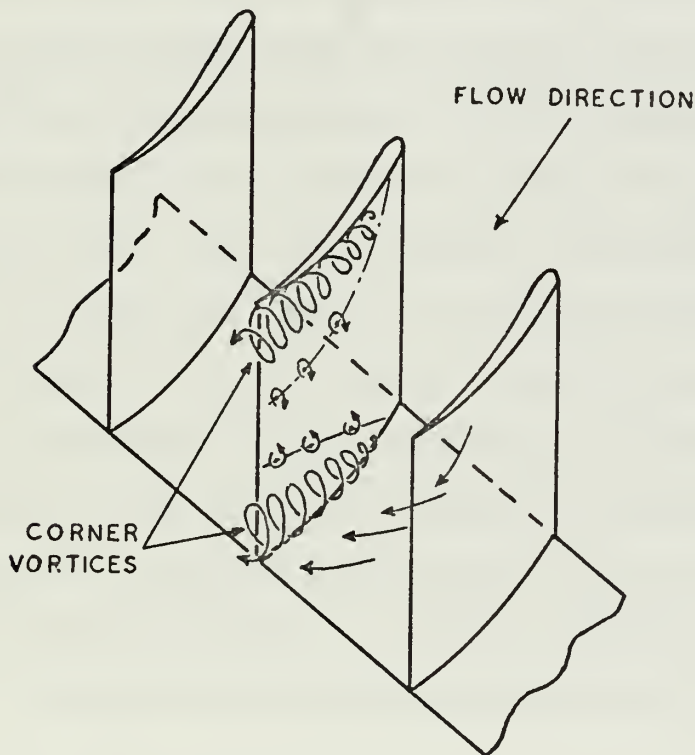


Figure 3. Secondary Flow in a Cascade Showing the Corner Vortices (adapted from Ref. 11).





$$\nabla \left( \frac{p}{\rho} + \frac{V_{1m}^2}{2} \right) = \vec{i}_1 V_{1m} \times \frac{\vec{i}_2}{R} \frac{\partial (RV_{1m})}{\partial R} = \vec{i}_3 \frac{V_{1m}}{R} \frac{\partial (RV_{1m})}{\partial R}$$

for the flow outside of the end-wall boundary layers. In this region the velocity  $V_{1m}$  is also constant in the radial direction. Thus, at point P where  $R = R_{cm}$ ,

$$-\nabla(p/\rho) = -\vec{i}_3 \frac{V_{1m}^2}{R_{cm}} \quad (2)$$

where  $p$  is the static pressure. The quantity  $-\nabla(p/\rho)$  is the force per unit mass exerted on a fluid particle.

According to Eq. 2, the fluid particles are in equilibrium between the centrifugal force and the static pressure gradient along a radius between the curved channel walls, where the convex wall and the concave wall are analogous to the cascade-blade suction side and pressure side, respectively. Since the static pressure inside a boundary layer equals that outside of it, the same gradient  $\nabla(p/\rho)$  is assumed to exist all along the vertical line through P, in direction of  $\vec{i}_2$ , from the upper to the lower wall. At the point  $P_u$  the velocity  $V_{1u}$  is smaller than  $V_{1m}$ ; and since the force per unit mass  $-\nabla(p/\rho)$  exerted on a fluid particle at  $P_u$  is equal to that at P, the radius of curvature  $R_{cu}$  of the flow path at  $P_u$  must be smaller than  $R_{cm}$  to satisfy the equilibrium condition of Eq. 2. Similar conditions exist at the point  $P_l$ . Therefore, the fluid particles at the two end walls have the tendency to flow from the pressure side of the channel to the suction side, and the movement continues on the suction side towards mid-channel. Since the flow



directions are opposite at the upper and lower walls, two cascade secondary vortices  $S_u$  and  $S_l$ , which have opposing rotations, are formed, as shown in Fig. 2.

## 2. Corner Vortices

If viscous effects are considered in the flow of Fig. 2, corner vortices will be formed at the intersections of the end walls and the suction surface of the cascade blading, due to the interaction of the accumulation of low-energy boundary-layer material flowing into this corner with the blade suction-side boundary layer. The corner vortices are shown schematically in Fig. 3, where the cascade secondary vortices are omitted for clarity.

Senoo [Ref. 13] proposed a theoretical model for the formation of the corner vortices. The end-wall boundary layer was represented by a series of parallel vortex sheets. The deflection of a vortex sheet in the corner formed by the end wall and the blade suction side causes a self-induced rolling-up motion, similar to that of the trailing vortex of a finite wing; and the secondary flow in the corner is not a single vortex but a rolled-up vortex sheet. Senoo obtained good qualitative agreement between this hypothesis and measurements of the boundary layer on an end wall of a turbine stator cascade.

## 3. Trailing Vortices

The vortices that exist at the exit of a cascade as trailing vortices are due to the vortex sheet that is induced by a variable circulation over the blade height or by the



decrease in circulation caused by a tip clearance at the hub or casing. The trailing vortex sheet does not persist in an actual flow; it splits up into single vortices, which are unstable and tend to combine in larger single vortices [Ref. 9]. In the case presented in Fig. 1, single trailing vortices are formed in the two halves of the blade passage with rotation opposite to the cascade secondary vortices.

#### 4. Tip-Clearance Flow

Tip-clearance flow in unshrouded blading has two sources. The clearance space between the blade tip and the hub or casing allows a portion of the through-flow to pass, which is undeflected and therefore does not participate in the energy exchange. Also, a tip vortex is formed because of the flow over the tip due to the static pressure difference on the pressure and suction surfaces of the blades.

#### 5. Scraping Effect

Flow-visualization studies by NACA [Refs. 2, 5, and 6] demonstrated that if relative motion exists between the blades and the casing, the leading surfaces of the blades scrape up entrained fluid near the wall and impart a vortex motion to the fluid in this region. However, Dean [Ref. 14] suggested that it is the fluid moving with the rotor, not the blade itself, which scrapes up the casing boundary layer. In either case it is the motion of the rotor blade relative to the casing boundary layer, rather than the pressure difference across the tip, that is responsible for the scraping vortex depicted in Fig. 1.



In a compressor where the pressure surface of the rotor blade leads, the scraping effect improves flow conditions in the tip region by preventing flow on the pressure side from deflecting over the tip, and reduces the tendency of flow separations in the trailing-edge region of the blade suction surface by aspirating low-energy fluid off the suction side [Refs. 2 and 5]. In a turbine, however, where the rotor-blade suction surface leads, the scraping effect aggravates tip-clearance effects by decreasing the static pressure in the pressure-side tip region and by piling up fluid on and near the suction side, thereby increasing the tendency for the flow to separate [Refs. 2 and 5].

#### 6. Radial Flow

Due to radial pressure gradients in annular cascades, boundary-layer material is transported along the blade span, mainly over the suction surface in the rear part of the blade. In the stator the low-energy fluid is transported to the hub and produces larger flow losses in this region [Refs. 2 and 5]. In the case of the rotor, the centrifugal force and Coriolis acceleration can cause a radial flow from the hub to the tip of the blade [Ref. 1].

### C. THREE-DIMENSIONAL FLOW IN CASCADES

The present investigation is concerned with the secondary flow in a stationary, linear turbine cascade with zero clearance at the blade ends; thus, it does not include the phenomena associated with tip-clearance flow, scraping effect, and radial flow. The principal characteristic of





the secondary-flow process in turbomachines or cascades is a redistribution and collection of the low-momentum fluid in the blade passages, mainly from the end-wall boundary layers to the main body of the flow. These flow phenomena are three-dimensional in nature, since significant cross-flows are involved in the redistribution. The displacement of the low-energy fluid occurs in a vortex-like manner, and this fluid tends to collect near the corners formed by the blade suction surface and the end walls. Hence, these accumulations of fluid influence the mainstream flow as well as the flow in the suction-side boundary layer.

If the flow through a cascade is assumed to be incompressible with constant viscosity and negligible gravitational forces, the governing equations are the equation of continuity,

$$\nabla \cdot \vec{U} = 0 \quad (3)$$

and the equation of motion,

$$\frac{\partial \vec{U}}{\partial t} + (\vec{U} \cdot \nabla) \vec{U} = - \frac{\nabla p}{\rho} + \frac{\mu}{\rho} \nabla^2 \vec{U} \quad (4)$$

where  $\vec{U}$  is the velocity vector,  $p$  and  $\rho$  are the static pressure and density respectively, and  $\mu$  is the dynamic viscosity of the fluid. Equations 3 and 4 account for the detailed fluctuating motion of the turbulent flow in cascades. However, the analysis of these unsteady equations is at present limited to two-dimensional flows, and it has become customary to use an averaged set of equations for three-dimensional flows [Ref. 15].



Since the turbulence flow field in cascades can be considered as quasi-steady, Eqs. 3 and 4 are averaged with respect to time [Ref. 16]. The velocity vector and static pressure are given by

$$\vec{U} = \vec{V} + \vec{u}$$

and

$$p = \bar{p} + p'$$

respectively, where  $\vec{V}$  and  $\bar{p}$  are time-averaged quantities and  $\vec{u}$  and  $p'$  are fluctuation terms. By definition, time averages of the fluctuation quantities are equal to zero. The additional assumption of steady mean flow is made. The above values are substituted into Eqs. 3 and 4, and the resulting equations are time-averaged to obtain:

$$\nabla \cdot \vec{V} = 0 \quad (5)$$

$$(\vec{V} \cdot \nabla) \vec{V} + \overline{(\vec{u} \cdot \nabla) \vec{u}} = - \frac{\nabla p}{\rho} + \frac{\mu}{\rho} \nabla^2 \vec{V} \quad (6)$$

In the averaging process only the terms that are quadratic in the fluctuating velocity components remain, and their time averages are denoted by overscores in the equations. From Eqs. 3 and 5, there is also

$$\nabla \cdot \vec{u} = 0$$

Thus, the time-averaged and fluctuation velocity vectors each satisfy the incompressible continuity equation.

The vector relations

$$(\vec{V} \cdot \nabla) \vec{V} = \nabla \left( \frac{V^2}{2} \right) - \vec{V} \times (\nabla \times \vec{V})$$



and

$$\nabla \cdot \overline{(\vec{u}\vec{u})} = \overline{(\nabla \cdot \vec{u})\vec{u}} + \overline{(\vec{u} \cdot \nabla)\vec{u}}$$

introduced in Eq. 6 give

$$\nabla \left( \frac{\bar{P}_t}{\rho} \right) = \vec{V} \times (\nabla \times \vec{V}) + \frac{\mu}{\rho} \nabla^2 \vec{V} - \nabla \cdot \overline{(\vec{u}\vec{u})} \quad (7)$$

where  $\bar{P}_t = \bar{p} + \frac{\rho}{2} V^2$ .

Equations 5 and 7 are the time-mean equation of continuity and equation of motion respectively. In Eq. 7 the term  $-\overline{(\vec{u}\vec{u})}$  is the kinematic form of the so-called Reynolds stresses, which are additional fluid stresses caused by turbulent fluctuation. The time-averaged and fluctuation velocity vectors  $\vec{V}$  and  $\vec{u}$  in Eqs. 5 and 7 must satisfy the boundary conditions that their components vanish at solid walls.

Equations 5 and 7 and the boundary conditions do not constitute a closed set of equations for the evaluation of the three-dimensional mean flow in cascades, unless a relation between the averaged and turbulent velocity components is known. Such a relation can only be obtained empirically [Ref. 17]. For example, Gawain and Pritchett [Ref. 15] have developed a unified heuristic model of fluid turbulence, which has been successfully applied to flows in a two-dimensional uniform channel and in an axisymmetric free turbulent jet. However, solutions of Eqs. 5 and 7 for three-dimensional turbulent flows in cascades have not yet been obtained.



If the flow is assumed to be nonturbulent, Eq. 7 reduces to the steady Navier-Stokes equation. Although this assumption produces a major simplification in terms of the nature of the flow, exact solutions of the Navier-Stokes equation are only available for comparatively simple cases; for example, parallel flow, Couette flow, and Hagen-Poiseuille flow. Even with modern high-speed digital computers, the solutions of the nonlinear turbulent or nonturbulent flow equations are associated with major mathematical difficulties.

The steady, incompressible flow through a circular turbine cascade may be represented by the channel flow in Fig. 2, with the inlet conditions as described in Section II.B.1. The continuity equation is given by Eq. 5, and the equation of motion is

$$\nabla \left( \frac{P}{\rho} \right) = \vec{V} \times (\nabla \times \vec{V}) + \frac{\mu}{\rho} \nabla^2 \vec{V} \quad (8)$$

In general the velocity vector  $\vec{V}$  can be expressed by the components  $V_1$ ,  $V_2$ , and  $V_3$  in the directions of the unit vectors in Fig. 2,  $\vec{i}_1$ ,  $\vec{i}_2$ , and  $\vec{i}_3$ , respectively; and it must satisfy the no-slip condition at the channel walls.

Without loss of generality, the streamline through a particular point Q (Fig. 2) is assumed to be the intersection of a surface of constant  $z$  and of constant  $R$ ; so that at this point  $\vec{V} = \vec{i}_1 V_1$  and  $V_2 = V_3 = 0$ . Generally this is not possible at other stations in the flow field. Hence, the derivatives of  $V_2$  and  $V_3$  in the different directions do not vanish even if these components are zero at the particular station Q.





In the cylindrical coordinate system of Fig. 2, there is

$$\nabla = \frac{\vec{i}_1}{R} \frac{\partial}{\partial \theta} + \vec{i}_2 \frac{\partial}{\partial z} + \vec{i}_3 \frac{\partial}{\partial R} \quad (9)$$

Equations 5 and 8 are now expressed for the flow at the point Q. With Eq. 9 the continuity equation becomes

$$\frac{1}{R} \frac{\partial V_1}{\partial \theta} + \frac{\partial V_2}{\partial z} + \frac{\partial V_3}{\partial R} = 0 \quad (10)$$

The equation of motion yields the following three partial differential equations from its components in the directions of the unit vectors  $\vec{i}_1$ ,  $\vec{i}_2$ , and  $\vec{i}_3$  respectively:

$$\frac{1}{R} \frac{\partial}{\partial \theta} \left( \frac{P_t}{\rho} \right) = \frac{\mu}{\rho} \left( \frac{1}{R^2} \frac{\partial^2 V_1}{\partial \theta^2} + \frac{\partial^2 V_1}{\partial z^2} + \frac{\partial^2 V_1}{\partial R^2} + \frac{1}{R} \frac{\partial V_1}{\partial R} - \frac{V_1}{R^2} + \frac{2}{R^2} \frac{\partial V_3}{\partial \theta} \right) \quad (11)$$

$$\begin{aligned} \frac{\partial}{\partial z} \left( \frac{P_t}{\rho} \right) &= \frac{V_1}{R} \left( \frac{\partial (RV_1)}{\partial z} - \frac{\partial V_2}{\partial \theta} \right) \\ &+ \frac{\mu}{\rho} \left( \frac{1}{R^2} \frac{\partial^2 V_2}{\partial \theta^2} + \frac{\partial^2 V_2}{\partial z^2} + \frac{\partial^2 V_2}{\partial R^2} + \frac{1}{R} \frac{\partial V_2}{\partial R} \right) \end{aligned} \quad (12)$$

$$\begin{aligned} \frac{\partial}{\partial R} \left( \frac{P_t}{\rho} \right) &= \frac{V_1}{R} \left( \frac{\partial (RV_1)}{\partial R} - \frac{\partial V_3}{\partial \theta} \right) \\ &+ \frac{\mu}{\rho} \left( \frac{1}{R^2} \frac{\partial^2 V_3}{\partial \theta^2} + \frac{\partial^2 V_3}{\partial z^2} + \frac{\partial^2 V_3}{\partial R^2} + \frac{1}{R} \frac{\partial V_3}{\partial R} - \frac{2}{R^2} \frac{\partial V_1}{\partial \theta} \right) \end{aligned} \quad (13)$$

Equations 10 through 13 serve to point out the complexities involved in the analytical treatment of the secondary-flow problem in turbine cascades. Even for the unique conditions that exist at the point Q, Eqs. 12 and 13 retain their nonlinear terms. Surfaces of constant total pressure, which were originally planes of constant  $z$ , do not remain



plane; they tend to bend and rotate on passing through the channel. Furthermore, no a priori assumptions can be made about stream surfaces that describe the three-dimensional, viscous nature of the flow, since streamlines as the one at station Q are not representative of the entire flow field.

At present, fully three-dimensional flow calculations in turbomachines are restricted to the inviscid case; that is, for  $\mu = 0$  in Eq. 8. In Ref. 18 progress on a current research effort is reported in which a computer program has been developed for the analysis of three-dimensional, inviscid, subsonic flows in ducts. The computational method, based on the theory of Wu [Ref. 19], involves the solution of the governing equations on arbitrary but predetermined stream surfaces. Improved estimates of the stream-surface geometries are systematically generated by iteration until a specified convergence criterion is met.

This computer program has been successfully applied to three-dimensional, irrotational flows. However, major computational difficulties were encountered in trying to generalize the calculating procedure to allow for rotational flow at the inlet. As described in Section II.B.1, it is the rotational inlet flow which causes the cascade secondary flow. The elliptical nature of the subsonic flow equations requires that boundary conditions be applied on all fluid boundaries. Since the three-dimensional exit flow conditions are unknown, initial outlet boundary conditions must be assumed and then modified until a satisfactory approximation of the inlet flow is obtained. In addition, the program



required modification to handle the large stream-surface rotations that occur if the flow is deflected through a channel, and it was necessary to introduce a coordinate system that warps at a constant angular rate as it passes through the duct.

Although the investigation is still incomplete, some comparisons between calculated results and available experimental data are contained in Ref. 18. Satisfactory agreement was obtained for a square duct with 30 degrees of turning, but the agreement was unsatisfactory for a higher deflection of 60 degrees. It should be pointed out that the classical inviscid analyses of the secondary-flow problem [Refs. 20 and 21], in which the actual three-dimensional flow was treated as a perturbation on a two-dimensional flow, are also applicable for turning angles up to about 30 degrees.

For assumed inviscid flow the calculated streamwise or secondary vorticity is distributed uniformly across the flow passage. Whereas, experience has shown that the secondary-flow effects are concentrated near the suction-surface and end-wall corner region. Furthermore, if the inlet flow is uniform, an inviscid calculation cannot account for nor explain the generating of secondary flows. However, Louis [Ref. 10] showed that high secondary losses occurred in the corner region of a compressor cascade with uniform inlet flow conditions. In these experiments a wall was arranged at the mid-span of the cascade. This wall extended from a line through the leading edges of the blades



to a station downstream of the cascade; therefore, no boundary layer could develop ahead of the blading. The interaction of the flow over the suction side of the blade with that along the wall produced considerable secondary-flow losses. Thus, even three-dimensional, inviscid flow calculations give only qualitative information about the secondary-flow losses; and the applicability of this approach to high-deflection turbine cascades is highly questionable.

Boundary-layer theory has also been applied to the secondary-flow problem in turbomachines. The flow field is divided into a region where viscous effects are neglected and a thin boundary region adjacent to solid walls where such effects are considered. In the boundary layer the viscous equations of motion can be simplified to obtain the so-called boundary-layer equations. The three-dimensional boundary-layer flow in the suction-surface and end-wall corner region is of particular interest for the secondary-flow analysis in cascades. Reference 22, which is a comprehensive survey of the present state of the art of boundary-layer calculations, points out that three-dimensional boundary layers in a corner cannot be solved satisfactorily. However, three-dimensional end-wall boundary layers in turbine cascades have been treated with some success by using the generalized momentum-integral equations, which are obtained by integrating the boundary-layer equations through the boundary layer [Ref. 23]. In order to solve these equations, additional empirical relations are needed to





specify the boundary-layer velocity profiles and the wall shear stress.

Senoo investigated the laminar case and obtained satisfactory agreement between his theory [Ref. 24] and observed boundary-layer behavior on an end wall of a turbine stator cascade [Ref. 13]. Dring [Ref. 25] presented an analysis of the turbulent end-wall boundary layer that is not restricted to small cross-flows. However, comparisons with secondary-flow losses measured in cascades of several geometries showed that the calculated losses and measured values differed by about 30 percent. Considering the computational efforts necessary for the solutions, this error is appreciable.

One limitation of this approach to the secondary-flow problem is the lack of experimental data for three-dimensional boundary layers that necessitates the use of a two-dimensional empirical relation for the wall shear stress. Moreover, in the analysis cross-flow effects must be limited to the end-wall boundary-layer region; whereas, experience has shown that near the blade trailing edge cross-flows continue far outside the end-wall boundary layer, and interactions with the blade suction-surface boundary layer become important. Such interactions cannot be treated with the available boundary-layer calculation methods.

Thus, the analytical treatment of the secondary flow in turbomachines is limited to qualitative physical descriptions of the complex three-dimensional flow phenomena. For this reason no theoretical method is available to accurately



predict the associated secondary losses [Ref. 26], and quantitative secondary-flow investigations for high-deflection turbine cascades must at present be experimental in nature.



### III. EXPERIMENTAL APPARATUS AND PROCEDURES

#### A. RECTILINEAR CASCADE TEST FACILITY

The Rectilinear Cascade Test Facility is an open-cycle wind tunnel that contains a large number of axial-flow turbomachine blades of identical shape, which are arranged along a straight axis with equal spacing and orientation. Cascades of this type do not actually occur in turbomachines; but if enough blades are used so that periodic exit flow conditions are established, rectilinear cascades can be utilized successfully in flow investigations as substitutes for annular rows of blades. A detailed description of the Cascade Test Rig and associated machinery was given by Rose and Guttormson [Ref. 27]. Earlier modifications were described by Bartocci [Refs. 28 and 29]. Recent additions and modifications that were required for the present investigation included a newer automatic data-acquisition system, replacement of the removable end wall with one made of one-inch Plexiglas, and relocation of the outlet measuring plane.

The profile geometry of the high-deflection, impulse-type turbine blading used in the cascade for this study is depicted in Fig. 4. The profile consists solely of straight lines and circular arcs. The leading and trailing edges are not rounded, and the design deflection angle is 132 degrees. The blade has a chord of 6.757 inches and a height



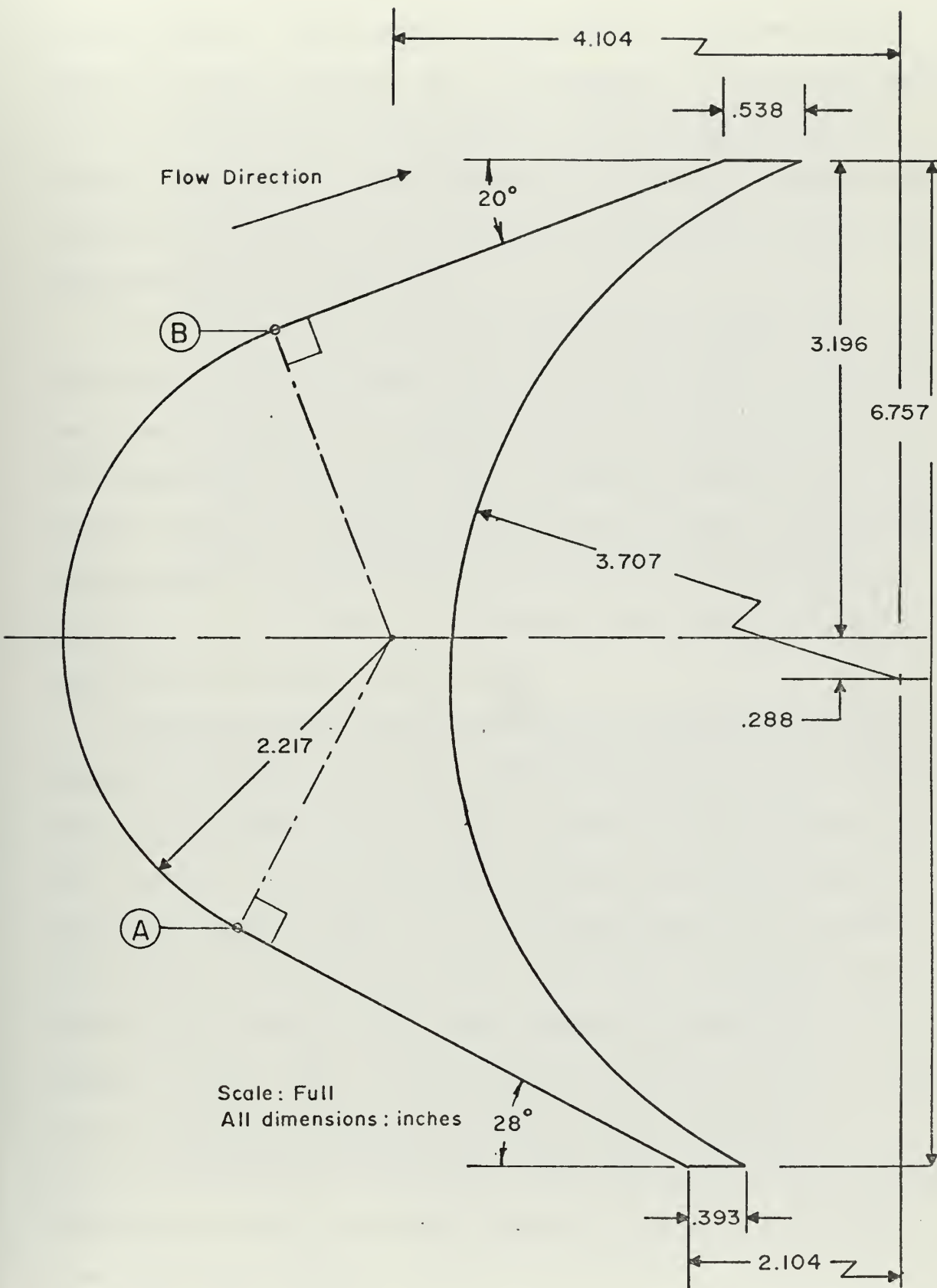


Figure 4. Profile Geometry of the High-Deflection, Impulse-Type Turbine Rotor Blade.





of ten inches. The cascade consisted of 15 blades with a spacing of four inches. The flow passage is convergent with a throat diameter of 1.18 inches. These blades are nine times scale models of the blading in an actual turbine rotor that can be tested in the Transonic Turbine Test Rig at the Turbo-Propulsion Laboratory.

The blades were installed in the cascade with zero tip clearance. The adjustable side walls upstream of the blading were set to obtain the design inlet flow angle of 62 degrees. The downstream side walls were diverged one degree from the design outlet flow angle of 70 degrees to allow for boundary-layer growth on these walls. The cascade installation is shown in Fig. 5, where the 60-degree inlet guide vanes at the plenum exit can also be seen.

Preliminary tests were initiated to verify the results obtained by Bown [Ref. 30]. Inlet and outlet flow conditions were surveyed for the two blade spacings in the center of the cascade. Total and dynamic pressure and flow angle measurements were made with two United Sensor and Control Corporation YC-120 flow probes, which are two-dimensional directional probes. The inlet measuring plane was 9.50 inches in the vertical direction from the leading-edge plane of the blading, while the outlet flow was surveyed at a vertical distance of 6.75 inches from the blade trailing edges. Surveys were made in several spanwise planes for the full ten-inch blade height.





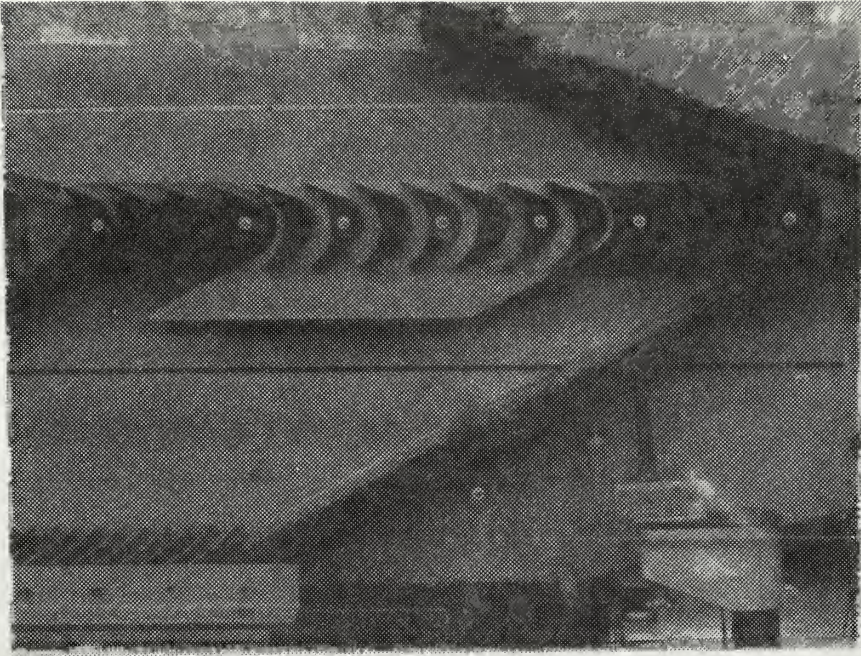


Figure 5. Cascade Installation.

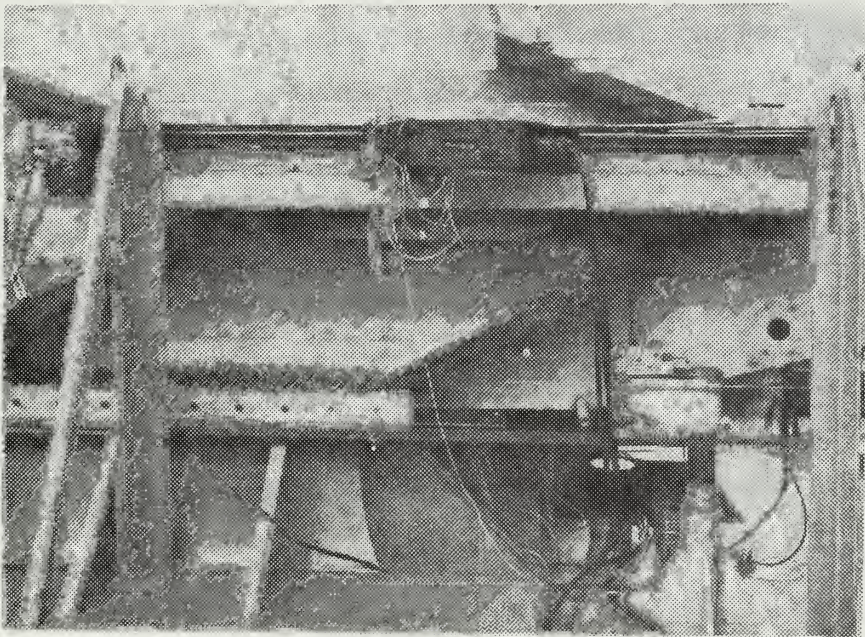


Figure 6. Exit Probe Carriage and Adjustable Support.





The resulting plots of spanwise loss distributions of Fig. 7 showed that, although there was no clearance at the blade ends, the loss was not symmetrically distributed over the blade span. Investigation showed that the seal for the lower probe slot had deteriorated, and a large leak had developed. This had the effect of removing part of the boundary-layer fluid on the end wall of the cascade where the lower peak loss coefficient had existed. The unequal end-wall boundary layers also affected the periodicity of the exit flow. The leakage was stopped with a new rubber seal, which provides a continuous seal as the probe is moved.

Subsequent surveys with a United Sensor DA-125 three-dimensional directional probe verified the existence of two-dimensional flow conditions at the entry and exit measuring planes. Although the higher losses near the end walls in Fig. 7 were produced by three-dimensional or secondary effects in the blade passages, the flow was nearly uniform and essentially two-dimensional at this downstream measuring plane, due to turbulent mixing and viscous effects. In order to obtain meaningful measurements of the three-dimensional flow, the exit measuring plane was moved to a vertical distance of  $5/16$  inch from the trailing edges. Since the existing measuring stations of the cascade are slotted in the fixed end wall, the removable end wall was replaced with a Plexiglas wall. The Plexiglas wall was slotted for the probe, and the probe carriage was mounted on an adjustable support. With this arrangement



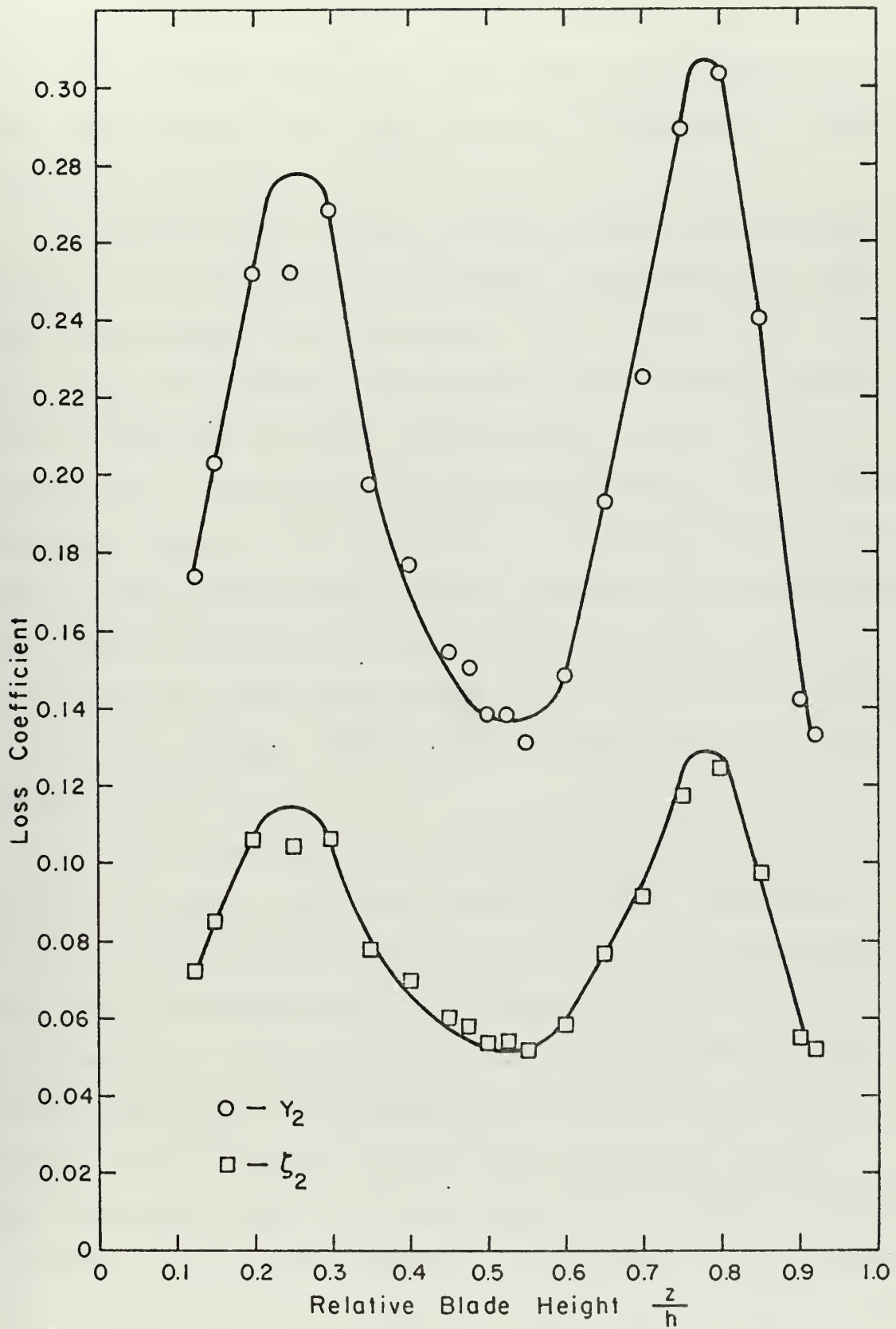


Figure 7. Spanwise Distributions of Loss Coefficients  $\gamma_2$  and  $\zeta_2$  for  $h = 10.0$  inches ( $h/c = 1.480$ ).





the outlet measuring station can be located at any desired position if appropriate slots are cut in the Plexiglas wall. The installation of the upper probe carriage and its support is shown in Fig. 6.

To ensure equal end-wall boundary layers and to provide a means for varying the blade height, adjustable end walls were manufactured from aluminum. The walls were cut to fit over the seven blades in the center of the cascade and were held in place by 1/8-inch threaded steel rods and self-locking nuts. The walls extended 4.50 inches in the vertical direction from the inlet plane of the cascade blading, and their leading edges were rounded to prevent flow separation. The gaps around the blades at the intersections with these adjustable end walls were sealed with an adhesive compound to prevent leakage. One of the adjustable end walls can be seen in Fig. 5.

For all subsequent tests the fan was run at high speed, giving an average inlet Mach number of 0.25. The periodicity of the exit flow conditions was verified by traversing three blade spacings in the center of the seven-blade test section. Static-pressure taps on the fixed end wall showed that the static-pressure distribution was uniform across the test section at the inlet measuring station. For the actual tests inlet and outlet flow conditions were surveyed for one blade spacing in the center of the cascade test section over one half of the blade span. The traverse ahead of the cascade inlet was centered at the geometric



center of the cascade, and the exit traverse was centered on the wake of the central blade in the test section.

The two-dimensional directional probe was used for the inlet surveys. This probe has three sensing holes on a prism-shaped measuring section. The probe was rotated until the two side pressures were equal. The center hole then gave the total pressure, and the through-flow angle was obtained from the probe mount. The two side pressures were connected to a choke which provided a high-resistance bleed across the differential of these two pressures and was tapped at the center to give the arithmetic mean of the two side pressures. The dynamic pressure was measured by comparing this average pressure to the total pressure obtained from the center sensing hole.

The outlet flow was surveyed with the three-dimensional directional probe which has five sensing holes on a prism-shaped measuring section. In addition to the total pressure, dynamic pressure, and through-flow angle measurements, the cross-flow angle is indicated by the differential pressure across two holes located above and below the center hole. The method that was utilized to survey the blade wake region of the outlet flow is discussed in Appendix C. Since the probe was mounted with its axis normal to the total-pressure gradient in the blade wake, errors in the indicated through-flow angle as large as ten degrees occurred in the wake region, as shown in Fig. C1. With the side sensing holes of the probe, which are



separated by a certain distance, located in regions of different total pressure, the probe rotated out of the through-flow direction in order to balance the two side pressures. This resulted in physically smaller wakes and, therefore, lower indicated loss in total pressure. By taking a constant through-flow angle through the wake region equal to that angle measured outside of the wake, which was essentially uniform, more accurate exit total pressures were obtained. In this case the two side pressures were not equal, but the choke provided a mean pressure for dynamic-pressure measurements.

The probes required calibration since the indicated average of the two side pressures does not coincide with the true static pressure. Both probes were calibrated against a Prandtl pitot-static tube in the Model-Testing Facility of the Turbo-Propulsion Laboratory. The calibration consisted of comparing the data from the survey probe to that from the Prandtl tube, both mounted in the same plane of a uniform flow in a ten-inch diameter pipe. The mounting for the survey probe allowed the probe to be pitched through different angles while maintaining the measuring section at the same position in the flow. The Mach numbers used for the probe calibrations were the same as the average inlet and outlet Mach numbers in the cascade. Calibration data were repeatable to within 0.5 percent for both survey probes.



The flow probes are shown in Fig. 8. The measuring section of both probes is located 1/4 inch from the end on 1/8-inch diameter steel tubing. The probes are reinforced with 1/4-inch diameter steel tubing. The calibration curves for the two-dimensional probe are shown in Fig. 9. Constant corrections were applied to indicated dynamic pressure for the data reduction using zero pitch angle and the average inlet Mach number. The calibration curves for the three-dimensional probe are shown in Fig. 10. Least-squares polynomial approximations to these curves were obtained for the data reduction. The pitch angle or cross-flow angle was calculated from the differential pressure,  $(p_4 - p_5)$ . Using this pitch angle the indicated dynamic pressure was corrected to the true value.

Although some accuracy was sacrificed by using these combination probes, the principal advantage was that all flow data were obtained from single probes at the inlet and outlet. The probes have a 1/8-inch sensing-head diameter, so flow passage constriction by the probe was considered negligible. Since the measuring sections of both probes are located two diameters back from the end, tip effects are minimized. The so-called immersion correction for the data was not necessary due to the configuration of the cascade, and surveys could be made to within 1/8 inch of the adjustable end walls.





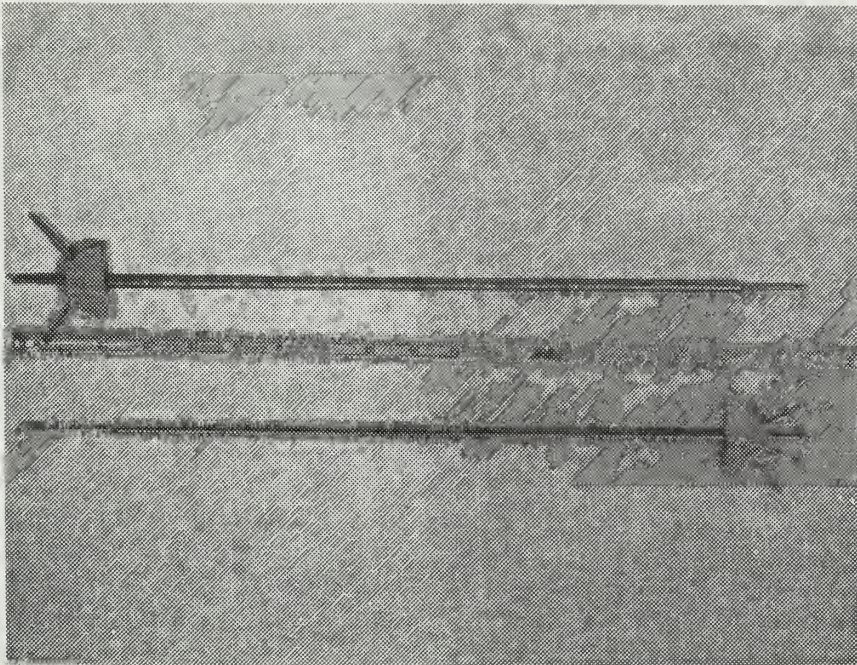


Figure 8. Flow Probes for Cascade Tests (Top, Two-Dimensional  
- Bottom, Three-Dimensional).



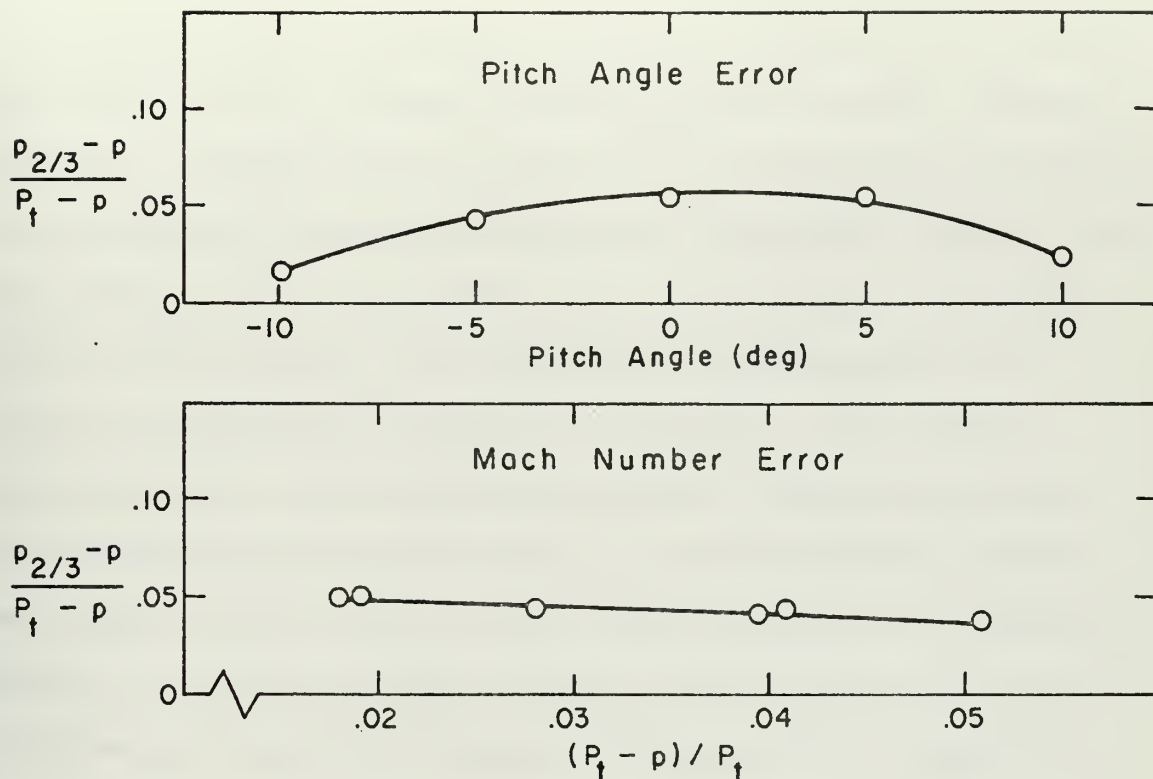


Figure 9. Calibration Curves for Two-Dimensional Probe.

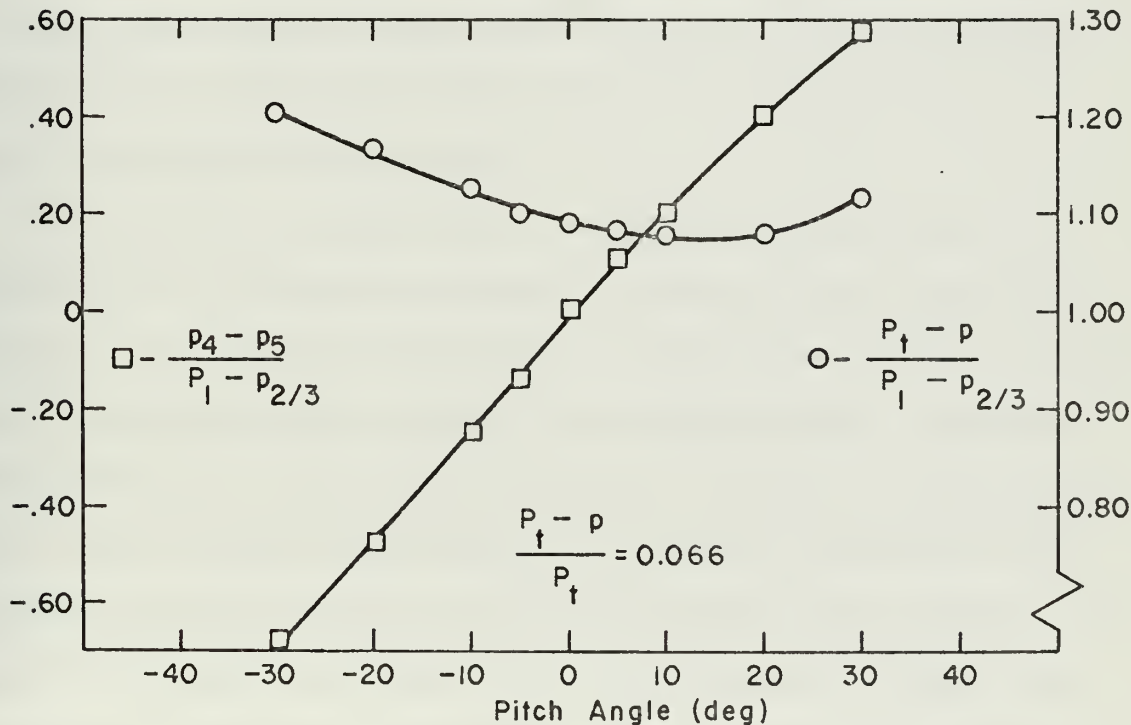


Figure 10. Calibration Curves for Three-Dimensional Probe.



The mean flow properties that were measured at the inlet and outlet of the cascade included total pressure, dynamic pressure, and through-flow angle and a differential pressure at the exit for the determination of cross-flow angle. Plenum pressure and temperature were also measured for each point in the survey. All pressures were connected to Statham differential pressure transducers. The probe pressures were also connected to water U-tube manometers for monitoring during the tests. The through-flow angles were electrically sensed using a power supply and potentiometers. A phantom ground circuit was utilized to provide a positive and negative voltage, and there was a one-to-one correspondence between the millivolt output and a positive or negative flow angle. A protractor and vernier located on the probe mounting provided a check on the flow-angle indication. The plenum temperature was measured with an iron-constantan thermocouple.

The probes, transducers, and angle potentiometers are mounted on traversing carriages, along with the electrical motors that position the probes. The probes could be rotated into the flow either manually or automatically. Automatic positioning is made possible through the use of the electrical signal from an additional differential pressure transducer connected to the two side pressures of the probe. This signal provides the drive for a servo, which rotates the probe in a direction depending on the polarity of the signal. When the pressures are balanced, no power is supplied to the





servo. Sensitivity and damping controls are provided for the servo amplifier. Electric motors are provided to move the probes into and out of the test section.

A flow survey consisted of positioning the inlet and outlet probes at corresponding positions along the blade height. The flow was traversed in the direction of the blade spacing by moving the probe carriage by hand with a crank and gearing arrangement. Because of the periodicity of the flow, it was sufficient to measure the flow conditions over one blade spacing only. The aforementioned data were taken at intervals of 0.10 inch. Such surveys were made at various spanwise locations over half the blade height.

A Systron-Donner model 160-11 automatic data-logging system was used to acquire the data from the flow surveys. The system could accept the analog signals from the plenum-temperature thermocouple, the through-flow angle potentiometers, and the bridge-type pressure transducers. The system could also accept digital data from Datex shaft-angle encoders which were mounted on the gearing mechanisms and indicated carriage position with an accuracy of  $\pm 0.25$  percent over the full traverse of four inches.

With the thermocouple the plenum temperature could be measured with an accuracy of  $\pm 0.01$  millivolt or  $\pm 0.3$  degree Fahrenheit. The through-flow angle potentiometers were calibrated to an accuracy of  $\pm 0.5$  degree using the protractor and vernier. The pressure transducers were calibrated by applying a known pressure and adjusting the strain-gage





bridge resistance until the readout was equal to the known pressure in engineering units. This pressure was measured with a Texas Instrument Model 141 fused-quartz bourdon-tube pressure gage, which is a secondary standard for pressure measurement and was previously calibrated at the Navy Standards Laboratory at Alameda, California. For each transducer a value of resistance could be shunted across one leg of the bridge to give a voltmeter reading corresponding to the calibrated full-scale pressure. This shunt resistance was determined by means of a decade resistor in the data system and was used to electrically calibrate the pressure transducers prior to each test. The calibration resistances were verified periodically by repeating the aforementioned calibration procedure. The full-scale reading of the pressure transducers was  $1.750 \text{ psig} \pm 0.003 \text{ psig}$  or  $1.000 \text{ psig} \pm 0.003 \text{ psig}$  depending on the pressure being measured, and the transducers were linear over the entire range. Engineering units for pressure were used to eliminate the temperature and gravity corrections of manometer readings. The cross-flow angle could be determined with an accuracy of  $\pm 2.0$  degrees from the probe calibration results.

The survey data was punched on paper tape with a Tally model 420 tape perforator for processing on the IBM 360/67 digital computer of the Naval Postgraduate School. The paper-tape data was transmitted directly to the computer via a Teletype terminal [Ref. 31]. The Government-surplus



data-logging system originally used a Flexowriter as its output device. Before it could be used with a Teletype, extensive modification of the internal logic was necessary to obtain digital output in ASCII code.

Additional data for each survey consisted of the span-wise position of the probes and ambient pressure and temperature. The ambient pressure was read from a standard Fortin-type barometer and corrected for temperature and local gravity to obtain an accuracy of  $\pm 0.005$  inch of mercury.

Experimental errors can be generally classified as fixed and random errors. The uncertainty of the experimental results was determined with the method of Kline and McClintock [Ref. 32]. The purpose of the investigation was to establish the total-pressure loss coefficient  $Y_2$  of the cascade. From Appendix A

$$Y_2 = \frac{\bar{P}_{t1} - \bar{P}_{t2}}{\bar{P}_{t1} - \bar{P}_1}$$

The uncertainties in the mass-averaged total pressures  $\bar{P}_{t1}$  and  $\bar{P}_{t2}$  and static pressure  $\bar{P}_1$  were estimated to be  $\pm 0.3$  percent and  $\pm 1.0$  percent respectively. From Ref. 32 the uncertainty interval  $w_r$  is given by the second-power equation,

$$w_r = \left[ \left( \frac{\partial Y_2}{\partial \bar{P}_{t1}} w_1 \right)^2 + \left( \frac{\partial Y_2}{\partial \bar{P}_{t2}} w_1 \right)^2 + \left( \frac{\partial Y_2}{\partial \bar{P}_1} w_2 \right)^2 \right]^{1/2}$$



where  $w_1$  and  $w_2$  are the uncertainties in the total and static pressures respectively. With the above relation the uncertainty in the total-pressure loss coefficient is of the order of four percent. Based on test results from flow survey data taken on different days, the loss coefficient had a repeatability of one percent.

In addition to the cascade tests, surveys were made of the end-wall boundary layer at the leading-edge plane of the blading and of the static-pressure distributions on the blade surface. A United Sensor Cobra-type probe was used for the boundary-layer surveys. This probe is designed for use near solid boundaries and measures total pressure and flow angle. Wall static-pressure taps near the probe access hole provided static pressure for velocity determinations. The pressures were connected to water U-tube manometers that could be read with an accuracy of  $\pm 0.05$  inch. The flow angles could be determined with an accuracy of  $\pm 0.5$  degree by a protractor and vernier on the probe mounting. Figure 11 shows the installation of the traverse mechanism on the removable Plexiglas wall.

The center blade in the cascade test section was instrumented with surface taps to provide static-pressure distributions for several spanwise positions. This was accomplished by cutting grooves into the blade surface and stacking 0.033-inch outside diameter, stainless-steel tubing, one tube for each spanwise position. Near the sensing end the tubing was bent 90 degrees so that the measuring tap was normal to the surface. The tubes were run along the blade





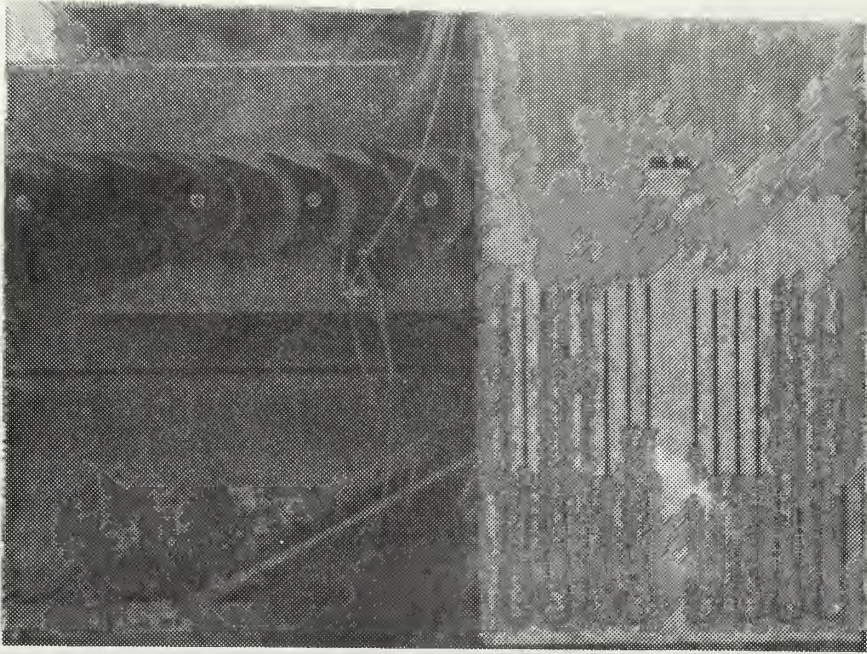


Figure 11. Installation for End-Wall Boundary-Layer Surveys.

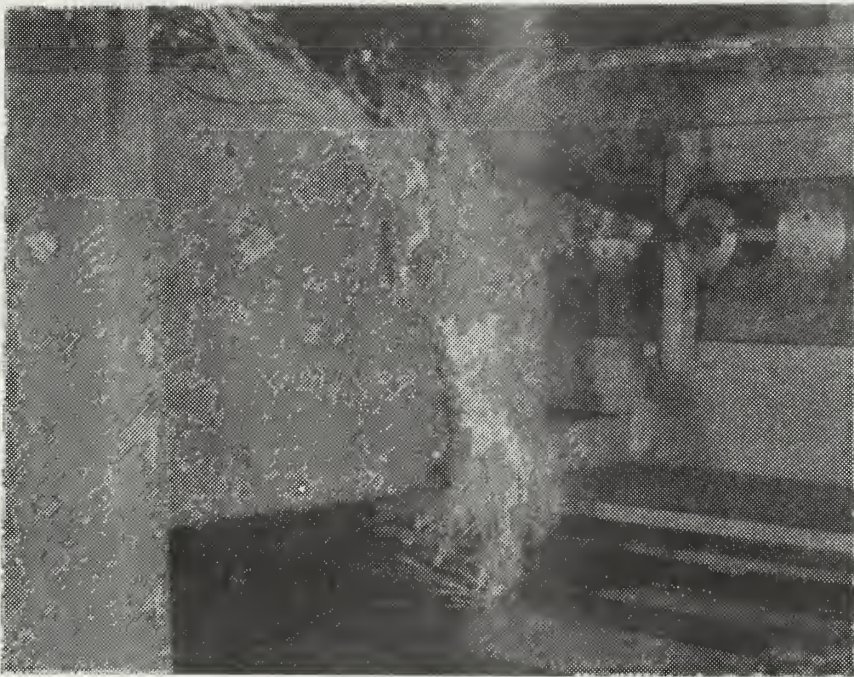


Figure 12. Tubing for Surface Static-Pressure Measurements.





span and through the cylindrical support of the blade, from where they were connected to a water-filled manometer bank. The grooves were filled with epoxy and sanded smooth to restore the surface to its original condition. Care was taken to remove all burrs from the pressure taps. Pressure data was obtained at different spanwise positions on the suction and pressure surfaces of the blade for varying blade heights, except near the leading and trailing edges where the blade was only thick enough for one tube. The instrumented blade had a total of 132 pressure taps. The surface static pressures could be read with an accuracy of  $\pm 0.05$  inch of water. The blade holder and stainless-steel and plastic tubing are shown in Fig. 12.

#### B. CHANNEL-FLOW MODEL

In Section II.C the three-dimensional flow in the passage between two neighboring blades of a turbine cascade was represented by the flow in a turning duct. Accordingly, a channel-flow model was designed and tested to investigate the effect of increasing deflection angle on the secondary-flow losses. The model had a five-inch square cross section, and the curved walls were concentric circular arcs with ten-inch and 15-inch radii. The upper and lower walls of the model, that correspond to the end walls of the cascade, were made of 5/8-inch Plexiglas; and the curved walls consisted of 1/16-inch aluminum sheets. Sections with 90, 110, and 135 degrees of turning were tested. Straight sections with the same wetted area as the curved sections were also



tested for comparison. The straight sections gave a two-dimensional flow loss; and the curved sections gave a total flow loss, the difference between the two being the additional three-dimensional or secondary loss.

Prior to testing the channel-flow model, it was necessary to design a plenum system to produce the desired uniform inlet flow conditions ahead of the model. The so-called Model-Testing Facility consists of two tanks; one with a height of nine feet, the other with a height of six feet, both have a diameter of 42 inches. Compressed air is supplied to the large tank from the Allis-Chalmers compressor through an existing ASME standard orifice installation for flow-rate determination. The line connecting the two tanks contains a smaller ASME standard orifice installation which is used for a more accurate determination of lower flow rates. Flow straighteners were placed at the inlets to the tanks to provide an axial entry velocity. Long, conical diffusers then reduce the inlet velocity to near zero, so the tanks act as plenum chambers. The ten-inch diameter outlets from the tanks are fitted with elliptically contoured bellmouths to produce uniform exit flow conditions. The facility has been used for several types of flow-model investigations as well as for the probe calibrations described in Section III.A.

The channel-flow model was mounted on the large plenum tank using a ten- to eight-inch pipe reducer and an available pipe section that provided a transition from an eight-inch



circular cross section to a five-inch square cross section. Surveys at the inlet to the model showed that the boundary-layer thicknesses were of the order of one percent of the cross section; thus, entry flow conditions were essentially uniform due mainly to the acceleration produced by the transition pipe.

Inlet total pressure was measured at the axis of the model with a Kiel probe. The average static pressure at the exit was obtained with a combination of two wall taps located 1/16 inch from the outlet plane of the model on the centerlines of the aluminum sides. Both pressures were connected to U-tube manometers, which could be read with an accuracy of  $\pm 0.1$  centimeter of water.

In Appendix B the axial force exerted by the flow on a flat plate perpendicular to the model exit is related to the loss in kinetic energy through the model. The force plate consisted of an aluminum sheet, 20 inches square and 1/8 inch thick, and it was mounted on ball-bearing guides to minimize frictional effects on the measured force. A knife-edge transmitted the force to the center of a simply supported aluminum beam, which had a full strain-gage bridge on either side of the loading point. The bridge outputs were calibrated in units of pounds force and were read from a digital voltmeter. Although the voltmeter provided a reading accuracy of  $\pm 0.1$  pounds, the uncertainty in the measured force on the plate, which was taken as the average of the readings from the two bridges, was estimated to be  $\pm 1.0$



percent due to hysteresis. Above 65 pounds force on the plate, the beam exceeded its elastic limit; so this value was used as an upper limit for the tests.

The force plate and beam were fixed to a movable support, which was positioned for each test and then clamped to the floor. The proper distance between the force plate and the outlet plane of the model, as established by tests, was nine inches. Smaller distances influenced upstream pressure measurements. The channel-flow-model installation for the 90-degree curved section is shown in Fig. 13.





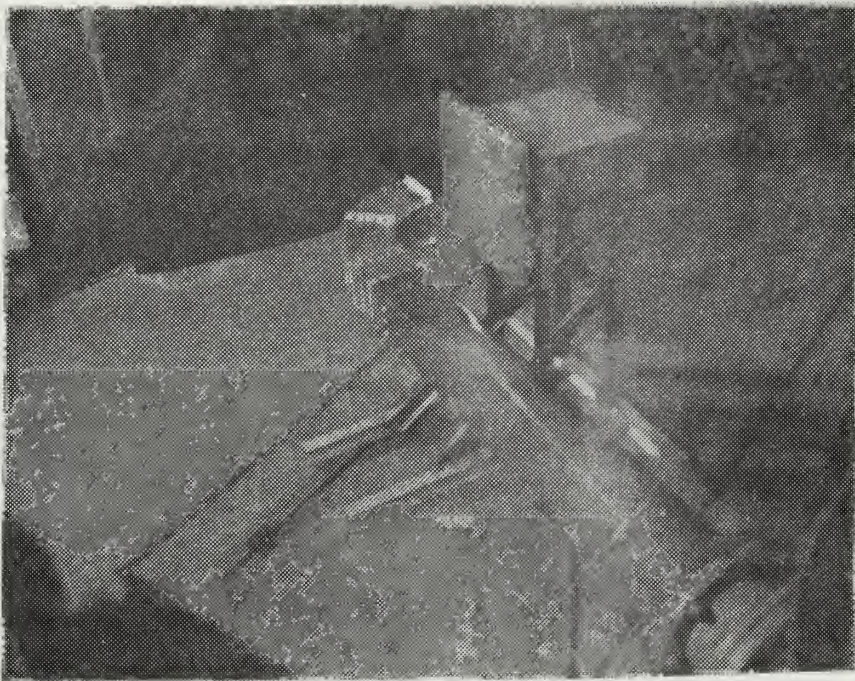


Figure 13. Channel-Flow-Model Installation for 90-Degree Curved Section.



#### IV. RESULTS AND DISCUSSION

##### A. CASCADE TESTS

The method that was utilized for the reduction of cascade test data is given in Appendix A. Flow conditions were investigated for blade heights of 7.0, 6.0, 5.0, and 4.0 inches using the traversing technique described in Section III.A. To establish the most appropriate interval at which data were taken for these traverses, two tests were made at intervals of 0.05 inch. Comparing the results calculated for this interval and those obtained by deleting every other data point, it could be seen that the differences were insignificant. For example, whereas the total-pressure loss coefficient for an interval of 0.05 inch was 0.1264, it became 0.1262 if the interval was 0.10 inch. Hence, a traversing interval of 0.10 inch was used.

In order to correlate tests at the various spanwise positions made at different times, the same average ratio of absolute plenum pressure to ambient pressure was maintained. With the blower running at high speed, this pressure ratio had a value of  $1.096 \pm 0.002$ . The Reynolds number was essentially the same for the four cascade configurations. Based on the mass-averaged exit velocity and the blade chord, the Reynolds number was approximately  $1.4 \times 10^6$ .

The spanwise distributions of the total-pressure loss coefficient  $Y_2$  and the kinetic-energy loss coefficient  $\zeta_2$ ,



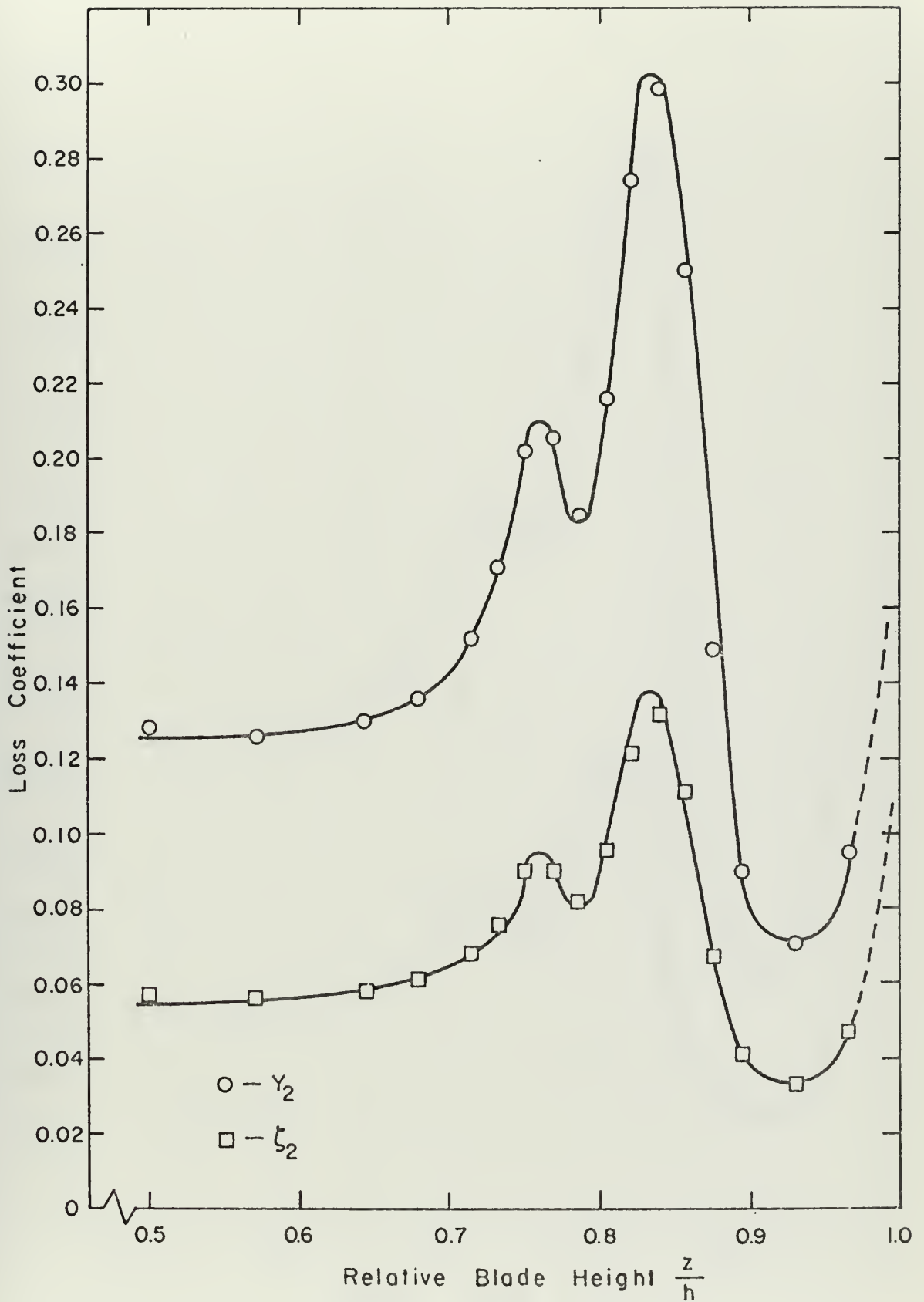


Figure 14. Spanwise Distributions of Loss Coefficients  $Y_2$  and  $\zeta_2$  for  $h = 7.0$  inches ( $h/c = 1.036$ ).



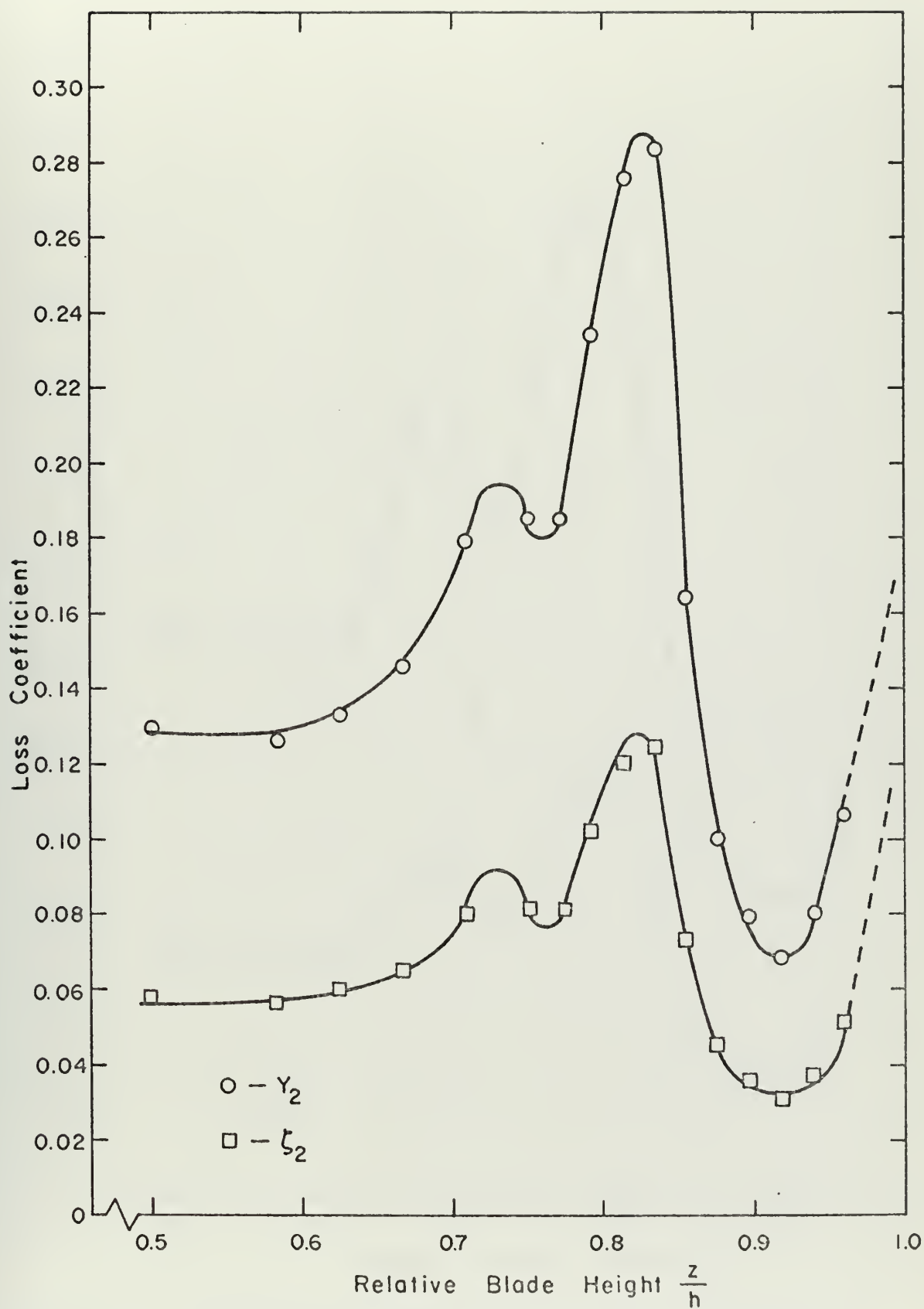


Figure 15. Spanwise Distributions of Loss Coefficients  $Y_2$  and  $\zeta_2$  for  $h = 6.0$  inches ( $h/c = 0.888$ ).





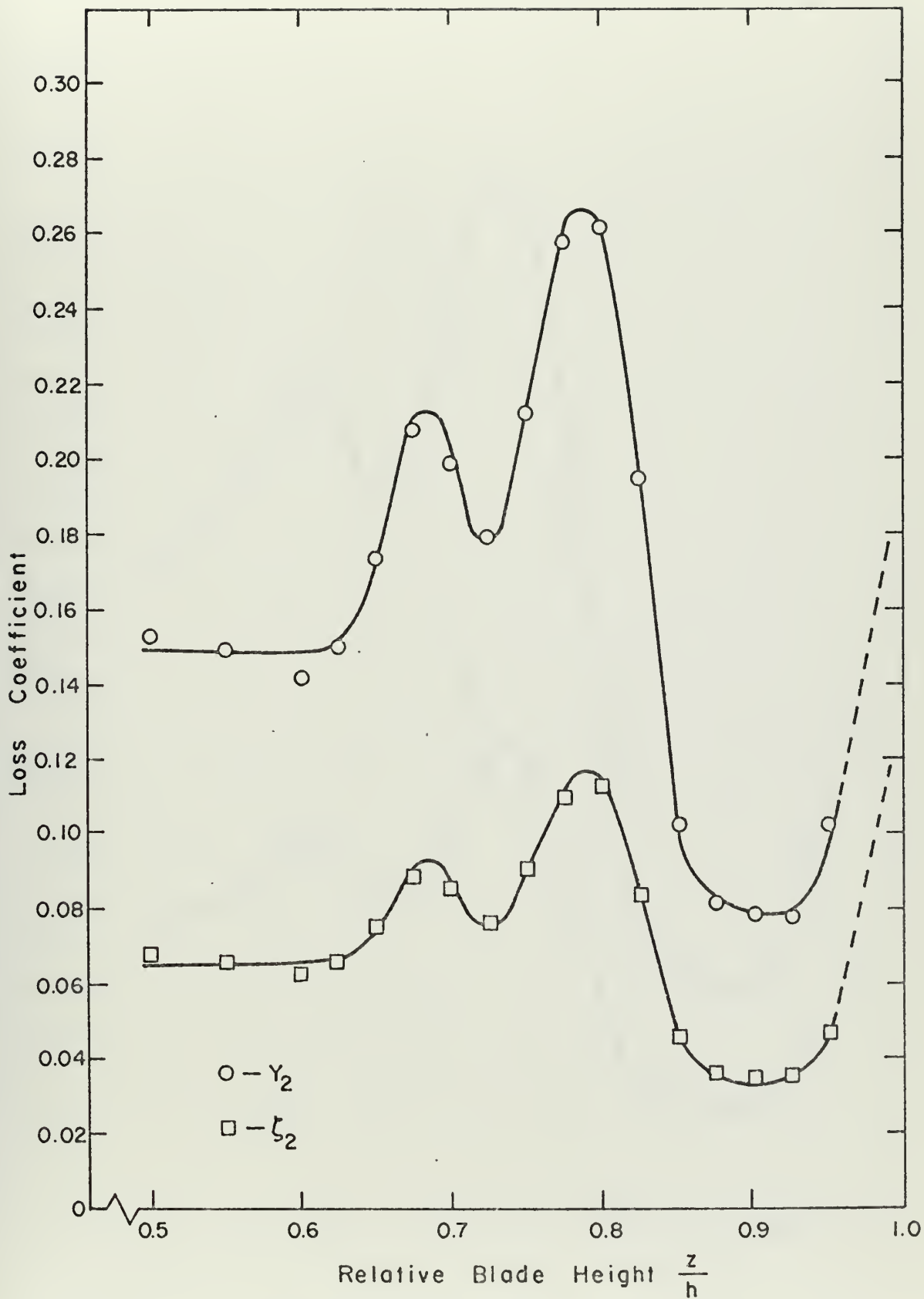


Figure 16. Spanwise Distributions of Loss Coefficients  $Y_2$  and  $\zeta_2$  for  $h = 5.0$  inches ( $h/c = 0.740$ ).



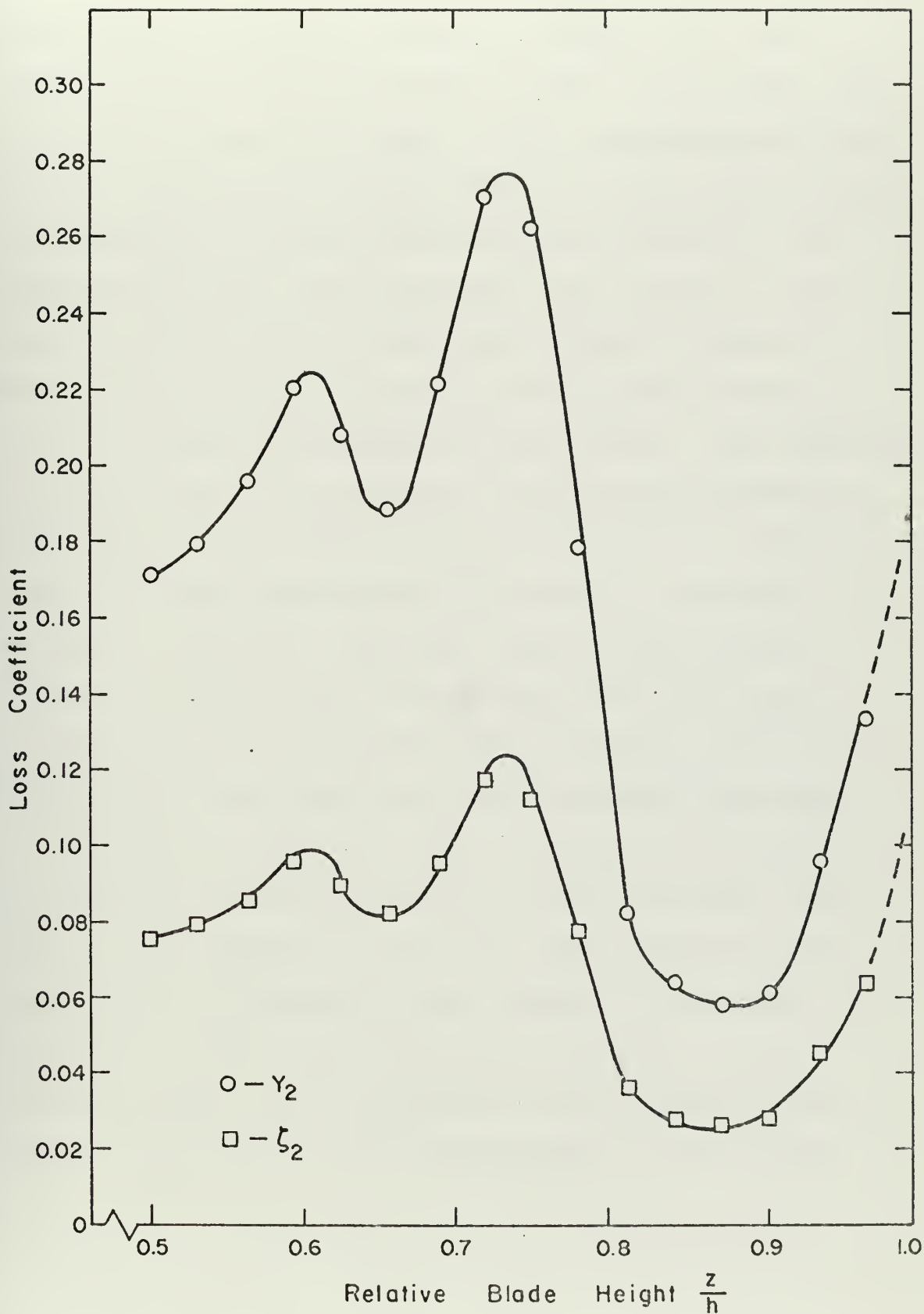


Figure 17. Spanwise Distributions of Loss Coefficients  $\gamma_2$  and  $\zeta_2$  for  $h = 4.0$  inches ( $h/c = 0.592$ ).



which are defined by Eqs. A8 and A9 respectively, were plotted over half the blade span for each blade height and are shown in Figs. 14 through 17. The characteristics that the loss distributions had in common were two definite peaks at intermediate values of relative blade height  $z/h$ , one considerably higher than the other, and a region of lower loss near the end wall. There was a region of constant loss near mid-span of the blading that became smaller and finally vanished for decreasing blade heights. The magnitude of the mid-span loss coefficient increased with decreasing blade height, which must be due to the effects of secondary flows. The three-dimensional flow also had the effect of moving the loss peaks relatively closer to the mid-span location as blade height was reduced; hence, the size of the lower-loss region near the wall increased. However, in each case the loss coefficient at the end wall increased.

Total loss coefficients were calculated by integrating the spanwise distributions along the relative blade height. Overall loss coefficients were also obtained for the flow conditions far downstream of the cascade, as described in Appendix A. These loss coefficients are given in the following table, which includes the results from the preliminary tests for the full blade height of 10.0 inches.



## TOTAL LOSS COEFFICIENTS

Blade Height	$Y_{2t}$	$Y_{3t}$	$\zeta_{2t}$	$\zeta_{3t}$
*10.0	0.1650	0.1656	0.0661	0.0664
7.0	0.1501	0.1700	0.0674	0.0771
6.0	0.1515	0.1728	0.0678	0.0782
5.0	0.1592	0.1814	0.0695	0.0800
4.0	0.1615	0.1866	0.0708	0.0826

\*The results for the ten-inch blade height were obtained for exit surveys at the upper outlet measuring station.

This table shows that the total-pressure loss coefficient  $Y_{2t}$  increased by only 1.1 percent if the blade height was decreased from 7.0 inches to 4.0 inches, and the increase in the kinetic-energy loss coefficient  $\zeta_{2t}$  was only 0.3 percent. The difference between the total loss coefficient based on exit flow conditions, which is denoted by the subscript 2t, and that based on conditions far downstream, with subscript 3t, is the so-called mixing loss. The results for the ten-inch blade height were obtained for exit surveys at the upper outlet measuring station, and the above table shows that the mixing loss was negligible. Thus, the flow at this measuring station nearly corresponded to conditions far downstream. For the other four configurations, the total-pressure mixing loss increased from 2.0 percent for the seven-inch blade height to 2.5 percent for the four-inch blade height; while the kinetic-energy mixing loss increased from 1.0 percent to 1.2 percent.

Similar to Ref. 33 the overall total-pressure loss coefficient  $Y_{2t}$  was considered to be the sum of the two-dimensional loss  $Y_{2-d}$ , a constant for a given blade profile, and the secondary loss  $Y_s$ . This separation of losses is





consistent with the definition of secondary flow in a cascade given in Section II.A. Since the flow at the blade mid-span was less subject to three-dimensional effects, the total-pressure loss coefficient calculated from the mid-span traverse data for each cascade configuration was plotted versus the ratio of blade chord  $c$  to blade height  $h$ , the inverse of aspect ratio, on a semi-logarithmic scale. The two-dimensional loss coefficient was determined by extrapolating to infinite blade height. As shown in Fig. 18, a value of 0.090 was obtained for the two-dimensional loss coefficient. In order to use the results from the preliminary tests for the ten-inch blade height, an estimated mixing loss of two percent was subtracted from the computed loss coefficients.

The difference between the total loss and the two-dimensional loss gave the secondary loss coefficient for each case. In Fig. 19 the ratio of secondary loss to overall loss is depicted as a function of inverse aspect ratio. The loss in total pressure associated with secondary flow increased from 38.1 percent of the overall total-pressure loss for a blade height of ten inches to 44.3 percent for the four-inch blade height. Also shown in Fig. 19 is the ratio of secondary loss to two-dimensional loss, which increased from 61.4 percent to 79.4 percent as the blade height was decreased from ten inches to four inches. The separation of the overall loss into the two-dimensional loss and the secondary loss for each blade height is depicted in Fig. 20.



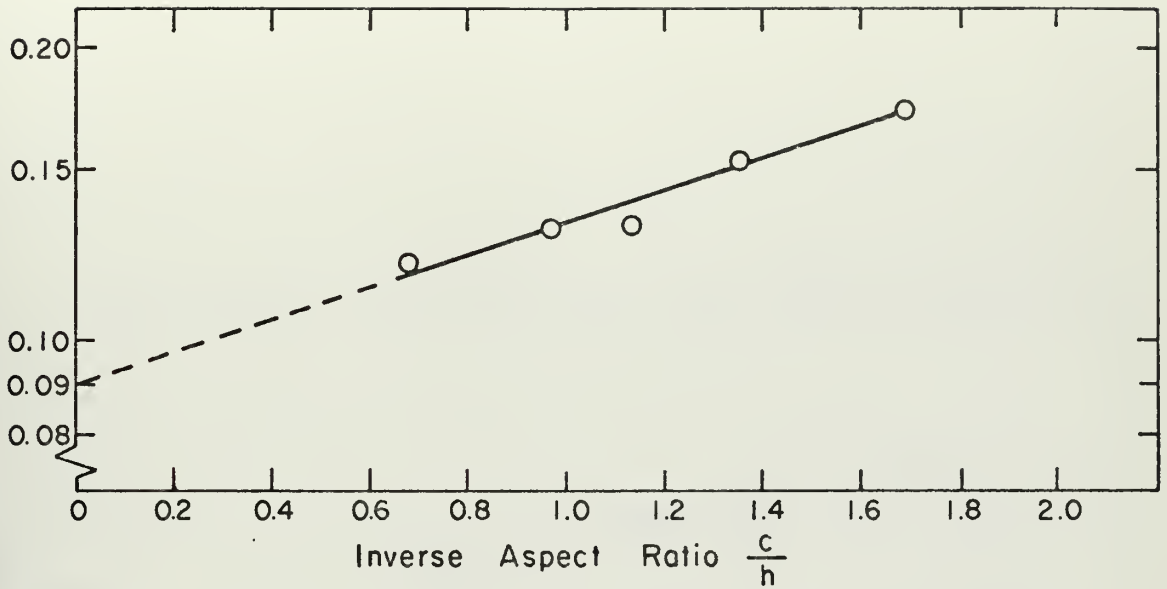


Figure 18. Mid-Span Total-Pressure Loss Coefficient.

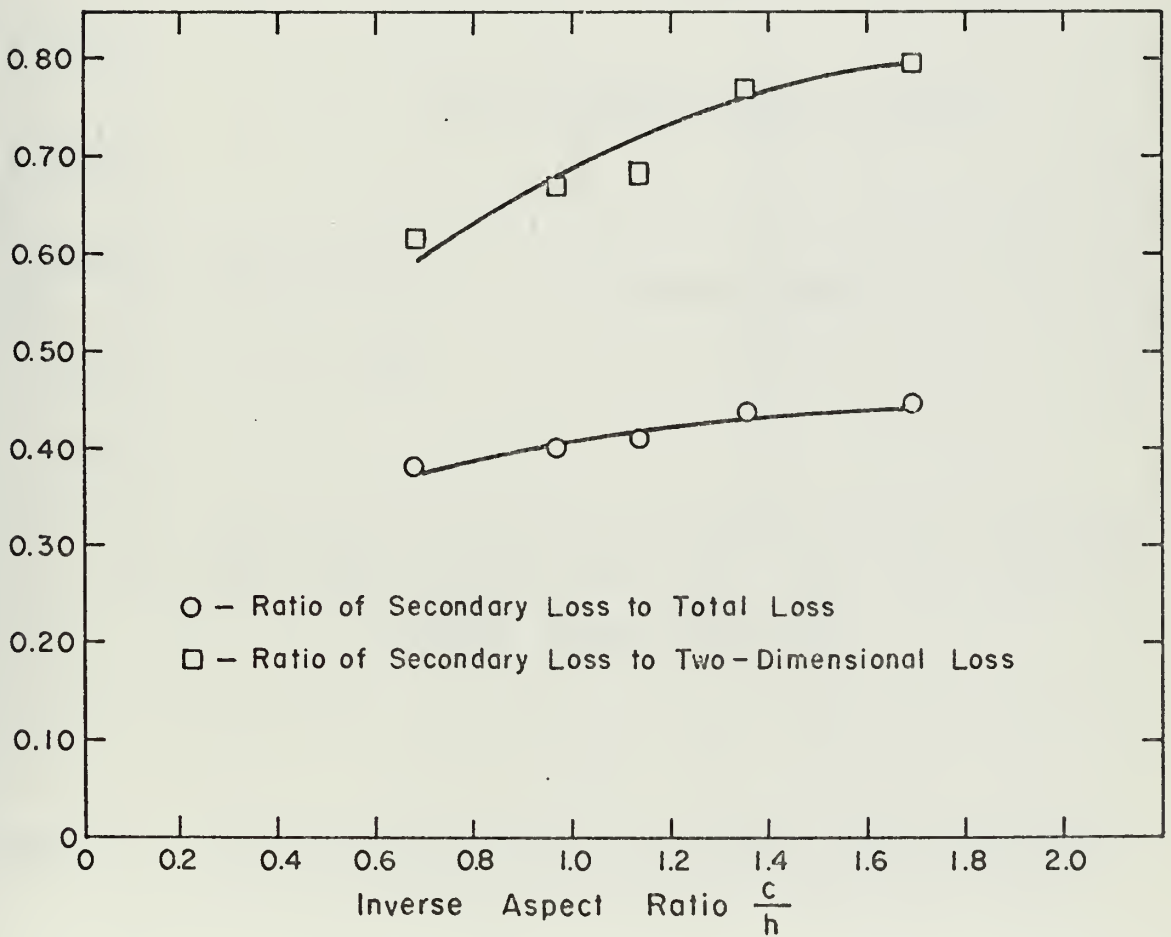


Figure 19. Variation of Secondary Loss in Total Pressure with Blade Height.



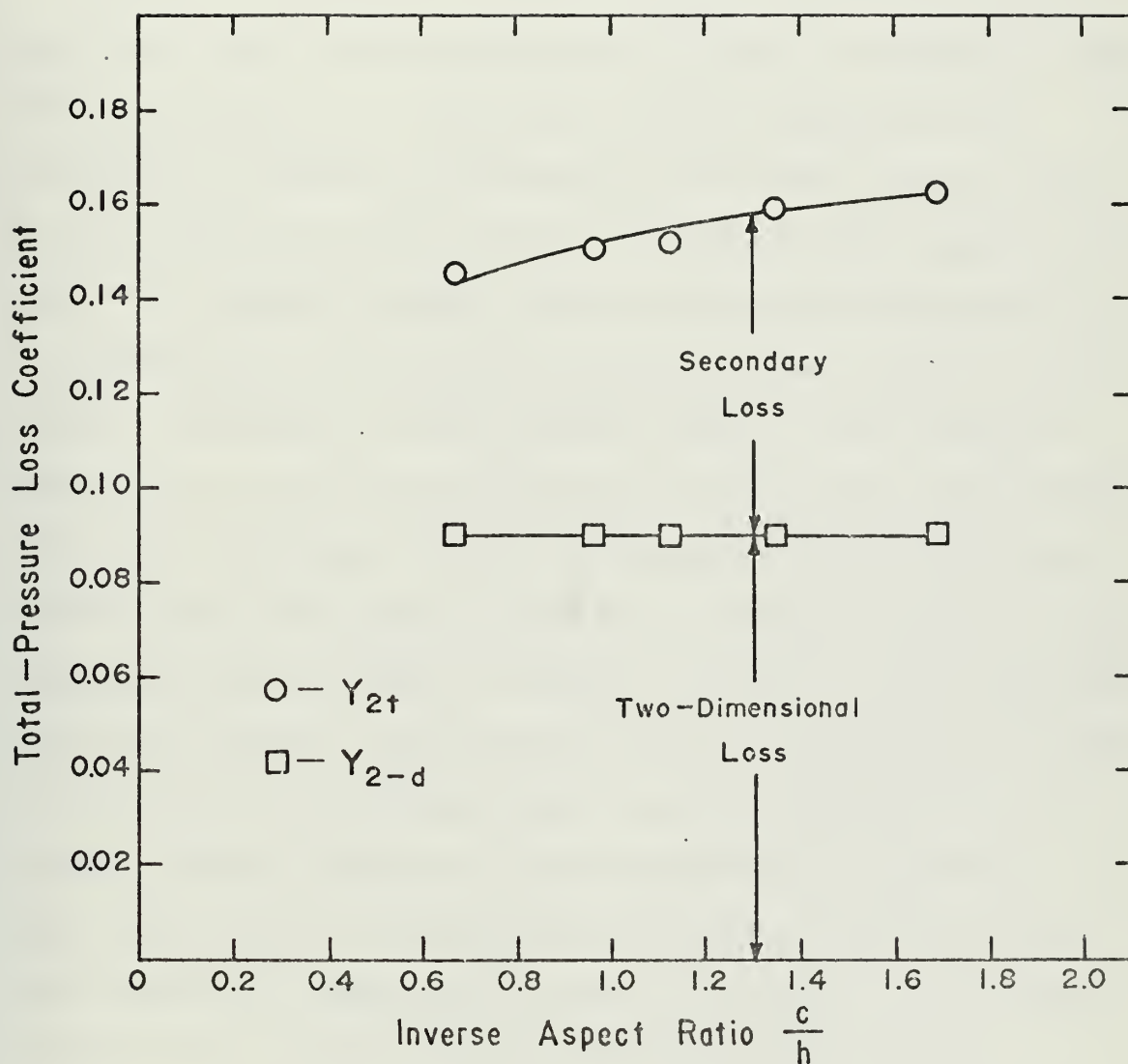


Figure 20. Separation of Overall Loss into Two-Dimensional Loss and Secondary Loss for Each Blade Height.



Since the blade height was varied for this investigation while the chord and spacing were held constant, plots similar to those shown in Figs. 18, 19, and 20 were obtained using blade-spacing-to-height ratio as abscissa.

Contours of constant relative total pressure in the outlet plane of the cascade are given in Figs. 21 through 24 for half the blade span. The effects of the secondary-flow phenomena in cascades are apparent from these contour plots. The exit relative total pressure is given by  $(\bar{P}_{t1} - P_{t2}) / (\bar{P}_{t1} - \bar{P}_1)$ , where the overscore denotes mass-averaged quantities and  $P_{t2}$  is the measured outlet total pressure at each point in the surveys. Therefore, at the larger values on the contours there existed a low total pressure at the outlet. The accumulation of fluid with low total pressure and therefore low velocity near the corner formed by the suction surface of the blading and the end wall is evident in Fig. 21. As the blade height was reduced, the relative position of the core of low-momentum fluid was further away from the end wall, Fig. 24. In each case the centers of the regions with low-energy fluid corresponded to the points of maximum total-pressure loss coefficient depicted in Figs. 14 through 17. From the contour plots it can be seen that the secondary flow influences the flow in the blade passage as well as that in the suction-surface boundary layer. This influence was also seen in the flow surveys as a considerable increase of the wake size in the region of the low-total-pressure core.

Visual indications of the boundary-layer flow patterns were obtained by coating the surfaces of the blade and the





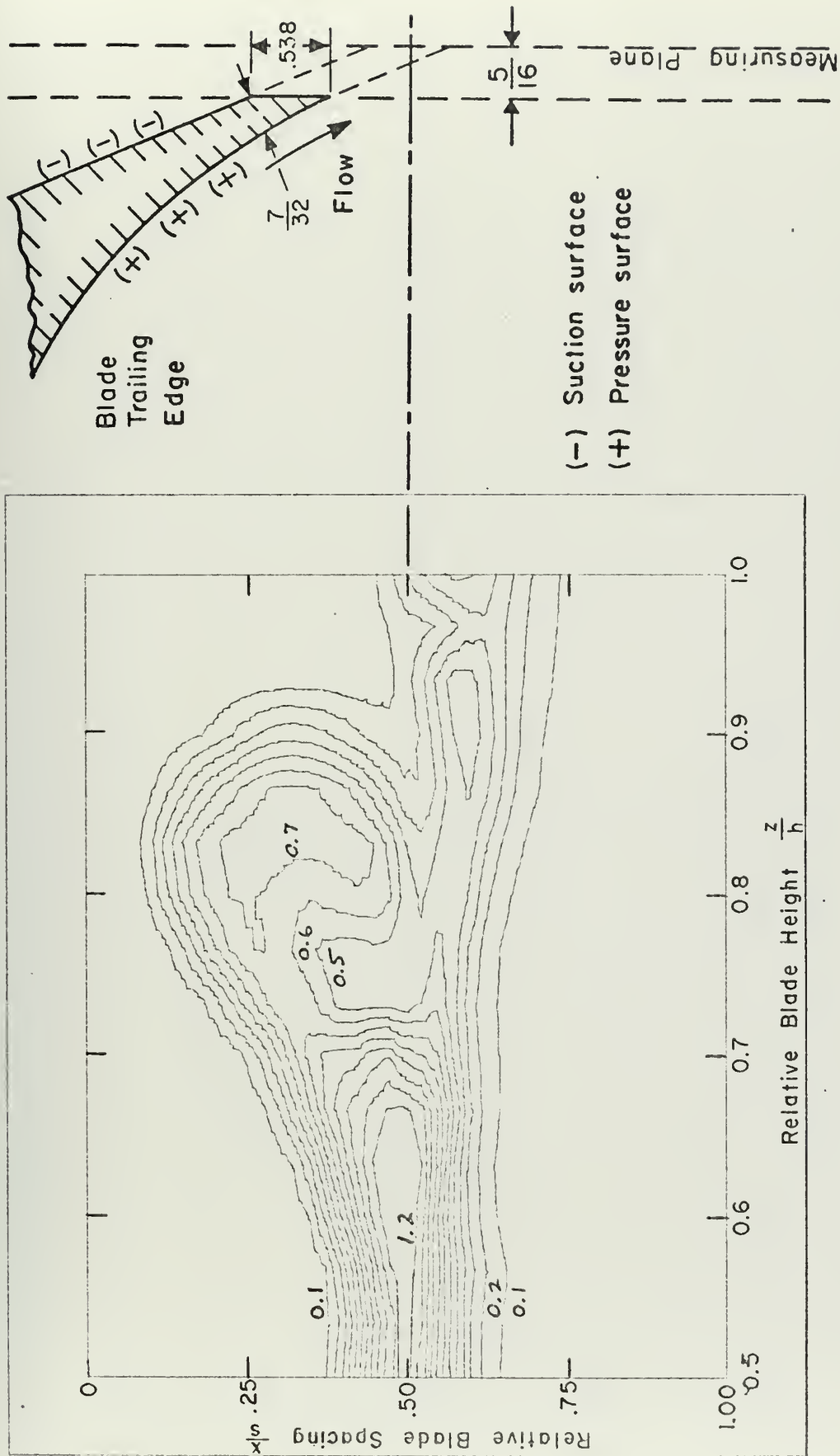


Figure 21. Contours of Constant Relative Total Pressure at Cascade Exit for  $h = 7.0$  inches ( $h/c = 1.036$ ).



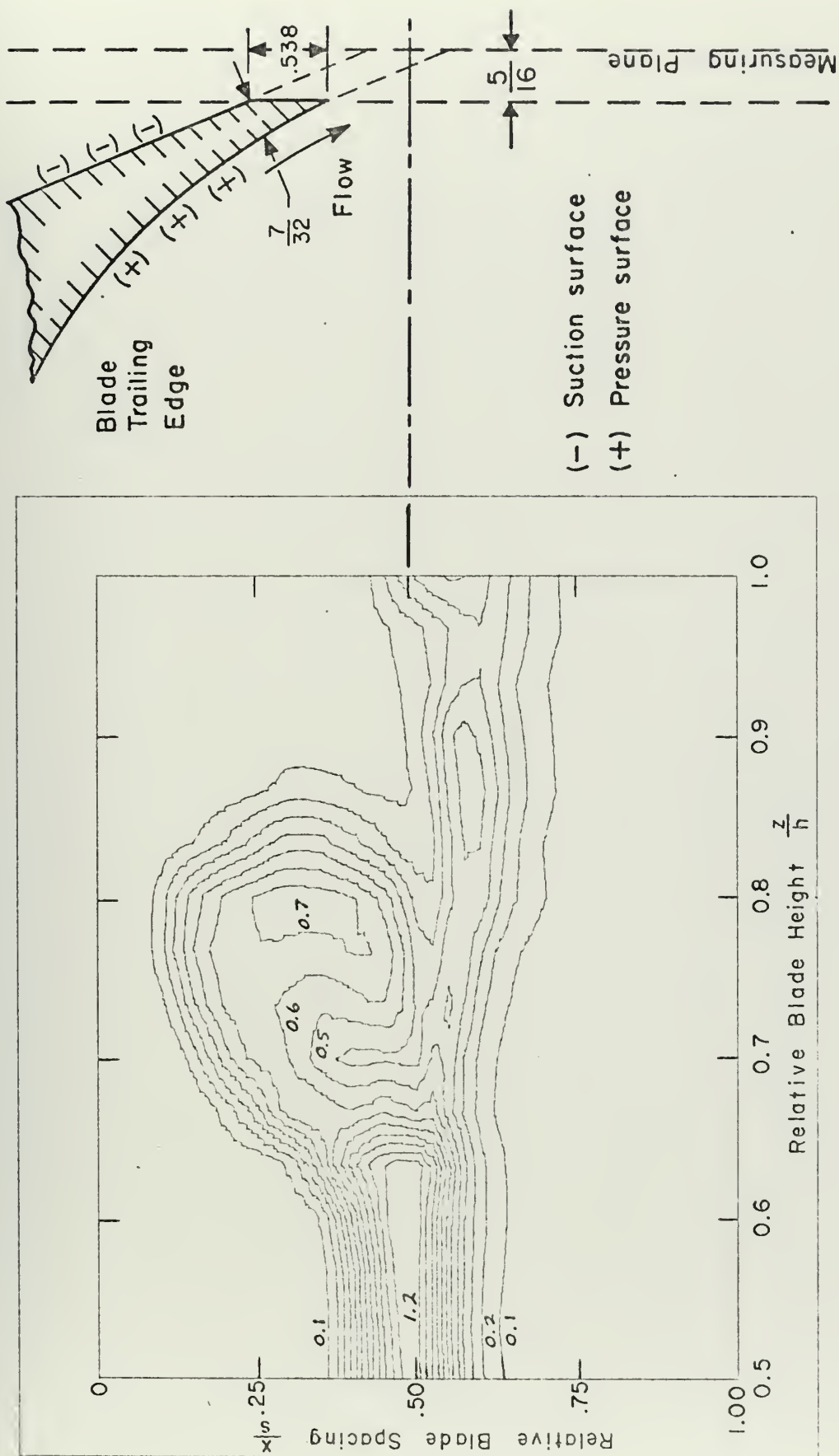


Figure 22. Contours of Constant Relative Total Pressure at Cascade Exit for  $h = 6.0$  inches ( $h/c = 0.888$ ).



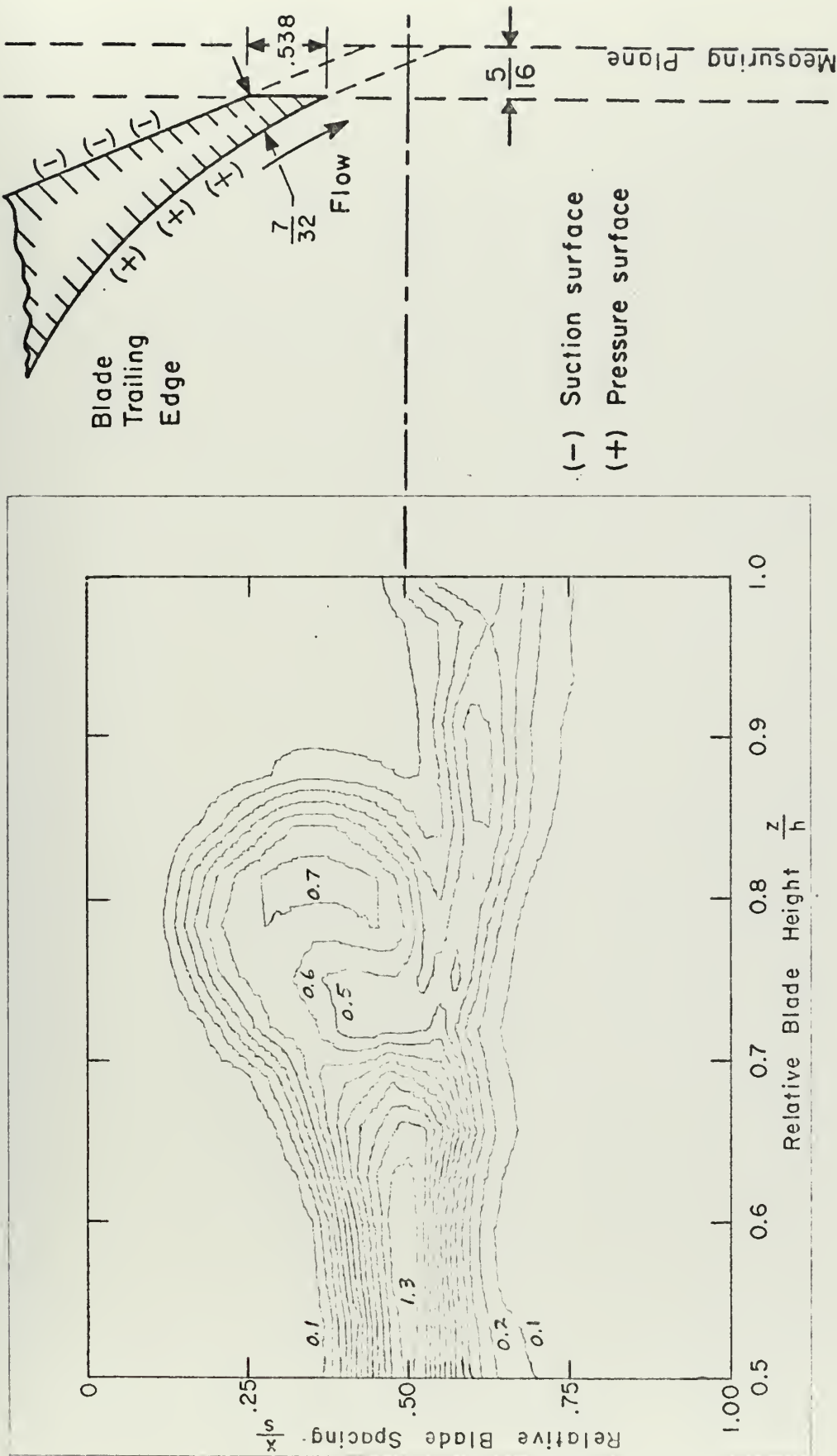


Figure 23. Contours of Constant Relative Total Pressure at Cascade Exit for  $h = 5.0$  inches ( $h/c = 0.740$ ).



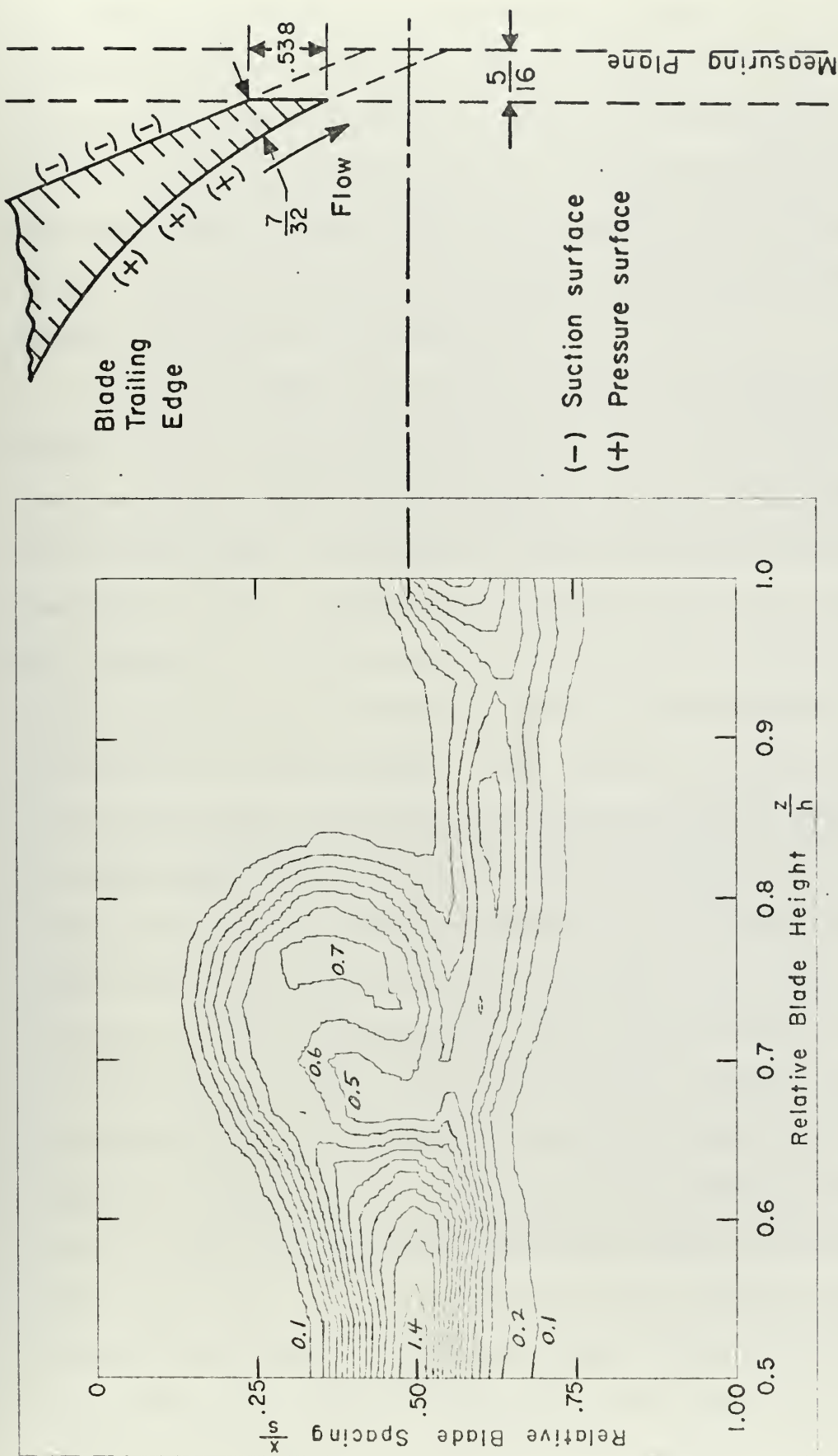


Figure 24. Contours of Constant Relative Total Pressure at Cascade Exit for  $h = 4.0$  inches ( $h/c = 0.592$ ).





end wall with a mixture of lampblack, light oil, and kerosene. Since the coating was wet, part of it was carried away by the flow, thus producing patterns of the streamline paths in the vicinity of the coated surfaces. Essentially the same flow patterns were obtained for each cascade configuration. Therefore, only the results for the four-inch blade height are presented in Figs. 25 through 29.

Figure 25 shows that the fluid particles near the end wall moved from the pressure side of the blade passage to the suction side. This process started at the leading edge of the blading near the pressure surface and continued to the passage throat. The end-wall boundary layer was surveyed at two stations in the plane through the blade leading edges. These stations were located  $\frac{1}{2}$  inch on either side of the midpoint of the blade passage. The results of these surveys were practically the same for the four cascade configurations. The measured flow angle had a maximum variation of only one degree through the boundary layer. The boundary layer was quite small and had a thickness of about 0.24 inch. Integrating the velocity distribution gave a displacement thickness of 0.046 inch. Hence, the ratio of displacement thickness  $\delta_1$  to boundary-layer thickness  $\delta$  was 0.19. Based on the average freestream velocity and the distance from the leading edge of the end wall, the Reynolds number was about  $1.4 \times 10^6$ . The ratio  $\delta_1/\delta$  has a value of 0.34 using the Blasius solution for laminar flow along a flat plate and a value of 0.125 using the  $1/7^{\text{th}}$ -power law for a turbulent velocity profile. Considering the Reynolds number and the comparison of these



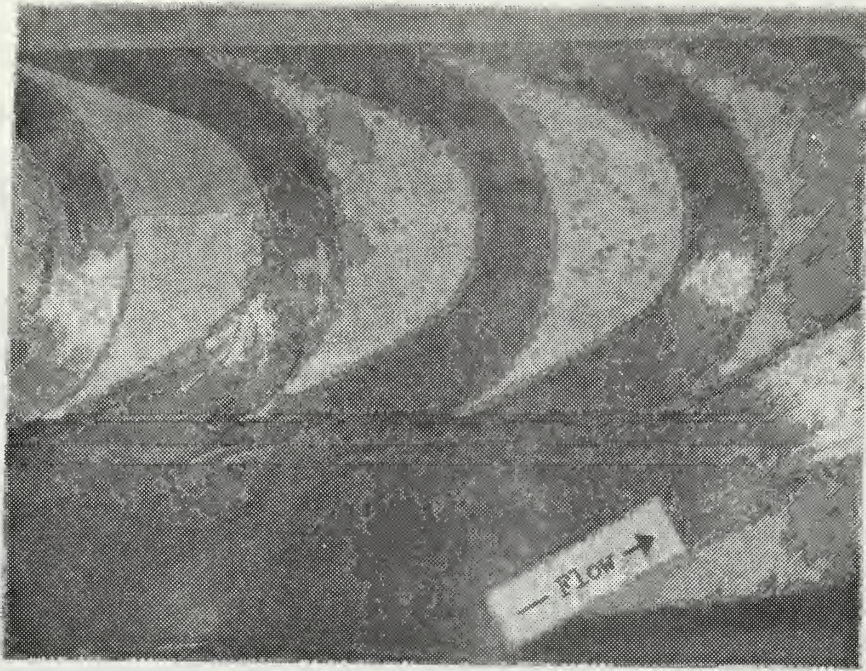


Figure 25. Boundary-Layer Flow Pattern on End Wall.

— Flow →



Figure 26. Boundary-Layer Flow Pattern on Pressure Surface.





values for  $\delta_1/\delta$ , it can be concluded that the end-wall boundary layer was turbulent.

In Figs. 26 through 29 the full blade height of four inches is shown. The lampblack pattern on the blade pressure surface of Fig. 26 shows that the flow in this region was two-dimensional, and there was no evidence that pressure-side boundary-layer fluid flowed into the blade passage at the end walls. The flow pattern of Fig. 27 shows a local separation and reattachment at the leading edge of the suction surface. From Fig. 27 it can also be seen that the cascade secondary flow started to form at point A of Fig. 30, where the tangent to the circular arc and straight surface coincide. At a point slightly further downstream, cross-flow in the suction-side boundary layer appeared, as shown in Fig. 28. It was at this point that the corner secondary flow started to form. Figure 29 shows the lampblack pattern in the trailing-edge region of the suction surface. The formation of these secondary flow patterns was observed through the Plexiglas end wall, and the effects of the cascade secondary vortices and the corner vortices were seen as collections of the lampblack material on the blade suction surface. In Figs. 28 and 29 the location of the corner vortices is shown by the darker lines that form the boundary between the cross-flow region near the end wall and the main body of the flow. The cascade secondary vortices are located inboard of the corner vortices and slightly closer to the blade mid-span. Cross-flow angles as large as 30 degrees were measured in the blade wake region at the spanwise position corresponding to the location of the corner vortex.



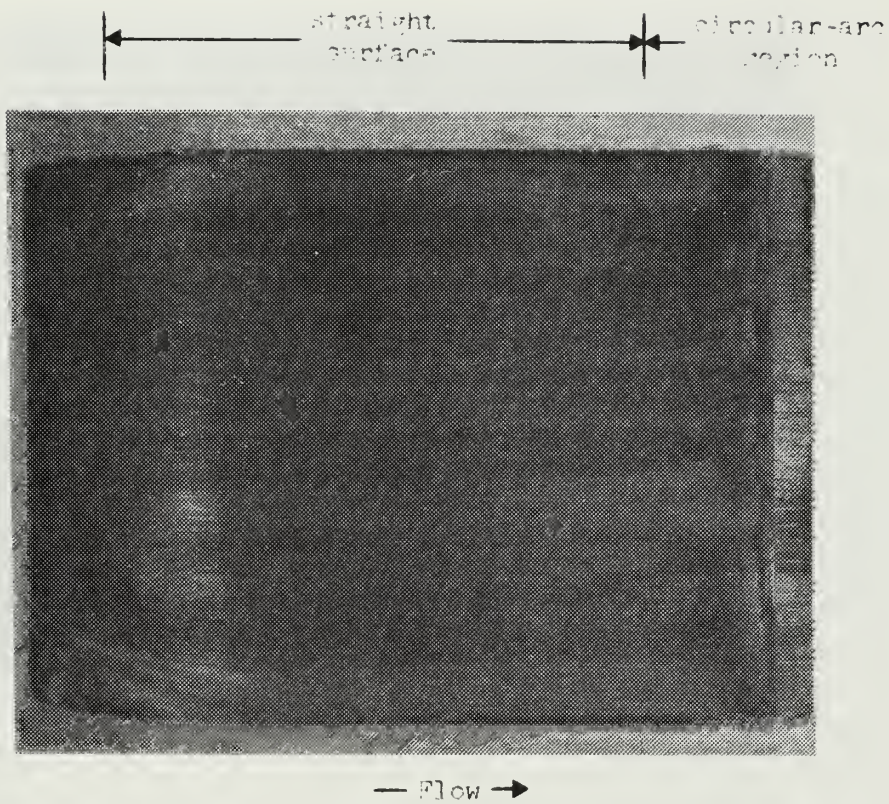
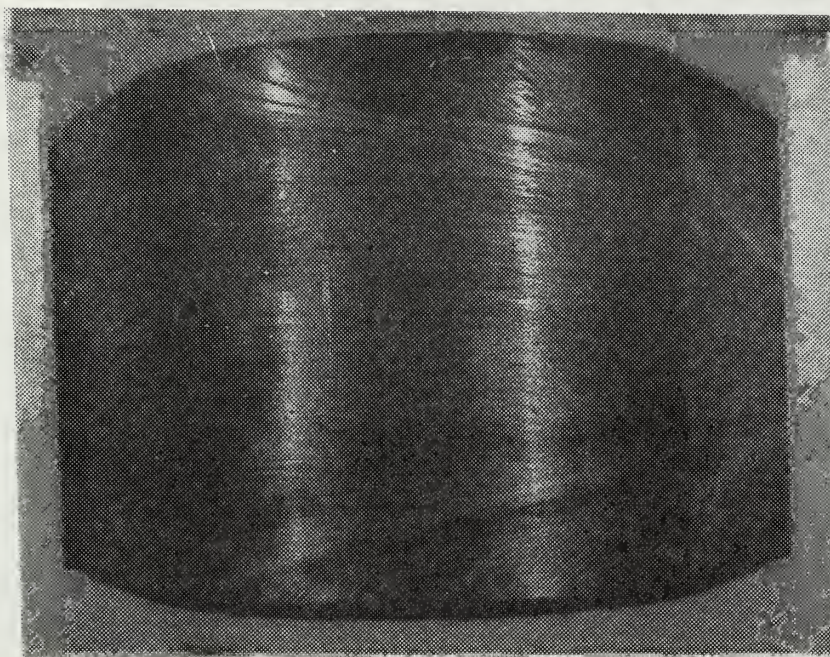


Figure 27. Boundary-Layer Flow Pattern on Suction Surface in Leading-Edge Region.





straight surface      circular-arc portion      straight surface



— Flow →

Figure 28. Boundary-Layer Flow Pattern on Suction Surface in Mid-Chord Region.



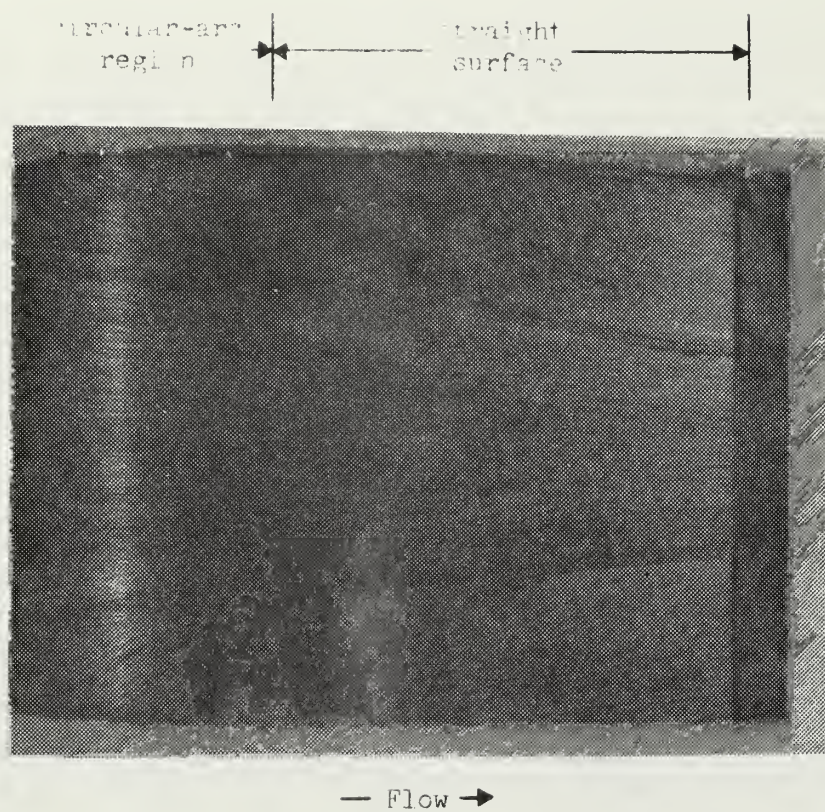


Figure 29. Boundary-Layer Flow Pattern on Suction Surface in Trailing-Edge Region.





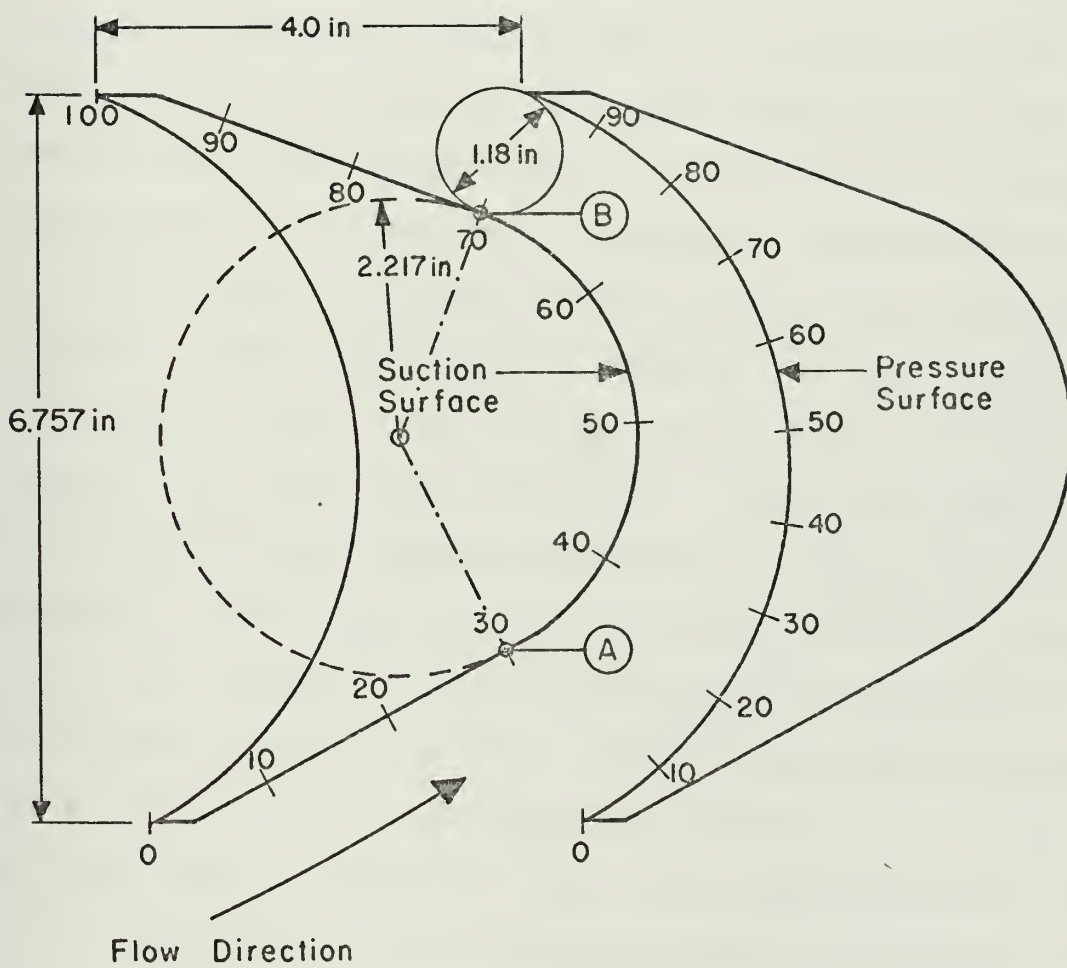


Figure 30. Percent-Surface Coordinates for Cascade Blade.



Static-pressure distributions on the blade surface at various spanwise positions are depicted in Figs. 31 through 34 for the four values of blade height. Figure 30 shows the relation between the blade passage geometry and points on the pressure-distribution curves. As the figures show, the pressure distributions were quite similar. Due to passage convergence, the flow over the pressure surface accelerated from the leading edge to the trailing edge. The static-pressure variations along the blade height on the pressure side were insignificant. Figure 26 also shows the uniformity of the flow over the pressure surface of the blade.

Points A and B of Fig. 30 denote discontinuities in the curvature of the blade suction surface. As shown in Figs. 31 through 34, the flow over the suction side accelerated smoothly from the region downstream of the local separation at the leading edge through the point A. The minimum static pressure on the suction surface occurred at a point located about seven percent of the surface coordinate upstream of the passage throat at point B. There was a sudden increase in the static pressure in the region of point B. At the mid-span plane of the blade there was a small decrease and then an increase in static pressure near the trailing edge on the suction side. The unequal pressures at the blade trailing edge were indicative of the different velocities in this region over the suction and pressure surfaces. Compared to mid-span pressure loading, there was a slight decrease in loading at the intermediate spanwise position





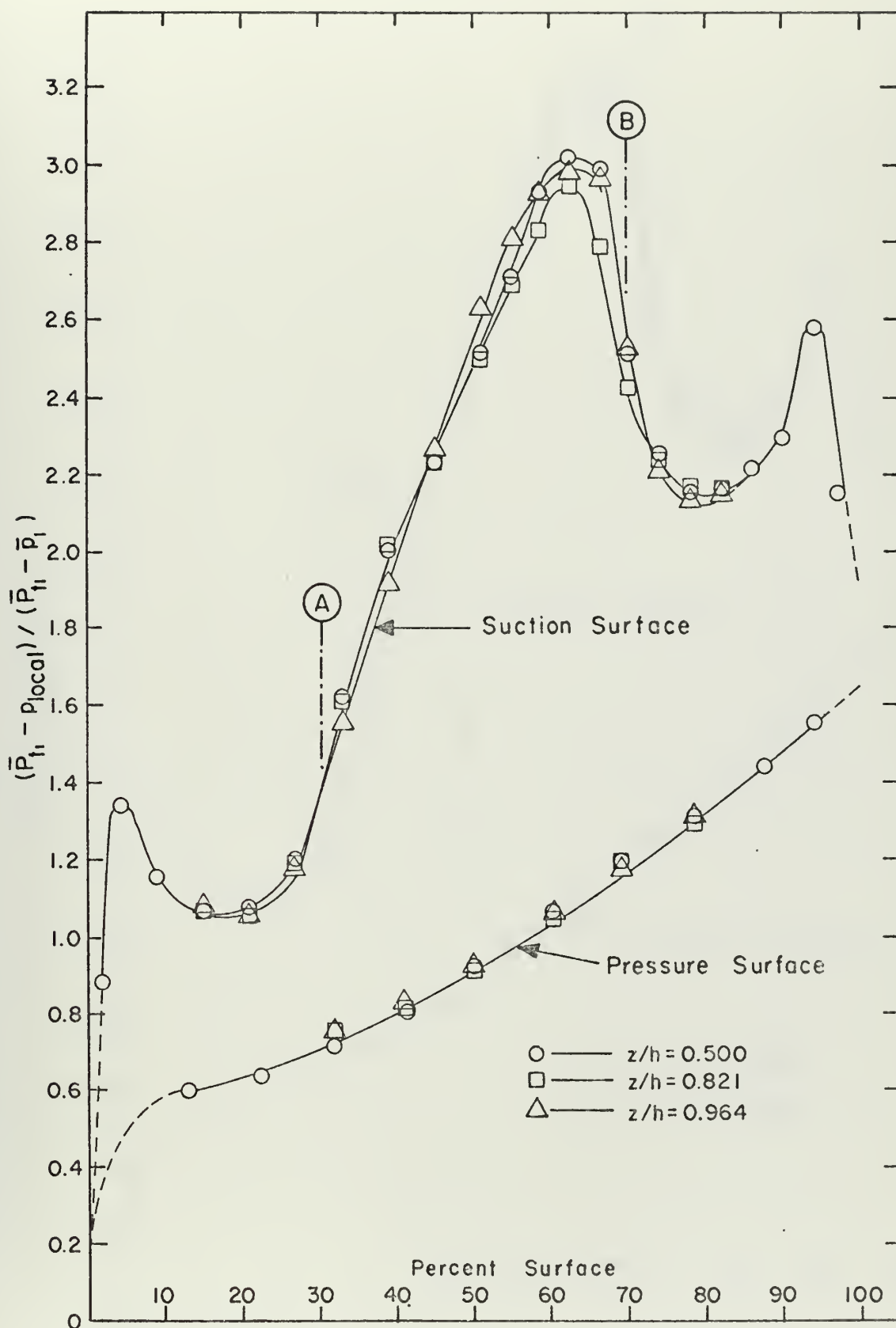


Figure 31. Static-Pressure Distributions on Blade Surface for  $h = 7.0$  inches ( $h/c = 1.036$ ).



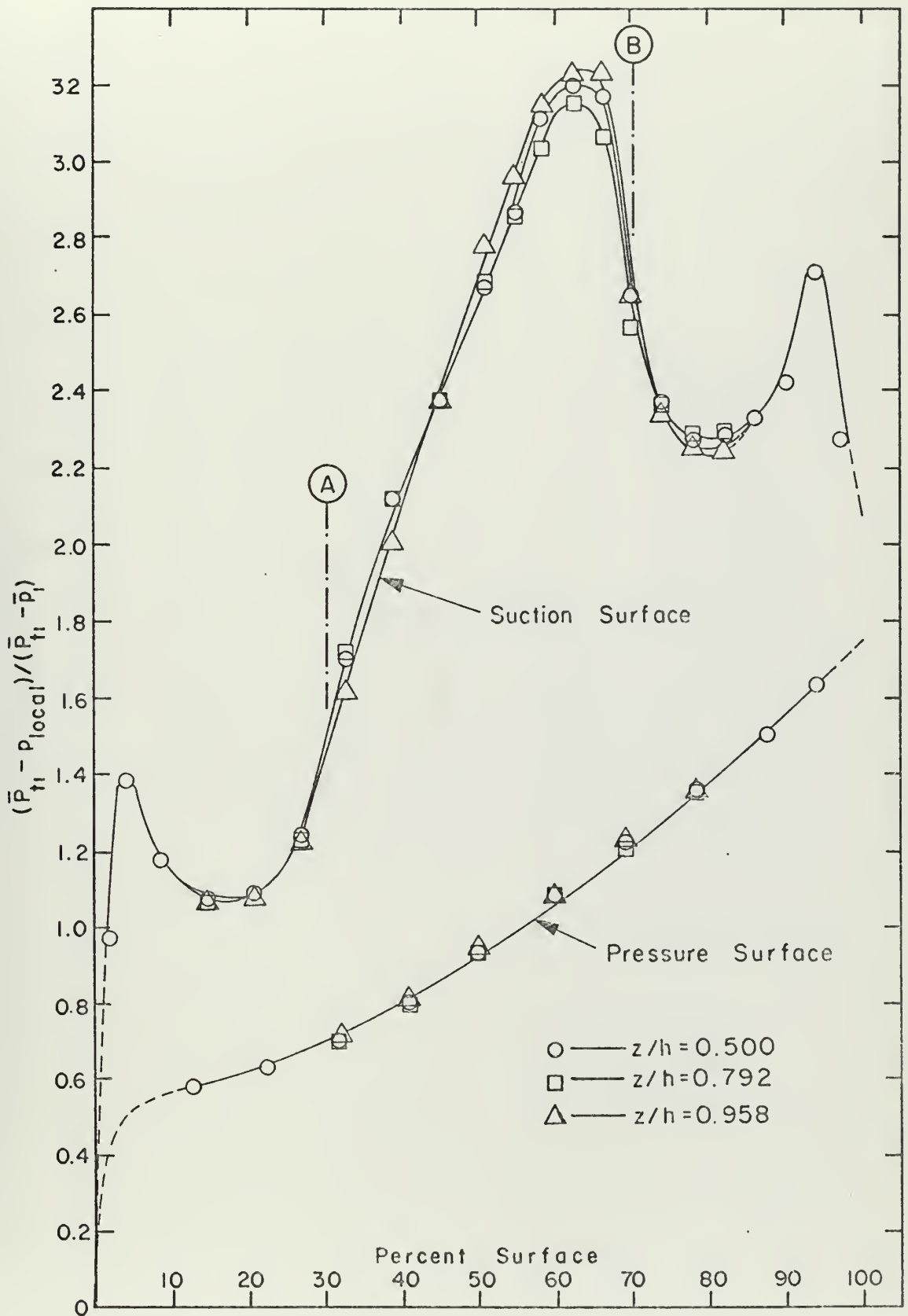


Figure 32. Static-Pressure Distributions on Blade Surface for  $h = 6.0$  inches ( $h/c = 0.888$ ).



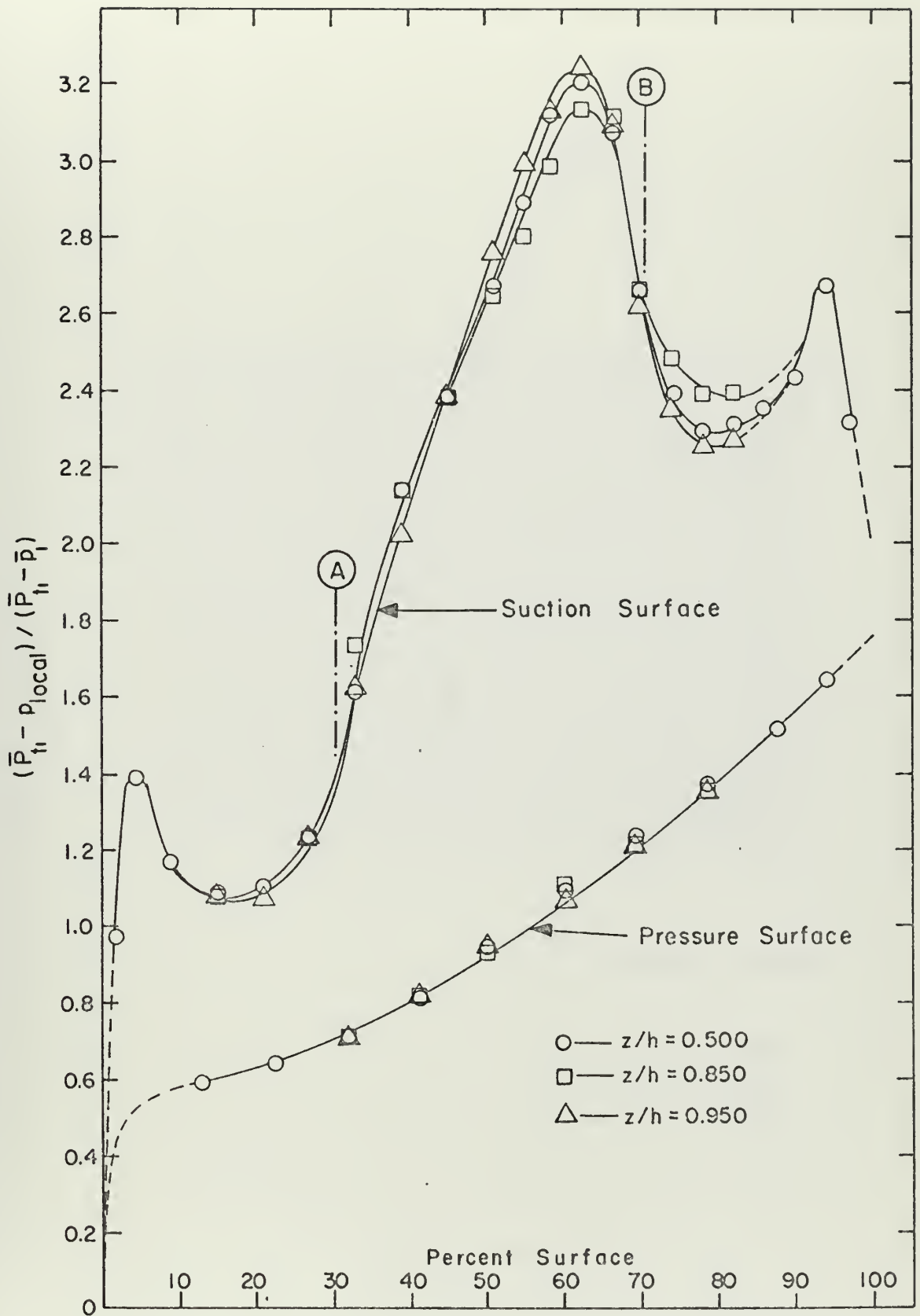


Figure 33. Static-Pressure Distributions on Blade Surface for  $h = 5.0$  inches ( $h/c = 0.740$ ).



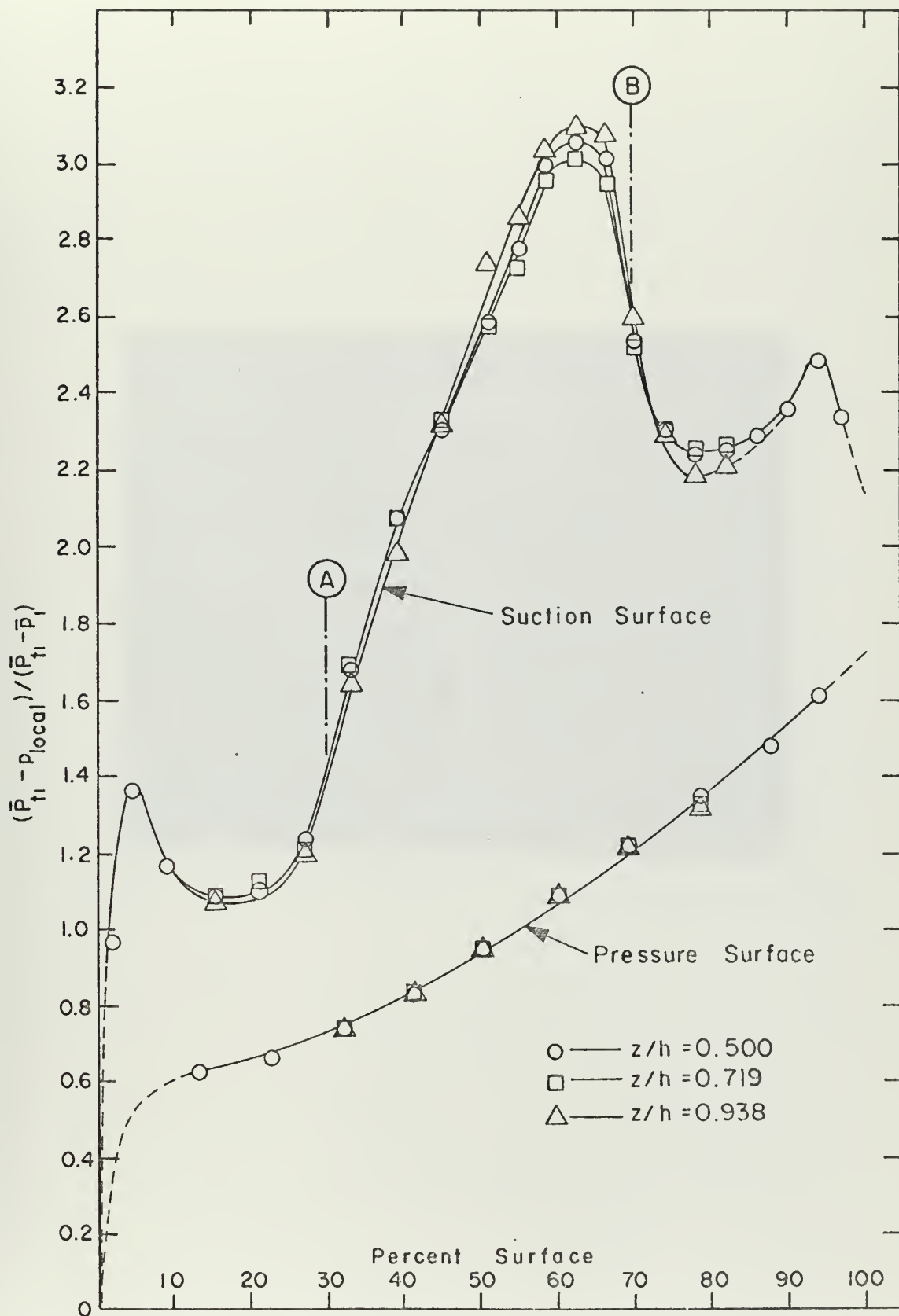


Figure 34. Static-Pressure Distributions on Blade Surface for  $h = 4.0$  inches ( $h/c = 0.592$ ).





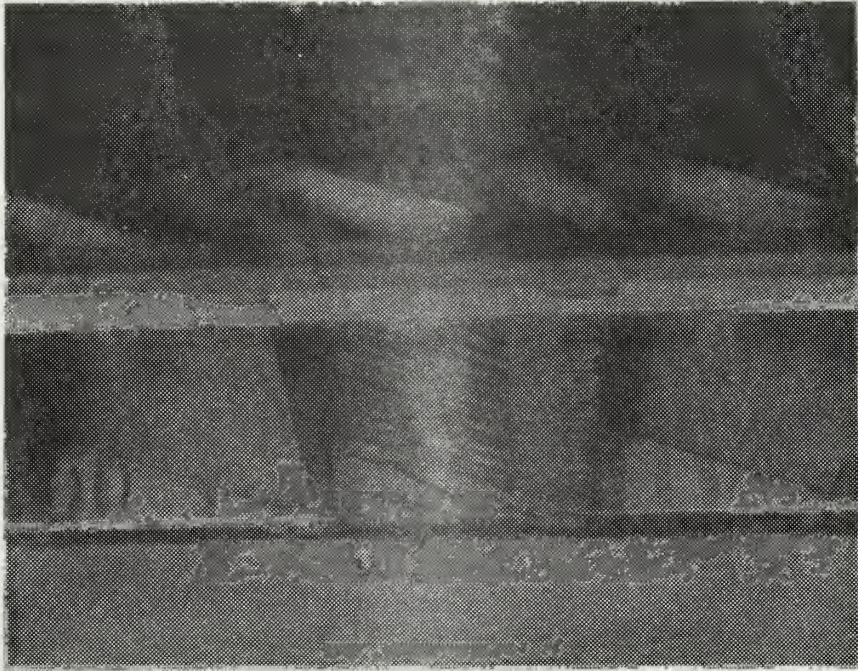


Figure 35. Tufts Attached to Blade Suction Surface.



and a small increase near the end wall. However, the secondary flow did not have a large effect on the suction-surface pressure distributions along the blade height.

The sudden increase in static pressure near point B indicated the possibility of flow separation in this region. As shown in Fig. 35, wool tufts attached to the suction surface displayed no evidence of backflow that could be caused by separation. Moreover, the lampblack pattern of Fig. 29 gave no indication of flow separation.

#### B. CHANNEL-FLOW-MODEL TESTS

The method used in the determination of kinetic-energy loss coefficients for the channel-flow-model tests is described in Appendix B. Curved sections with deflection angles of 90, 110, and 135 degrees and the corresponding straight sections were investigated. To verify the validity of the assumptions that were made to derive Eq. B8 for the overall loss coefficient, the flow at the exit of the 135-degree curved section was surveyed with a two-dimensional directional probe. The axial force calculated from the survey data was four percent higher than that measured with the force plate. Since the uncertainty in the dynamic pressure measured with the survey probe was about one percent, the agreement between the measured and calculated force was quite good.

The model tests were made for a range of pressure ratios  $P_{t1}/\bar{P}_2$  from 1.05 to 1.10. The maximum allowable force on the plate was exceeded at higher pressure ratios. The



results are shown in Fig. 36, where the parameter used for the abscissa is the ratio of the dimensionless axial force,  $\lambda = F/(P_{t1}A_2)$ , to  $\bar{\eta} = \bar{p}_2/P_{t1}$ . Figure 36 shows that the effect of compressibility on the loss coefficients was negligible for the range of pressure ratios that was used in these tests.

There was some scatter in the data, but average values of the kinetic-energy loss coefficients could be determined from Fig. 36. These average values are given in the following table.

KINETIC-ENERGY LOSS COEFFICIENTS

<u>Turning Angle</u>	<u><math>\bar{\zeta}_t</math></u>	<u><math>\bar{\zeta}_{2-d}</math></u>	<u><math>\bar{\zeta}_s</math></u>
90°	0.090	0.060	0.030
110°	0.120	0.080	0.040
135°	0.150	0.095	0.055

From the above table it can be seen that the total loss in kinetic energy  $\bar{\zeta}_t$  and the secondary loss  $\bar{\zeta}_s$  increased linearly with turning angle. Experience has shown, however, that overall kinetic-energy losses in high-deflection turbine cascades increase with the square of turning angle [Ref. 34]. The fundamental difference between the flow in a turbine cascade and the flow in a curved channel is that the former has a leading-edge stagnation point, which affects the boundary-layer flows over the blade surfaces. This difference could have caused the discrepancy in the loss coefficients measured in the channel model.





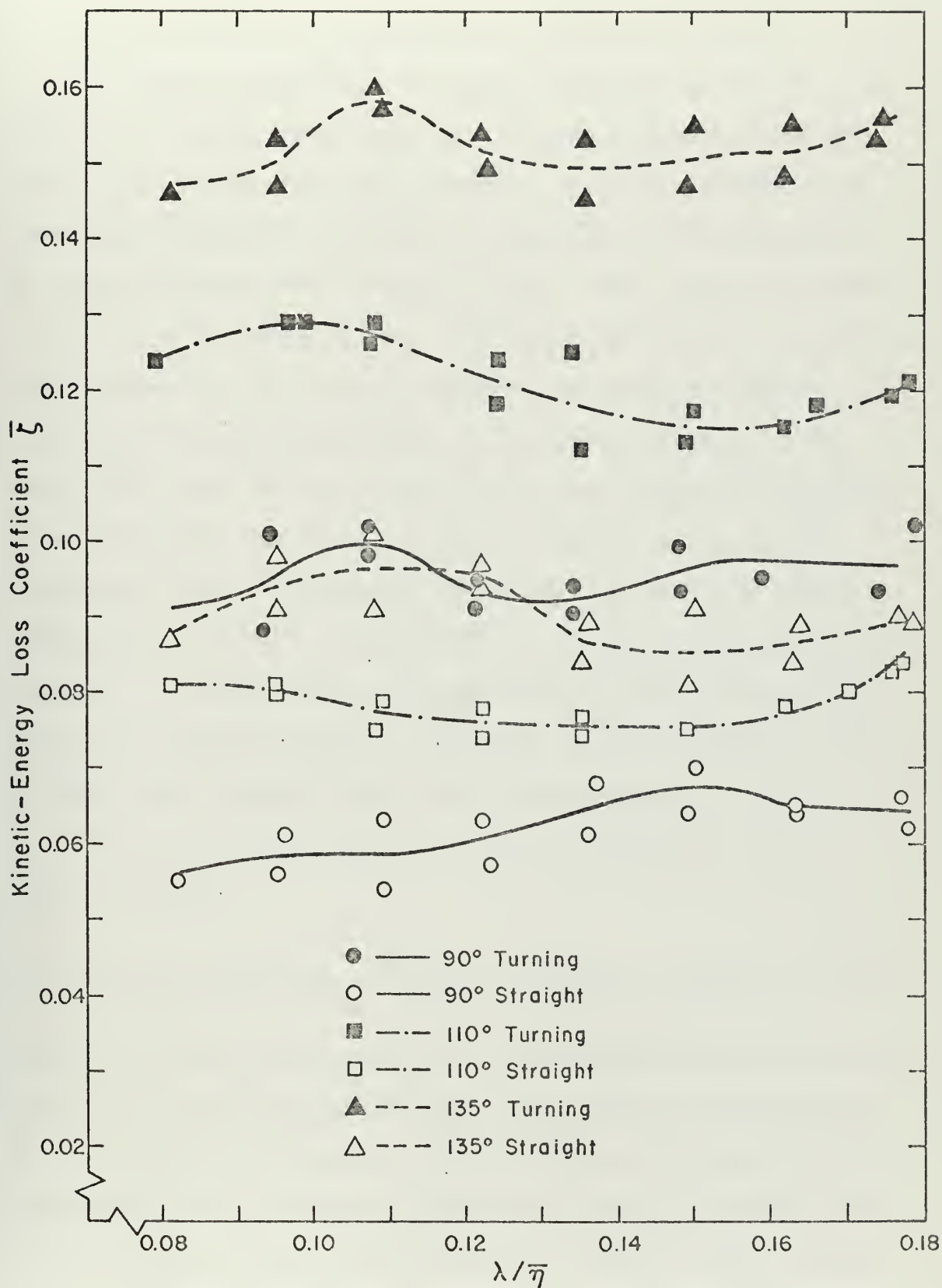


Figure 36. Kinetic-Energy Loss Coefficient  $\bar{\zeta}$  of Channel-Flow Model for Various Deflection Angles.





### C. CORRELATIONS FOR PREDICTION OF SECONDARY LOSSES

The design parameters of axial turbine stages are frequently established with approximate methods using the so-called one-dimensional analysis. In this approach the flow conditions at a reference diameter are considered to be representative of the whole stage. The reference diameter is usually taken as the arithmetic mean of the hub and tip diameters, and the flow properties ahead and after a row of blades are calculated at this mean diameter. The total flow loss for the blade row at the reference diameter consists of the two-dimensional or profile loss and the secondary loss. At present, empirical or semi-empirical relations are used to predict the loss due to secondary-flow effects. In this section the secondary-loss correlations that are commonly used are compared to the results of the cascade tests for the seven-inch blade height.

For the secondary loss in total pressure  $Y_s$ , Vavra [Ref. 34] gives

$$Y_s = 0.16 \frac{s}{h} \cos^2 \alpha_1 (\tan \alpha_1 - \tan \alpha_2)^2 \left[ 1 + \frac{1}{4} (\tan \alpha_1 + \tan \alpha_2)^2 \right]^{\frac{1}{2}} \quad (14)$$

where  $h$  is the blade height,  $s$  is the blade spacing, and  $\alpha_1$  and  $\alpha_2$  are the inlet and outlet flow angles, respectively, at the reference diameter. This relation is based on the replacement of the cascade blade by a vortex filament which has trailing vortices that produce an induced drag. With Eq. 14 the predicted secondary loss  $Y_s$  is 0.4396, whereas the measured value was 0.0601.



As a suggested improvement to the Ainley-Mathieson method of turbine performance prediction [Ref. 35], Dunham and Came [Ref. 36] give the relation,

$$Y_s = 0.1336 \frac{c}{h} \left( \frac{\cos \alpha_1}{\cos \beta_1} \right) \cos^2 \alpha_1 (\tan \alpha_1 - \tan \alpha_2)^2 \left[ 1 + \frac{1}{4} (\tan \alpha_1 + \tan \alpha_2)^2 \right]^{\frac{1}{2}} \quad (15)$$

where  $c$  is the blade chord and  $\beta_1$  is the inlet blade angle. Equation 15 is based on available cascade data on secondary losses [Ref. 37] and on a theoretical model similar to that used to develop Eq. 14. In Ref. 36 the secondary loss given by Eq. 15 is multiplied by the factor  $(R_e/2 \times 10^5)^{-0.2}$  to correct for the Reynolds number  $R_e$ . With Eq. 15 the predicted secondary loss  $Y_s$  is 0.3140, which is the same order of magnitude as the value given by Eq. 14.

For the secondary loss in kinetic energy  $\zeta_s$ , Markov [Ref. 38] suggests the correlation,

$$\zeta_s = (1 - \zeta_{2-d}) \zeta_e \frac{0}{h} \quad (16)$$

where  $0$  is the throat diameter of the blade passage. The end-wall loss  $\zeta_e$  is given by  $0.07 \leq \zeta_e \leq 0.18$ , and the higher values are recommended for impulse-type blading. Equation 16 is based on cascade tests of stator and rotor bladings. The two-dimensional loss in kinetic energy,  $\zeta_{2-d} = 0.040$ , was determined in the same manner as that described in Section IV.A for the two-dimensional loss  $Y_{2-d}$ . With Eq. 16 and  $\zeta_e = 0.17$ , the predicted secondary loss  $\zeta_s$  is 0.0275, whereas the measured value was 0.0274.



Soderberg's correlation for the secondary loss in kinetic energy [Ref. 39] is referred to the actual outlet kinetic energy and is denoted by  $\zeta'_s$ . This correlation is based on cascade data as well as actual turbine tests and is given by

$$\zeta'_s = \left( \frac{10^5}{R_h} \right)^{\frac{1}{4}} 0.075 \frac{b}{h} \quad (17)$$

where  $b$  is the axial width of the blade. The Reynolds number  $R_h$  is based on the exit velocity and the hydraulic mean diameter of the throat section  $d_h$ , which is given by

$$d_h = \frac{2hs \cos \alpha_2}{s \cos \alpha_2 + h}$$

From the definition of the kinetic-energy loss coefficient  $\zeta$ , Eq. A9, there is

$$\zeta_s = \frac{\zeta'_s}{1 + \zeta'_s} \quad (18)$$

With Eqs. 17 and 18, the predicted secondary loss  $\zeta_s$  is 0.0488, compared to the measured value of 0.0274.

Based on cascade tests of low-aspect-ratio compressor bladings, Griepentrog [Ref. 11] correlated secondary losses in total pressure with the parameters, aspect ratio  $h/c$  and design deflection angle  $\theta$ . The comparison of Griepentrog's correlation with the results of the present study is shown in Fig. 37.

Equations 14 and 15 predict unreasonably high secondary losses and thus are not suitable for application to impulse-type bladings where  $\alpha_1 \approx -\alpha_2$ . In low-aspect-ratio compressor



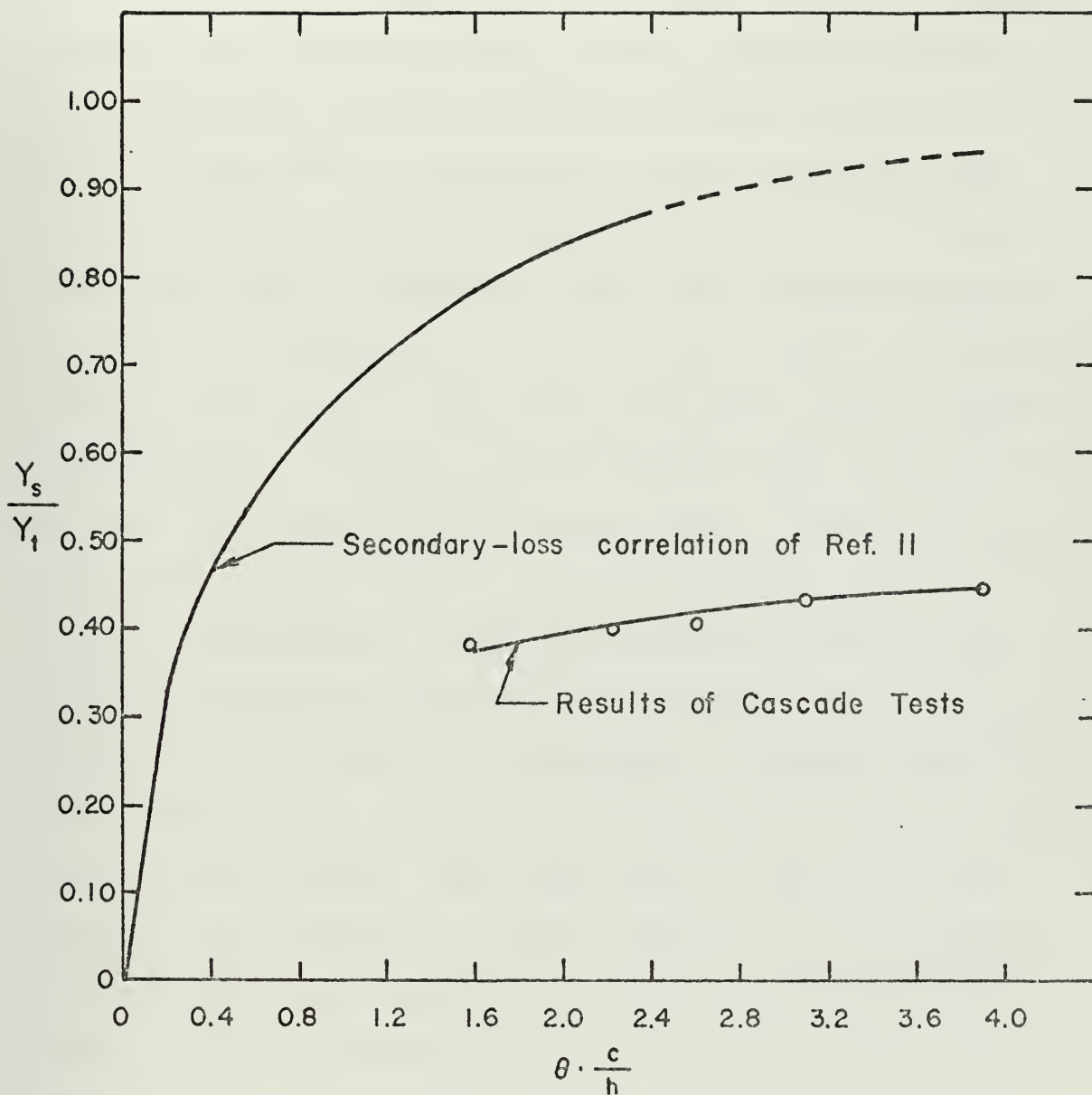


Figure 37. Comparison of Griepentrog's Secondary-Loss Correlation with Cascade Test Results.





cascades, the interaction of the corner vortices with the decelerating flow over the suction surface frequently causes flow separations. Therefore, correlations based on compressor cascade tests do not generally provide realistic estimates of the secondary losses in turbine cascades, as shown in Fig. 37. Soderberg's correlation gives a secondary loss that has the right order of magnitude but is about 78 percent higher than the measured loss. The agreement between the predicted secondary loss given by Eq. 16 and the measured value is excellent for the seven-inch blade height. However, the agreement was not as good at smaller blade heights. For the four-inch blade height, the measured secondary loss  $\zeta_s$  was 0.0308, whereas with Eq. 16 the predicted value is 0.0481. Nevertheless, Markov's correlation produced the most satisfactory comparisons with cascade test results. Markov [Ref. 38] based his correlation on cascade tests of rotor bladings that were quite similar to the blading used in the present study. Thus, empirical or semi-empirical secondary-loss prediction methods should only be applied to bladings that have characteristics similar to those used to establish the correlation.



## V. CONCLUSIONS

The conclusions obtained from this secondary-flow investigation, which are contained in the following section, were quantitative, qualitative, and general in nature.

### A. SECONDARY-FLOW LOSSES

From rectilinear cascade tests, overall flow losses were determined for a high-deflection turbine rotor blading at various blade heights. The losses due to secondary-flow effects were also determined. The blade aspect ratio  $h/c$ , which ranged from 1.480 to 0.592, was used as the parameter for discussing the test results. Since the blade chord and spacing were held constant, this choice was arbitrary. The smallest aspect ratio is typical of turbine bladings used in advanced, small gas-turbine power plants.

The total-pressure loss coefficient  $Y_2$  had an experimental uncertainty of about four percent and was considered to be less subject to experimental error than the kinetic-energy loss coefficient  $\zeta_2$ . As shown in Fig. 20, the secondary loss in total pressure increased with decreasing aspect ratio. Consequently, the overall total-pressure loss coefficient also increased as the aspect ratio was reduced. However, the magnitudes of the secondary loss and the overall loss for the smaller aspect ratios were not as large as expected. In particular, as the aspect ratio was decreased from 1.036



to 0.592, the increase in overall total-pressure loss coefficient was only 1.1 percent.

Comparisons of measured and predicted secondary loss coefficients showed that only Markov's correlation produced satisfactory agreement. Since Markov based Eq. 16 on cascade tests for rotor bladings of the type used in the present study, the application of empirical or semi-empirical secondary-loss relations is limited to bladings that have characteristics similar to those used to establish the experimental correlation. Completely general correlations for secondary-loss predictions are extremely difficult to obtain by systematic cascade testing due to the many independent variables that can affect secondary losses. For example, a thicker end-wall boundary layer at the cascade inlet causes higher secondary losses, as shown in Fig. 7. Moreover, the channel-flow-model tests showed that secondary losses increase with deflection angle. However, a discrepancy between the results of these tests and experience in turbine cascades exists for the functional relationship of the increase in losses with turning angle. Such differences can occur when oversimplified models of the actual flow in turbomachines are used.

## B. SECONDARY-FLOW DESCRIPTION

The qualitative results of this investigation helped to clarify the physical description of the complex secondary-flow phenomena. The lampblack flow-visualization technique reproduces the mechanisms of the flow only in boundary-layer



regions and cannot supply any direct information on processes in the main part of the flow. However, comparison of the contour plots of Figs. 21 through 24 with the lampblack flow patterns of Figs. 25 through 29 clearly showed the effects of the secondary flows in the cascade.

To satisfy the equilibrium condition given by Eq. 2 of Section II.B.1, end-wall boundary-layer fluid flows from the pressure side of the blade passage to the suction side. There was no evidence of flow from the blade pressure-surface boundary layer into the end-wall region. The cascade secondary flow started to form at point A of Fig. 30. At a point slightly further downstream, the corner secondary flow started to form due to the interaction of the end-wall boundary-layer fluid flowing into the corner region with the blade suction-surface boundary layer. This interaction is evident in Figs. 28 and 29, which show the cross-flows in the suction-surface boundary-layer region near the end wall. These cross-flows also swept some of the boundary-layer fluid off the suction surface, producing lower losses near the end wall, as shown by the loss distributions of Figs. 14 through 17. Thus, the cores of fluid with low total pressure, that are shown in the contour plots, consisted of material that originated in the end-wall and suction-surface boundary layers. Moreover, due to the extensive cross-flows caused by the large deflection angle of the cascade, these low-total-pressure cores were located at a distance of about 20 percent of the blade height from the end wall.





### C. GENERAL

The maximum total-pressure loss coefficient along the blade height in Figs. 14 through 17 was caused by the so-called corner vortices. This loss was considerably larger than that caused by the so-called cascade secondary vortices, as shown by the smaller peak in the spanwise loss-distribution plots. Thus, the predominate effects of secondary flows in high-deflection turbine cascades are viscous in nature, namely the flow interactions near the end-wall and suction-surface corner region.

Theories based on assumed inviscid flow through the cascade can only account for the cascade secondary flow, and the associated streamwise or secondary vorticity is distributed uniformly across the blade passage. However, the present investigation has shown that the cascade secondary vortices are not responsible for the large secondary losses, and that the secondary-flow effects are concentrated near the suction-surface and end-wall corner region. Hence, the applicability of the inviscid approach to high-deflection turbine cascades is highly questionable.

Furthermore, in analytical solutions of three-dimensional end-wall boundary layers, cross-flow effects must be limited to the end-wall boundary-layer region. However, Fig. 29 shows that cross-flows continue far outside the end-wall boundary layer. Moreover, the important interactions of the end-wall and suction surface boundary layers cannot be treated with the available boundary-layer calculation methods.



The secondary-flow effects on the blade-surface static-pressure distributions were small, as shown in Figs. 31 through 34. Therefore, these pressure distributions were primarily determined by the main through-flow, while the secondary-flow processes were mostly concentrated near the blade suction surface. However, the contour plots show that the secondary flow influences the flow in the blade passage as well as the flow in the suction-surface boundary layer. Hence, the secondary flow is not entirely a boundary-layer phenomenon in turbine cascades with large deflection angles and small aspect ratios.

Due to the complex three-dimensional flow phenomena that are involved, quantitative secondary-flow investigations must be experimental at present. This investigation was carried out in the Rectilinear Cascade Test Rig because of the extreme difficulties associated with measuring fluid properties in the rotating bladings of small turbines. Thus, the important tip-clearance and rotational effects could not be simulated in the cascade. These effects will certainly increase the overall flow losses in the actual machine. For example, the tip-clearance flow and scraping effect described in Section II.B could cause flow separation on the suction surface in the region of point B where a steep adverse pressure gradient exists, as shown in Figs. 31 through 34. Nevertheless, this study without tip-clearance and rotational effects has shown that the increase in overall total-pressure loss caused by decreasing blade height was small.



## APPENDIX A

### REDUCTION OF CASCADE TEST DATA

#### 1. Thermodynamic Relations

The following derivations are based on the assumption that the fluid flowing through the cascade is a perfect gas or that it satisfies

$$p/\rho = gR_g T \quad (A1)$$

where  $p$ ,  $\rho$ , and  $T$  are the static pressure, density, and temperature respectively,  $g$  is the gravitational constant, and  $R_g$  is the gas constant. For a constant specific heat ratio  $\gamma$ , there is

$$c_p = \frac{\gamma}{\gamma - 1} \cdot \frac{R_g}{J} \quad (A2)$$

where  $J$  is the mechanical equivalent of heat.

The relation between the static pressure and density for an isentropic process of a perfect gas is

$$p\rho^{-\gamma} = C \quad (A3)$$

With Eq. A1 the relation given by Eq. A3 can be rewritten with the static temperature  $T$  of the fluid, or

$$pT^{\gamma/(\gamma-1)} = K \quad (A4)$$

The quantities  $C$  and  $K$  in Eqs. A3 and A4 are constants at fixed values of the entropy  $s$ .



The flow through the cascade was assumed to be steady and adiabatic. The flow process is shown on the entropy diagram of Fig. A1. The subscripts 1 and 2 refer to the upstream and downstream measuring planes which correspond to stations (1) and (2) of Fig. A2. The plenum temperature  $T_{p1}$  was taken as the constant total temperature, since the velocity was negligible in this region. Thus, the velocity at a measuring plane is

$$T_t = T_{p1} = T + \frac{v^2}{2gJc_p}$$

Equations A1, A3, and A4 are also valid for stagnation conditions. Hence, the velocity in terms of the total pressure  $P_t$  and the static pressure  $p$  is

$$v^2 = \frac{2}{\gamma - 1} \gamma g R_g T_{p1} \left[ 1 - \left( \frac{p}{P_t} \right)^{(\gamma-1)/\gamma} \right] \quad (A5)$$

where Eq. A2 has been substituted for  $c_p$ . The dynamic pressure  $q$ , which is the difference between the total and static pressures, was a measured quantity and not the static pressure. With this substitution the velocity becomes

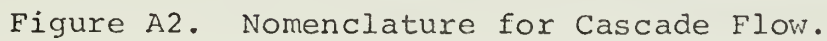
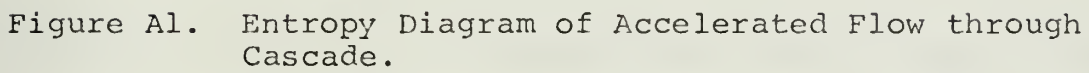
$$v^2 = \frac{2}{\gamma - 1} \gamma g R_g T_{p1} \left[ 1 - \left( 1 - \frac{q}{P_t} \right)^{(\gamma-1)/\gamma} \right] \quad (A6)$$

From Eqs. A1 and A3, the density at a measuring plane is

$$\rho = \frac{P_t}{g R_g T_{p1}} \left( 1 - \frac{q}{P_t} \right)^{1/\gamma} \quad (A7)$$









## 2. Loss Coefficients

Two loss coefficients were used in the analysis of the cascade data; the total-pressure loss coefficient  $Y_2$ , which is defined as

$$Y_2 = \frac{\bar{p}_{t1} - \bar{p}_{t2}}{\bar{p}_{t1} - \bar{p}_1} \quad (A8)$$

and the kinetic-energy loss coefficient  $\zeta_2$ , which is defined as

$$\zeta_2 = 1 - \left( \frac{\bar{v}_2}{\bar{v}_{2th}} \right)^2 \quad (A9)$$

As shown in Fig. A1, the theoretical velocity  $v_{2th}$  is the velocity that would obtain if the expansion between the cascade inlet and outlet were isentropic. Equation A9 can be rewritten in terms of pressure. With Eq. A5

$$\zeta_2 = 1 - \frac{\left[ 1 - \left( \frac{\bar{p}_2}{\bar{p}_{t2}} \right)^{(\gamma-1)/\gamma} \right]}{\left[ 1 - \left( \frac{\bar{p}_2}{\bar{p}_{t1}} \right)^{(\gamma-1)/\gamma} \right]} \quad (A10)$$

The overscores in Eqs. A8, A9, and A10 denote mass-averaged quantities. The fluid properties were measured at the cascade inlet and outlet at stations (1) and (2) in corresponding planes of constant  $z$ . These quantities were functions of the traversing direction  $x$ . Local loss coefficients can only be determined along a streamline, which was impractical for the present investigation since



the flow was three-dimensional. For this reason mass-averaged flow conditions at the cascade inlet and outlet were compared for the calculation of the spanwise variation of the loss coefficients  $Y_2$  and  $\zeta_2$ .

The mass average of a quantity  $Q$  is obtained by integrating that quantity, weighted by the mass flux per unit span, over the distance traversed and then dividing by the total mass flux per unit span. The mass-averaged quantity  $\bar{Q}$  is then

$$\bar{Q} = \frac{\int \rho V_a Q dx}{\int \rho V_a dx}$$

where  $Q$  denotes a fluid property and  $V_a$  is the axial component of the velocity vector  $\vec{V}$ .

The total loss coefficients were determined by integrating the loss coefficients obtained at each spanwise position with Eqs. A8 and A10 along the relative blade height  $z/h$ ; therefore,

$$Y_{2t} = 2 \int_{0.5}^{1.0} Y_2 d\left(\frac{z}{h}\right) \quad (A11)$$

and

$$\zeta_{2t} = 2 \int_{0.5}^{1.0} \zeta_2 d\left(\frac{z}{h}\right) \quad (A12)$$

where the integrals were taken over half the blade height since it was verified that the loss distribution was symmetrical.



In addition to the loss relations described above, the cascade inlet flow conditions were compared to those conditions far downstream of the cascade, station (3) in Fig. A2, where the flow was considered to be uniform. The equalizing of the flow between stations (2) and (3), due to viscous effects and turbulent mixing, is associated with an additional loss, the so-called mixing loss. These loss coefficients are given by Eqs. A8, A10, A11, and A12 with the subscript 3 replacing the subscript 2 in each equation.

### 3. Conditions Far Downstream

The flow conditions far downstream of the cascade were calculated by applying the momentum theorem to the flow between the cascade exit, station (2), and the uniform flow at station (3). The control region used was bounded by two streamlines separated by a distance equal to the blade spacing  $s$  extending from station (2) to station (3), as shown in Fig. A2.

Although the flow at the exit of the cascade was three-dimensional, it was assumed that the planes with the distance  $\Delta z/2$  above and below the plane of Fig. A2 could be considered as stream surfaces for the purpose of establishing the conditions far downstream. For this case the momentum equation could be written per unit span. In addition, the shear stress integral at station (2) was neglected, since simple methods do not exist to determine the value of the shear stresses by tests [Ref. 12]. The weight of the fluid in the





control region was also neglected. With these simplifications the momentum equation, Eq. 5(18) in Ref. 12, becomes

$$\int_0^s d\dot{m}_2 \vec{V}_2 - \dot{m} \vec{V}_3 + \vec{j} \int_0^s p_2 dx - \vec{j} p_3 s = 0 \quad (A13)$$

The velocity vectors  $\vec{V}_2$  and  $\vec{V}_3$  are

$$\vec{V}_2 = \vec{i} V_2 \cos\theta_2 \sin\alpha_2 + \vec{j} V_2 \cos\theta_2 \cos\alpha_2 + \vec{k} V_2 \sin\theta_2$$

$$\vec{V}_3 = \vec{i} V_3 \sin\alpha_3 + \vec{j} V_3 \cos\alpha_3$$

where the flow angles have to be introduced with their proper algebraic signs. The mass flow rate per unit span is

$$\dot{m} = \int_0^s \rho_2 V_2 \cos\theta_2 \cos\alpha_2 dx = \rho_3 V_3 \cos\alpha_3 s \quad (A14)$$

The above relations substituted into Eq. A13 give

$$\begin{aligned} \int_0^s d\dot{m}_2 (\vec{i} V_{t2} + \vec{j} V_{a2} + \vec{k} V_2 \sin\theta_2) \\ - \dot{m} (\vec{i} V_3 \sin\alpha_3 + \vec{j} V_3 \cos\alpha_3) + \vec{j} \int_0^s p_2 dx - \vec{j} p_3 s = 0 \end{aligned} \quad (A15)$$

where  $V_{t2} = V_2 \cos\theta_2 \sin\alpha_2$  and  $V_{a2} = V_2 \cos\theta_2 \cos\alpha_2$ . The component of Eq. A15 in the direction of the unit vector  $\vec{i}$  gives

$$V_3 \sin\alpha_3 = \frac{\int_0^s \rho_2 V_{a2} V_{t2} dx}{\int_0^s \rho_2 V_{a2} dx} \quad (A16)$$

From Eq. A14

$$V_3 \cos\alpha_3 = \frac{1}{\rho_3 s} \int_0^s \rho_2 V_{a2} dx \quad (A17)$$



With the substitution of Eq. A17, the component of Eq. A15 in the direction of the unit vector  $\vec{j}$  gives

$$p_3 = \frac{1}{s} \int_0^s \rho_2 v_{a2}^2 dx - \frac{1}{\rho_3 s^2} \left( \int_0^s \rho_2 v_{a2} dx \right)^2 + \frac{1}{s} \int_0^s p_2 dx \quad (A18)$$

Equations A16 and A17 can be combined to obtain

$$v_3^2 = \frac{\left( \int_0^s \rho_2 v_{a2} v_{t2} dx \right)^2}{\left( \int_0^s \rho_2 v_{a2} dx \right)^2} + \frac{1}{(\rho_3 s)^2} \left( \int_0^s \rho_2 v_{a2} dx \right)^2 \quad (A19)$$

In order to calculate the static pressure and velocity at station (3) with Eqs. A18 and A19, the density  $\rho_3$  must be known. Inverting Eq. A5 gives

$$\frac{p_3}{p_{t3}} = \left( 1 - \frac{\gamma - 1}{2} \frac{v_3^2}{\gamma g R_g T_{p1}} \right)^{\gamma/(\gamma-1)} \quad (A20)$$

Equation A7 can also be expressed as

$$\rho_3 = \left( \frac{p_3}{p_{t3}} \right)^{(1-\gamma)/\gamma} \frac{p_3}{g R_g T_{p1}} \quad (A21)$$

The flow conditions far downstream at each spanwise position were established by using successive approximations to the density  $\rho_3$  [Ref. 29]. Equations A18 and A19 were solved using the measured data at station (2) and a trial value for  $\rho_3$ , say  $\rho_3 = \rho_2$ . Equations A20 and A21 were then used to obtain a new value for  $\rho_3$ . The process was repeated until two successive values of  $\rho_3$  differed in absolute value by a small tolerance. Since the equalizing of the flow between



stations (2) and (3) takes place at about the same pressures and temperatures, the convergence was rapid.

#### 4. Computer Program CASCADE II

The cascade test data were reduced on the IBM 360/67 computer system of the Naval Postgraduate School by means of the FORTRAN IV program CASCADE II, which is listed after the appendixes. The program is self-explanatory since comment statements were extensively used throughout; however, some general comments about the program are necessary.

A data run consisted of a cascade traverse, inlet and outlet, at a fixed spanwise position. The number of data points in each run depended on the distance being traversed and the traversing interval. A paper tape containing all the information for a data run was generated by the automatic data-logging system described in Section III.A. Data cards, one for each data point, were punched directly by the computer using its online-data-acquisition capability [Ref. 31]. Scale factors were required in the format statements for reading input data to properly place the decimal point.

Since equal traversing intervals were utilized in the x-direction of Fig. A2, Simpson's rule was used in obtaining approximate integrals over the blade spacing. This was accomplished by subroutine SIMP in the computer program. For approximate integration in the z-direction where the experimental data were nonequally spaced, a rule based on overlapping parabolas was employed [Ref. 40]. This rule combines both an integrating and a smoothing feature, and



the numerical integration is carried out by function ZINT in CASCADE II. The roundoff error in both integration rules was decreased by performing the arithmetic operations of the two subprograms in double precision.

The contour plots of relative total pressure at the cascade exit were obtained from subroutine CONTUR and the offline plotter facility of the computer center. Subroutine CONTUR is in the computer-system source library, but it has not been precompiled and must be accessed by concatenation in the FORTRAN compile step.





## APPENDIX B

### REDUCTION OF CHANNEL-FLOW-MODEL TEST DATA

The channel-flow model is shown schematically in Fig. B1. The following assumptions are made:

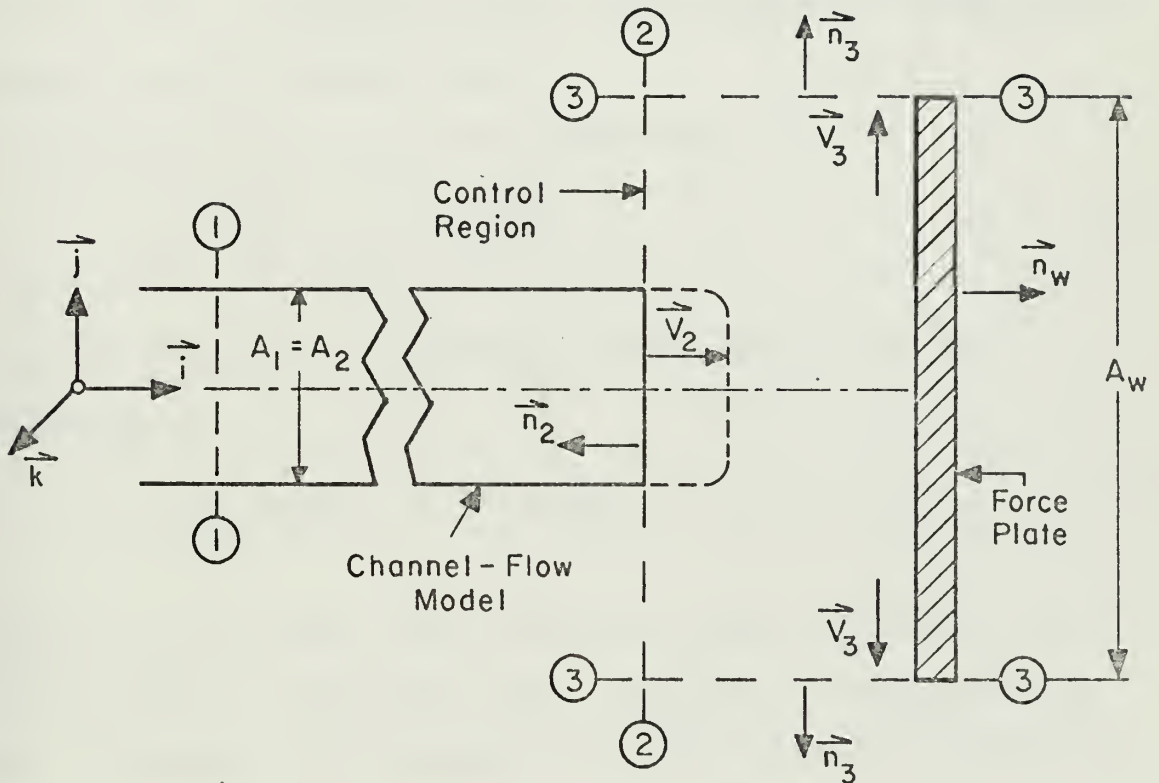


Figure B1. Schematic Side View of Channel-Flow Model.

- (a) steady, adiabatic flow of a perfect gas,
- (b) negligible fluid weight in the control region,
- (c)  $\vec{V}_2 = \vec{i} V_2$ ,
- (d)  $\vec{V}_3 = \vec{j} V_{3y} + \vec{k} V_{3z}$ ,
- (e) neglect shear stresses at stations 2 and 3.



With these assumptions the momentum theorem applied between stations 2 and 3 gives

$$\begin{aligned} \int_{(A_3)} \dot{m}_3 (\vec{j}v_{3y} + \vec{k}v_{3z}) - \vec{i} \int_{(A_2)} v_2 \dot{m}_2 = \\ \vec{i} \int_{(A_2)} p_2 dS_2 + \vec{i} p_a A_a - \vec{n}_3 \int_{(A_3)} p_3 dS_3 - \vec{i} \int_{(A_w)} p_w dS_w \quad (B1) \end{aligned}$$

where  $p_a$  is ambient pressure and  $A_a = A_w - A_1$ . The subscripts 2 and 3 refer to stations where fluid enters and leaves the control region, respectively.

The mass flow rate at the model exit is

$$\int_{(A_2)} \dot{m}_2 = \int_{(A_2)} \rho_2 v_2 dS_2 \quad (B2)$$

The last integral on the right side of Eq. B1 can be expressed by

$$\vec{i} \int_{(A_w)} p_w dS_w = \vec{i} (F + p_a A_w) \quad (B3)$$

where  $F$  is the axial force exerted by the flow on the flat plate normal to the model exit. With the substitutions of Eqs. B2 and B3, the component of Eq. B1 in the direction of the unit vector  $\vec{i}$  gives

$$F = \int_{(A_2)} (\rho_2 v_2^2 + p_2) dS_2 - p_a A_2 \quad (B4)$$

Equation B4 can be expressed in terms of the loss in kinetic energy through the channel-flow model, that is, between stations 1 and 2 of Fig. B1. As verified by tests, uniform flow conditions existed at the inlet to the model.



The flow process through the model is similar to that shown on the entropy diagram of Fig. A1. With Eqs. A5 and A7 and the definition of the kinetic-energy loss coefficient given by Eq. A9, it can be shown that

$$V_2^2 = \frac{2\gamma}{\gamma-1} gR_g T_{t1} \left[ (1-\zeta) \left( 1 - \eta^{(\gamma-1)/\gamma} \right) \right] \quad (B5)$$

and

$$\rho_2 = \left( \frac{P_{t1}}{gR_g T_{t1}} \right) \frac{\eta}{1 - \left[ (1-\zeta) \left( 1 - \eta^{(\gamma-1)/\gamma} \right) \right]} \quad (B6)$$

where  $\eta = p_2/P_{t1}$ .

The objective of the channel-flow model tests was to establish the overall kinetic-energy loss coefficient  $\bar{\zeta}$  for various deflection angles. For this purpose it was sufficient to measure an average static pressure  $\bar{p}_2$  at the model exit. Thus,  $\bar{\zeta}$  and  $\bar{\eta} = \bar{p}_2/P_{t1}$  are constant. With the substitutions of Eqs. B5 and B6, Eq. B4 can be integrated to obtain

$$\frac{F}{P_{t1} A_2} = \frac{\frac{2\gamma}{\gamma-1} \bar{\eta} (1-\bar{\zeta}) \left( 1 - \bar{\eta}^{(\gamma-1)/\gamma} \right)}{1 - \left[ (1-\bar{\zeta}) \left( 1 - \bar{\eta}^{(\gamma-1)/\gamma} \right) \right]} + \bar{\eta} - \frac{P_a}{P_{t1}} \quad (B7)$$

Equation B7 can be solved for the loss coefficient  $\bar{\zeta}$ , which gives

$$\bar{\zeta} = 1 - \frac{\left( 1 - \frac{\epsilon}{\lambda} \right)}{\left( 1 - \bar{\eta}^{(\gamma-1)/\gamma} \right) \left( 1 + \frac{2\gamma}{\gamma-1} \frac{\bar{\eta}}{\lambda} - \frac{\epsilon}{\lambda} \right)} \quad (B8)$$

where  $\lambda = F/(P_{t1} A_2)$  and  $\epsilon = \bar{\eta} - (P_a/P_{t1})$ .



Equation B8 was used to determine the overall loss for the curved sections of the model and the two-dimensional loss for the straight sections, the difference between the two being the additional secondary loss.





## APPENDIX C

### MEASUREMENT OF OUTLET THROUGH-FLOW ANGLE

The outlet flow was surveyed with the three-dimensional directional probe described in Section III.A. In uniform or nearly uniform flow, this survey probe accurately indicates the through-flow angle when the pressures sensed by the two side holes are balanced. For the cascade tests the probe was mounted so that its axis was perpendicular to the total-pressure gradient in the blade wake region. Thus, the side sensing holes, which are separated by a certain distance, were located in regions of different total pressure; and the probe rotated out of the through-flow direction in order to balance the two side pressures. This resulted in physically smaller wakes and, therefore, lower indicated loss in total pressure, as shown by preliminary test results.

When the side pressures were allowed to balance, errors in the indicated outlet through-flow angle as large as ten degrees occurred in the wake region, as shown in Fig. C1. The exit through-flow angle was also measured with a much smaller, wedge-shaped probe without a center sensing hole, and the results are depicted in Fig. C1. Less error in the angle measurement was experienced with the smaller probe, but through-flow angle is the only flow property measured by this probe. The outlet flow was then surveyed with the



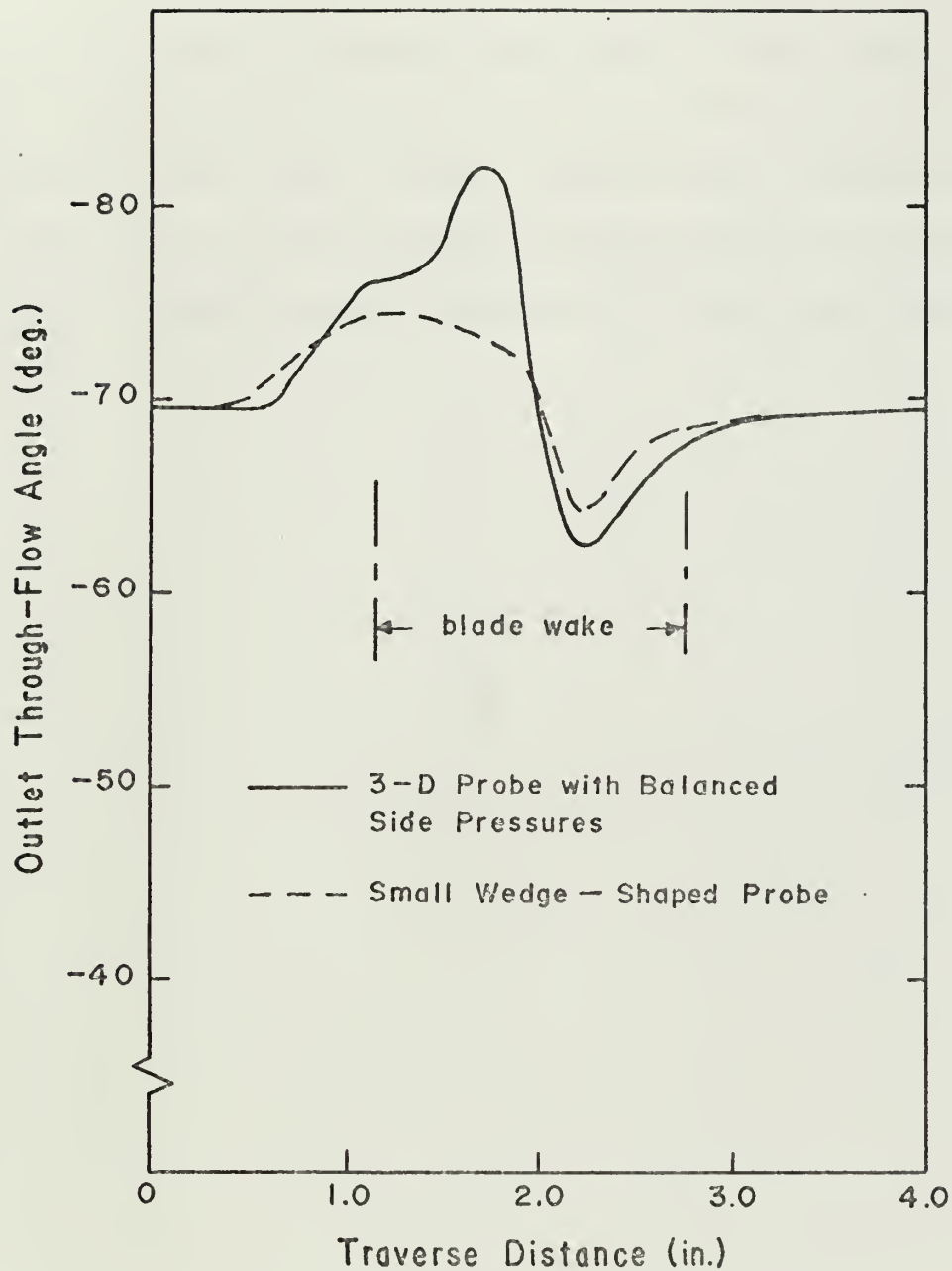


Figure C1. Error in Measurement of Outlet Through-Flow Angle in Blade Wake Region.



three-dimensional probe using the exit through-flow angle as determined with the small, wedge-shaped probe. An additional test was made using a constant outlet through-flow angle through the wake region equal to that angle measured outside of the wake, which was essentially uniform. Comparisons showed that using a constant exit through-flow angle gave the most satisfactory results since more accurate outlet total pressures were obtained with this surveying technique.



```

00000010
00000020
00000030
00000040
00000050
00000060
00000070
00000080
00000090
00000100
00000110
00000120
00000130
00000140
00000150
00000160
00000170
00000180
00000190
00000200
00000210
00000220
00000230
00000240
00000250
00000260
00000270
00000280
00000290
00000300
00000310
00000320
00000330
00000340
00000350
00000360
00000370
00000380
00000390
00000400
00000410
00000420
00000430
00000440
00000450
00000460
00000470
00000480

COMPUTER PROGRAM CASCADE II

PROGRAM CASCADE II FOR THE REDUCTION OF CASCADE DATA FROM THE
INVESTIGATION OF SECONDARY LOSSES. THE SPANWISE VARIATION IN LOSS
COEFFICIENT IS DETERMINED AS WELL AS THE OVERALL LOSS COEFFICIENT.

      IMPLICIT REAL*8 (F)
      DIMENSION TPL(45),ALFA1(45),ALFA2(45),PT1(45),DPI(45),THETA2(45),
1    PT2(45),DP2(45),X1(45),X2(45),V1(45),V2(45),VA1(45),VA2(45),
2    VT2(45),RHO1(45),RHO2(45),F11(45),F12(45),F13(45),F14(45),F15(45),
3    F16(45),F21(45),F22(45),F23(45),F24(45),F25(45),F26(45),F27(45),
4    F28(45),FZETA2(20),FY2(20),FY2L(45),Y2LOC(41,20),FZETA3(20),FY3(20)
5    )
      REAL*8 ZINT,BH(20),PHLO,BHUP,TITLE1(12)/'CONTOURS','OF LOCAL','
      LOSS COEFFICIENT','AT','CASCADE','EXIT FO','R ASPECT','
      2ATIO=','C.740','J.','R. WOODS.'/
      REAL*4 G/32.174/,RG/53.3448/,EPS/O.1E-6/,CL(15)/1.5,1.4,1.3,1.2,1.
1    1,1.9,8,7,6,5,4,3,2,1/
      LOGICAL*1 LTG(3)/.FALSE.,.FALSE./

      READ CASCADE CONFIGURATION (BLADE HEIGHT, CHORD, AND SPACING) AND
      NUMBER OF SETS OF DATA (NSETS).

      IO FORMAT (5,10) H,C,S,NSETS
      IO FORMAT (3F6.3,I4)

      WRITE OUTPUT HEADINGS.

      AR = H/C
      SIGMA = C/S
      HSR = H/S

      WRITE (6,20) AR,SIGMA,HSR
      IO FORMAT (1H1//52X,'TURBO-PROPULSION LABORATORY','50X','U.S. NAVAL PGS
1    ITGRADUATE SCHOOL'//12X,'CASCADE TESTS--A SPECT RATIO (H/C) =',F6.
2    23,'* SOLIDITY (C/S) =',F6.3,'* HEIGHT TO SPACING RATIO (H/S) =',F6.
3    3F6.3//8X,'RELATIVE ***MASS-AVERAGED FLOW CONDITIONS AT CASO00G370
4    CASCADE INLET (1) AND CUTLET (2)***',7X,'LOSS',7X,'MASS RATIO',/200000380
5    5X,'RUN BLADE',6X,'PT1',6X,'PI',7X,'V1',6X,'M1 ALPHA1 PT2',000000390
6    66X,'P2',7X,'V2',6X,'M2 ALPHA2 COEFFICIENTS FLOW (PPL'/12X,(P
7    7'NO. HEIGHT(Z/H) (PSFA) (PSFA) (DEG) (DEG) (PSFA) (P
8    8SFA) (FT/SEC)',9X,'(DEG) (ZETA2) RATIO (PATM)')
      K IS USED AS A COUNTER FROM ONE TO NSETS.

      DO 110 K=1,NSETS

      READ ATMOSPHERIC TEMPERATURE AND PRESSURE, RUN NUMBER (NRUN), NUMBER

```





```

C OF DATA POINTS (NPTS), AND SPANWISE TRAVERSE POSITION (Z).
C
  READ (5,30) TATM,PATM,NRUN,NPTS,Z
  30 FORMAT (F5.1,F6.2,2I4,F6.3)
C
C READ INPUT DATA.
C
  READ (5,40) (TPL(I),ALFA1(I),ALFA2(I),PT1(I),DPL(I),THETA2(I),PT2
1(I),DP2(I),PPL(I),X1(I),X2(I),I=1,NPTS)
  40 FORMAT (3F6.2,3P5F6.0,2P5F6.0,DP2F3.2)
C
C CONVERT PATM(IN.HG.) TO PSIA.
C
  SGHG = 13.63905 - (1.36303E-3*TATM)
  CFHG = (.4891585*SGHG)/13.54
  PATM = PATM*CFHG
  FGAMMA = 0.00
  FTPLM = 0.00
  FPPLM = 0.00
C
C CORRECT INPUT DYNAMIC PRESSURES WITH PROBE CALIBRATION DATA. DIFFERENT
C PROBES REQUIRE DIFFERENT CALIBRATION CONSTANTS HERE. 5-HOLE PROBE
C CALIBRATION IS FOR PITCH ANGLES BETWEEN -30 AND +10 ONLY.
C
  DO 50 J=1,NPTS
    DP1(J) = DPL(J)/(1. - .0492)
    DPL(J) = (DPL(J)/DP1(J) - .045)*144.
    Y = THETA2(J)/DP2(J)
    THETA2(J) = (48.3075*Y) + 1.00522
    W = 1.12128 - (1.71087E-3*THETA2(J)) + (1.32222E-4*(THETA2(J)**2))
    1 + (2.07438E-6*(THETA2(J)**3))
    DP2(J) = W*DP1(J)*144.
C
C CONVERT INPUT PLENUM PRESSURES TO PSIA AND TOTAL PRESSURES TO PSFA.
C
  PPL(J) = PPL(J) + PATM
  PT1(J) = (PT1(J) + PATM)*144.
  PT2(J) = (PT2(J) + PATM)*144.
C
C CONVERT PLENUM TEMPERATURE THERMOCOUPLE DATA TO ABSOLUTE TEMPERATURES.
C CALCULATE LOCAL VALUES OF GAMMA AND OTHER TERMS THAT DEPEND ON PLENUM
C TEMPERATURE AND CALCULATE SUMS FOR DETERMINATION OF MEAN VALUES OF
C GAMMA AND PLENUM TEMPERATURE AND PRESSURE.
C
  TPL(J) = 32.144 + (35.77*TPL(J)) - (.4518*(TPL(J)**2))
  GAMMA = 1.4018 - (2.E-5*TPL(J))
  FGAMMA = FGAMMA + GAMMA
  TPL(J) = TPL(J) + 459.69

```



```

FTPLM = FTPLM + TPL(J)
AP2 = GAMMA*RG*TPL(J)
AA = AP2/GAMMA
FPPLM = FPPLM + PPL(J)

C CALCULATE VELOCITIES AND DENSITIES AT MEASURING STATIONS.
C
V1SQ = ((2./(GAMMA-1.))*AP2)*(1.-((1.-(DP1(J)/PT1(J)))*((GAMMA-1.
1)/GAMMA)))
V1(J) = SQRT(V1SQ)
V2SQ = ((2./(GAMMA-1.))*AP2)*(1.-((1.-(DP2(J)/PT2(J)))*((GAMMA-1.
1)/GAMMA)))
V2(J) = SQRT(V2SQ)
RHO1(J) = (PT1(J)/AA)*((1.-(DP1(J)/PT1(J)))*((1./GAMMA)))
RHO2(J) = (PT2(J)/AA)*((1.-(DP2(J)/PT2(J)))*((1./GAMMA)))

C CONVERT FLOW ANGLES TO RADIAN.
C
ALFA1(J) = ALFA1(J)*1.745329E-2
ALFA2(J) = ALFA2(J)*1.745329E-2
THETA2(J) = THETA2(J)*1.745329E-2

C CALCULATE VELOCITY COMPONENTS AT MEASURING STATIONS.
C
VA1(J) = V1(J)*COS(ALFA1(J))
VA2(J) = V2(J)*COS(THETA2(J))*COS(ALFA2(J))
VT2(J) = V2(J)*COS(THETA2(J))*SIN(ALFA2(J))

C COMPUTE INTEGRAL VALUES AT INLET MEASURING PLANE (1) AS FUNCTION OF X.
C
F11(J) = RHO1(J)*VA1(J)
F12(J) = PT1(J)*F11(J)
F13(J) = V1(J)*F11(J)
F14(J) = (PT1(J) - DP1(J))*F11(J)
F15(J) = ALFA1(J)*F11(J)
F16(J) = DP1(J)*F11(J)

C COMPUTE INTEGRAL VALUES AT EXIT MEASURING PLANE (2) AS FUNCTION OF X.
C
F21(J) = RHO2(J)*VA2(J)
F22(J) = PT2(J)*F21(J)
F23(J) = V2(J)*F21(J)
F24(J) = (PT2(J) - DP2(J))*F21(J)
F25(J) = ALFA2(J)*F21(J)
F26(J) = VA2(J)*F21(J)
F27(J) = PT2(J) - DP2(J)
F28(J) = VT2(J)*F21(J)
50 CONTINUE

```



```

C INTEGRATE IN X (SPACING) DIRECTION USING SUBROUTINE SIMP.
C
CALL SIMP (F11,NPTS,F11T)
CALL SIMP (F12,NPTS,F12T)
CALL SIMP (F13,NPTS,F13T)
CALL SIMP (F14,NPTS,F14T)
CALL SIMP (F15,NPTS,F15T)
CALL SIMP (F16,NPTS,F16T)
CALL SIMP (F21,NPTS,F21T)
CALL SIMP (F22,NPTS,F22T)
CALL SIMP (F23,NPTS,F23T)
CALL SIMP (F24,NPTS,F24T)
CALL SIMP (F25,NPTS,F25T)
CALL SIMP (F26,NPTS,F26T)
CALL SIMP (F27,NPTS,F27T)
CALL SIMP (F28,NPTS,F28T)

C COMPUTE MEAN VALUES OF GAMMA, TPL, PPL, AND AP2.
C
PTS = FLOAT(NPTS)
GAM = FGAMMA/PTS
TPLM = FTPLM/PTS
PELM = FPPLM/PTS
AP2M = GAM*G*RG*TPLM
AAM = AP2M/GAM

C COMPUTE MASS-AVERAGED CCNDITIONS AT STATIONS 1 AND 2.
C
PT1M = F12T/F11T
P1M = F14T/F11T
V1M = F13T/F11T
ALFA1M = (F15T/F11T)*57.29578
T1 = TPLM*(1.-((GAM-1.)/2.))*((V1M**2)/AP2M))
DP1M = F16T/F11T
PT2M = F22T/F21T
P2M = F24T/F21T
V2M = F23T/F21T
ALFA2M = (F25T/F21T)*57.29578
T2 = TPLM*(1.-((GAM-1.)/2.))*((V2M**2)/AP2M))

C COMPUTE LOSS COEFFICIENTS AT PRESENT SPANWISE POSITION.
C
EXPO = (GAM-1.)/GAM
FY2(K) = (PT1M-PT2M)/DP1M
Y2 = FY2(K)
FZETA2(K) = 1. - ((1.-((P2M/PT2M)**EXPO))/(1.-((P2M/PT1M)**EXPO)))
ZETA2 = FZETA2(K)

```

```

00001450
00001460
00001470
00001480
00001490
00001500
00001510
00001520
00001530
00001540
00001550
00001560
00001570
00001580
00001590
00001600
00001610
00001620
00001630
00001640
00001650
00001660
00001670
00001680
00001690
00001700
00001710
00001720
00001730
00001740
00001750
00001760
00001770
00001780
00001790
00001800
00001810
00001820
00001830
00001840
00001850
00001860
00001870
00001880
00001890
00001900
00001910
00001920

```





```

C COMPUTE ADDITIONAL OUTPUT PARAMETERS: RELATIVE BLADE HEIGHT, MACH
C NUMBERS, MASS FLOW RATIO, AND CASCADE PRESSURE RATIO.
C
    RBH = Z/H
    ACH1 = V1M/SQRT(GAM*G*RG*TI1)
    ACH2 = V2M/SQRT(GAM*G*RG*TI2)
    RMF = F11T/F21T
    PR = PPLM/PATM

C WRITE OUTPUT DATA.
C
    WRITE (6,60) NRUN,RBH,PT1M,V1M,ACH1,ALFA1M,PT2M,P2M,V2M,ACH2,
    1ALFA2M,Y2,ZETA2,RMF,PR
    60 FORMAT (1H0,I4,F10.3,F11.1,F8.1,F9.2,F7.3,F8.2,2F8.1,F9.2,F7.3,F8.
    12,2F8.4,2F7.3)

C CALCULATE LOCAL VALUES OF LOSS COEFFICIENTS AT CASCADE EXIT (2).
C
    DO 70 L=1,NPTS
    FY2L(L) = (PT1M-PT2(L))/DP1M
    Y2LOC(L,K) = FY2L(L)
    70 CONTINUE

C ITERATE FOR DENSITY RHO3 FAR DOWNSTREAM AND CALCULATE LOSS
C COEFFICIENT BASED ON CONDITIONS FAR DOWNSTREAM (3).
C
    RHO3P = RHO2(1) - X2(1)/12.
    DX3 = (F26T/DX3) - ((F21T**2)/(RHO3P*(DX3**2)))+(F27T/DX3)
    80 P3 = (F26T/DX3) - ((F21T**2)/(RHO3P*(DX3**2)))+(F27T/DX3)
    V3SQ = ((F28T**2)/(F21T**2)) + ((F21T**2)/(RHO3P*(DX3**2)))
    PRA = (1. - ((GAM-1.)/2.)*((V3SQ/AP2M)))*((GAM/(GAM-1.)))
    RHO3C = (PRA**((1. - GAM)/GAM))*((P3/AAM)
    IF(ABS(RHO3C-RHO3P) - EPS) 100,100,90
    90 RHO3P = RHO3C
    GO TO 80
    100 P13 = P3/PRA
    FY3(K) = (PT1M-PT3)/DP1M
    FZETA3(K) = 1. - ((1. - (PRA**EXPC))/(1. - ((P3/PT1M)**EXPO)))
    BH(K) = RBH
    110 CONTINUE

C COMPUTE OVERALL LOSS COEFFICIENTS BY INTEGRATING VALUES OBTAINED AT
C EACH SPANWISE POSITION WITH FUNCTION ZINT.
C
    BHLO = BH(1)
    BHUP = 1. DO
    Y2I = ZINT(BH,FY2,NSETS,BHLO,BHUP)

```













## BIBLIOGRAPHY

1. Lakshminarayana, B. and Horlock, J. H., "Review: Secondary Flows and Losses in Cascades and Axial-Flow Turbomachines," International Journal of Mechanical Sciences, v. 5, pp. 287-307, 1963.
2. National Advisory Committee for Aeronautics Report 1163, A Visualization Study of Secondary Flows in Cascades, by H. Z. Herzig, A. G. Hansen, and G. R. Costello, 1954.
3. National Advisory Committee for Aeronautics Report 1168, Secondary Flows and Boundary-Layer Accumulations in Turbine Nozzles, by H. E. Rohlik and others, 1954.
4. Kofskey, M. G. and Allen, H. W., Smoke Study of Nozzle Secondary Flows in a Low-Speed Turbine, NACA Technical Note 3260, November 1954.
5. Herzig, H. Z. and Hansen, A. G., "Visualization Studies of Secondary Flows with Applications to Turbomachines," Transactions of the ASME, v. 77, pp. 249-266, April 1955.
6. Allen, H. W. and Kofskey, M. G., Visualization Study of Secondary Flows in Turbine Rotor Tip Regions, NACA Technical Note 3519, September 1955.
7. Hansen, A. G. and Herzig, H. A., Cross Flows in Laminar Incompressible Boundary Layers, NACA Technical Note 3651, February 1956.
8. Herzig, H. Z. and Hansen, A. G., "Experimental and Analytical Investigation of Secondary Flows in Ducts," Journal of the Aeronautical Sciences, v. 24, pp. 217-231, March 1957.
9. Fritzsche, A., "The Mechanism of Flow in Cascades," Sulzer Technical Review, v. 37, pp. 53-65, 1955.
10. Aeronautical Research Council Reports and Memoranda No. 3136, Secondary Flow and Losses in a Compressor Cascade, by J. F. Louis, March 1958.
11. Griepentrog, H., Prediction des Performances des Grilles d'Aubes Transsoniques a Haute Deflexion et Faible Allongement, Institut von Karman Note Technique 59, December 1969.





12. Vavra, M. H., Aero-Thermodynamics and Flow in Turbomachines, John Wiley and Sons, 1960.
13. Senoo, Y., "The Boundary Layer on the End Wall of a Turbine Nozzle Cascade," Transactions of the ASME, v. 80, pp. 1711-1720, November 1958.
14. Dean, R. C., Jr., Secondary Flow in Axial Compressors, Sc.D. Thesis, Massachusetts Institute of Technology, May 1954.
15. Gawain, T. H., "Some Recent Developments in the Numerical Analysis and Simulation of Fluid Turbulence," Proceedings of the Workshop on Flow in Turbomachines, Naval Postgraduate School Report No. NPS-57VA71111A, edited by M. H. Vavra, K. D. Papailiou, and J. R. Woods, Jr., 16 November 1971.
16. Hinze, J. O., Turbulence, pp. 18-24, McGraw-Hill, 1959.
17. Schlichting, H., Boundary-Layer Theory, p. 531, McGraw-Hill, 1968.
18. Fagan, J. R., Three-Dimensional, Subsonic, Duct Flow Analysis, Second Quarterly Technical Progress Report, Detroit Diesel Allison Division, January 1972.
19. Wu, Chung-Hua, A General Theory of Three-Dimensional Flow in Subsonic and Supersonic Turbomachines of Axial-, Radial-, and Mixed-Flow Types, NACA Technical Note 2604, January 1952.
20. Squire, H. B. and Winter, K. G., "The Secondary Flow in a Cascade of Airfoils in a Nonuniform Stream," Journal of the Aeronautical Sciences, v. 18, pp. 271-277, April 1951.
21. Hawthorne, W. R., "Secondary Circulation in Fluid Flow," Proceedings of the Royal Society, v. A206, pp. 374-387, 1951.
22. Papailiou, K. D., "A Review of the History of Boundary Layer Calculation Methods and the Present State of the Art," Proceedings of the Workshop on Flow in Turbomachines, Naval Postgraduate School Report No. NPS-57VA71111A, edited by M. H. Vavra, K. D. Papailiou, and J. R. Woods, Jr., 16 November 1971.
23. National Advisory Committee for Aeronautics Report 1067, Generalization of the Boundary-Layer Momentum-Integral Equations to Three-Dimensional Flows Including Those of Rotating System, by A. Mager, 1952.





24. Senoo, Y., "Three-Dimensional Laminar Boundary Layer in Curved Channel with Acceleration," Transactions of the ASME, v. 80, pp. 1721-1733, November 1958.
25. Dring, R. P., "A Momentum-Integral Analysis of the Three-Dimensional Turbine End-Wall Boundary Layer," Transactions of the ASME, v. 93, pp. 386-396, October 1971.
26. Woods, J. R., Jr., The Analytical Treatment of Secondary Flows and Associated Losses in Axial-Flow Turbo-machines, Naval Postgraduate School Report No. NPS-57WO71121A, 10 December 1971.
27. Rose, C. C., Jr. and Guttormson, D. L., Installation and Test of a Rectilinear Cascade, M.S. Thesis, Naval Postgraduate School, 1964.
28. Bartocci, J. E., An Investigation of the Flow Conditions at the Lower Measuring Plane, and in the Plenum Chamber of the Rectilinear Cascade Test Facility, Naval Postgraduate School, Department of Aeronautics Technical Note No. 66T-3, April 1966.
29. Bartocci, J. E., Cascade Tests of the Blading of a High-Deflection, Single-Stage, Axial-Flow Impulse Turbine and Comparison of Results with Actual Performance Data, A.E. Thesis, Naval Postgraduate School, May 1966.
30. Bown, R. L., An Investigation of the Secondary Flow Phenomena in a Cascade of High-Deflection Axial-Flow Impulse Turbine Blades, M.S. Thesis, Naval Postgraduate School, December 1966.
31. Zeleny, P. C., Online Data-Acquisition Under OS/360, Naval Postgraduate School Technical Note No. 0211-17, September 1971.
32. Kline, S. J. and McClintock, F. A., "Describing Uncertainties in Single-Sample Experiments," Mechanical Engineering, v. 75, pp. 3-8, January 1953.
33. Aeronautical Research Council Reports and Memoranda No. 2891, An Examination of the Flow and Pressure Losses in Blade Rows of Axial-Flow Turbines, by D. G. Ainley and G. C. R. Mathieson, March 1951.
34. Vavra, M. H., "Problems of Fluid Mechanics in Axial Turbomachines," Von Karman Institute Course Note 556, March 1969.



35. Aeronautical Research Council Reports and Memoranda No. 2891, A Method of Performance Estimation for Axial-Flow Turbines, by D. G. Ainley and G. C. R. Mathieson, December 1951.
36. Dunham, J. and Came, P. M., Improvements to the Ainley-Mathieson Method of Turbine Performance Prediction, paper no. 70-GT-2 presented at the ASME Gas Turbine Conference, Brussels, Belgium, May 1970.
37. Dunham, J., "Review of Cascade Data on Secondary Losses in Turbines," Journal of Mechanical Engineering Science, v. 12, pp. 48-59, 1970.
38. Markov, N. M., Calculation of the Aerodynamic Characteristics of Turbine Blading, Associated Technical Services, 1958.
39. Horlock, J. H., Axial Flow Turbines, Butterworths, 1966.
40. Davis, P. J. and Rabinowitz, P., Numerical Integration, pp. 22-24, 193, Blaisdell, 1967.



# INITIAL DISTRIBUTION LIST

	No. Copies
1. Defense Documentation Center Cameron Station Alexandria, Virginia 22314	2
2. Library, Code 0212 Naval Postgraduate School Monterey, California 93940	2
3. Commanding Officer Naval Air Systems Command Navy Department Washington, D.C. 20360	1
4. Rear Admiral C. O. Holmquist, USN Chief of Naval Research Office of Naval Research Arlington, Virginia 22218	1
5. Professor M. H. Vavra, Code 57Va Department of Aeronautics Naval Postgraduate School Monterey, California 93940	1
6. LCDR J. R. Woods, Jr., USN HELANTISUBRON(L) 31 Naval Air Station Imperial Beach, California 92032	1
7. Chairman Department of Aeronautics Naval Postgraduate School Monterey, California 93940	1



## DOCUMENT CONTROL DATA - R &amp; D

(Security classification of title, body of abstract and indexing annotation must be entered when the overall report is classified)

1. ORIGINATING ACTIVITY (Corporate author) Naval Postgraduate School Monterey, California 93940		2a. REPORT SECURITY CLASSIFICATION Unclassified	
		2b. GROUP	
3. REPORT TITLE AN INVESTIGATION OF SECONDARY-FLOW PHENOMENA AND ASSOCIATED LOSSES IN A HIGH-DEFLECTION TURBINE CASCADE			
4. DESCRIPTIVE NOTES (Type of report and inclusive dates) Doctor's Thesis; September 1972			
5. AUTHOR(S) (First name, middle initial, last name) James R. Woods, Jr.; Lieutenant Commander, United States Navy			
6. REPORT DATE September 1972		7a. TOTAL NO. OF PAGES 123	7b. NO. OF REFS 40
8a. CONTRACT OR GRANT NO.		9a. ORIGINATOR'S REPORT NUMBER(S)	
b. PROJECT NO.			
c.		9b. OTHER REPORT NO(S) (Any other numbers that may be assigned this report)	
d.			
10. DISTRIBUTION STATEMENT Approved for public release; distribution unlimited.			
11. SUPPLEMENTARY NOTES		12. SPONSORING MILITARY ACTIVITY Naval Postgraduate School Monterey, California 93940	
13. ABSTRACT  In this study precise quantitative data were established for the overall flow losses in a high-deflection turbine rotor cascade for a range of aspect ratios h/c from 1.480 to 0.592. The magnitude of the losses due to secondary-flow effects was also determined. From these measurements it was possible to obtain an improved physical description of the complex secondary-flow phenomena.			







14	KEY WORDS	LINK A		LINK B		LINK C	
		ROLE	WT	ROLE	WT	ROLE	WT
	TURBOMACHINE  SECONDARY-FLOW PHENOMENA  SECONDARY-FLOW LOSSES  HIGH-DEFLECTION TURBINE BLADING						



8 NOV 78

135638

Thesis  
W842  
c.1

Woods

135638

An investigation of  
secondary-flow phenome-  
na and associated loss-  
es in a high-deflection  
turbine cascade.

8 NOV 78

135638

Thesis  
W842  
c.1

Woods

135638

An investigation of  
secondary-flow phenome-  
na and associated loss-  
es in a high-deflection  
turbine cascade.

thesW842

An investigation of secondary-flow pheno



3 2768 001 90615 9

DUDLEY KNOX LIBRARY